# INFORMATION TO USERS

This manuscript has been reproduced from the microfilm master. UMI films the text directly from the original or copy submitted. Thus, some thesis and dissertation copies are in typewriter face, while others may be from any type of computer printer.

**The quality of this reproduction is dependent upon the quality of the copy submitted.** Broken or indistinct print, colored or poor quality illustrations and photographs, print bleedthrough, substandard margins, and improper alignment can adversely affect reproduction.

In the unlikely event that the author did not send UMI a complete manuscript and there are missing pages, these will be noted. Also, if unauthorized copyright material had to be removed, a note will indicate the deletion.

Oversize materials (e.g., maps, drawings, charts) are reproduced by sectioning the original, beginning at the upper left-hand corner and continuing from left to right in equal sections with small overlaps.

Photographs included in the original manuscript have been reproduced xerographically in this copy. Higher quality 6" x 9" black and white photographic prints are available for any photographs or illustrations appearing in this copy for an additional charge. Contact UMI directly to order.

ProQuest Information and Learning
300 North Zeeb Road, Ann Arbor, MI 48106-1346 USA
800-521-0600

# The Star Thrust Experiment, Rotating Magnetic Field Current Drive in the Field Reversed Configuration

Kenneth Elric Miller

A dissertation submitted in partial fulfillment
of the requirements for the degree of

Doctor of Philosophy

University of Washington

2001

Program Authorized to Offer Degree: Aeronautics and Astronautics

In presenting this dissertation in partial fulfillment of the requirements for the Doctoral degree at the University of Washington, I agree that the Library shall make its copies freely available for inspection. I further agree that extensive copying of the dissertation is allowable only for scholarly purposes, consistent with "fair use" as prescribed in the U.S. Copyright Law. Requests for copying or reproduction of this dissertation may be referred to Bell and Howell Information and Learning, 300 North Zeeb Road, Ann Arbor, MI 48106-1346, to whom the author has granted "the right to reproduce and sell (a) copies of the manuscript in microform and/or (b) printed copies of the manuscript made from microform."

Signature Kenneth Miller

Date 3/11/01

University of Washington
Graduate School

This is to certify that I have examined this copy of a doctoral dissertation by

Kenneth Elric Miller

and have found that it is complete and satisfactory in all respects,
and that any and all revisions required by the final
examining committee have been made.

Chair of Supervisory Committee:

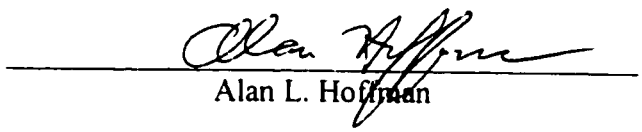

Alan L. Hoffman

Reading Committee:

Alan L. Hoffman

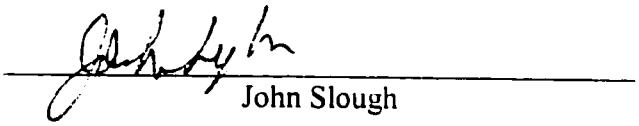

John Slough

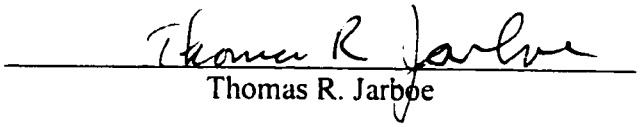

Thomas R. Jarboe

Date: 3/11/01

University of Washington

Abstract

The Star Thrust Experiment, Rotating Magnetic Field
Current Drive in the Field Reversed Configuration

Kenneth Elric Miller

Chair of Supervisory Committee:
Professor Alan Hoffman
Aeronautics and Astronautics

The Star Thrust Experiment (STX) has formed and sustained the Field Reversed Configuration (FRC) with a Rotating Magnetic Field (RMF) operated at a strength of 25 G and a frequency of 350 kHz. The RMF was generated with two IGBT switched solid state power supplies capable of delivering 2 MW each. Plasmas were typically 2 m long by 0.2 m in radius and consisted of fully ionized deuterium at temperatures of 60 eV and peak densities of $5\times10^{18}$ $m^{-3}$. The primary diagnostic was an extremely small 24 channel berylia jacketed internal magnetic probe that was used to make measurements as a function of time, radius, and axial position. These measurements when combined with the FRC's unique geometry and equilibrium relationships determined many other important plasma parameters. Axial confining fields of 100 G maintained a true vacuum boundary around the plasma and allowed for the study of FRC RMF equilibrium interactions. Key findings are that the RMF maintained a near zero separatrix pressure, penetrated only partially, and drove strong radial and axial flows. Issues discussed include the importance of the RMF driving an axial current distribution consistent with that of the FRC, possible benefits of varying the average beta condition, and potential RMF antenna length limits set by the tendency of driven axial flows to screen the RMF from the plasma.

# TABLE OF CONTENTS

# LIST OF FIGURES

# LIST OF TABLES

# Acknowledgements

The author wishes to express his sincere appreciation to:

John Slough, for providing essential guidance, insight and help throughout this experiment.

Alan Hoffman, for providing continuous support as well as enormous latitude and freedom in the undertaking of this research.

Mark Kostora, Bob Brooks, Dan Lotz, John Hayward, Scott Kimball, Dennis Peterson, and Dzung Tran, for their assistance in building and operating this experiment.

Vibhavaree Gargeya, my wife, for her interest, enthusiasm, and continuous support throughout this entire process.

Quasar and Nemesis, the family cats, for the hours of distraction they provided while at home writing this thesis.

# Dedication

To the advancement of science and betterment of society

# CHAPTER 1
# INTRODUCTION

The FRC[24] is a magnetic confinement scheme belonging to the class of compact toroids. It consists of an elongated current ring held in an external solenoidal field with the plasma confined by the current ring's own closed poloidal magnetic field, figure 1.1. There is minimal, if any, toroidal field. Though having unresolved physics issues regarding confinement and stability[5,6], the FRC is of interest due to its nearly ideal reactor attributes. The FRC is a compact high beta configuration capable of being confined in simple linear devices. The equilibrium is set by a plasma pressure balancing the radial magnetic pressure and the axial field line tension. The low average internal field gives the FRC the potential to burn advanced aneutronic fuels[19]. Further, the FRC has a natural divertor with plasma flowing radially out across the closed field lines and onto the axial open field lines where it is readily transported away from the configuration.

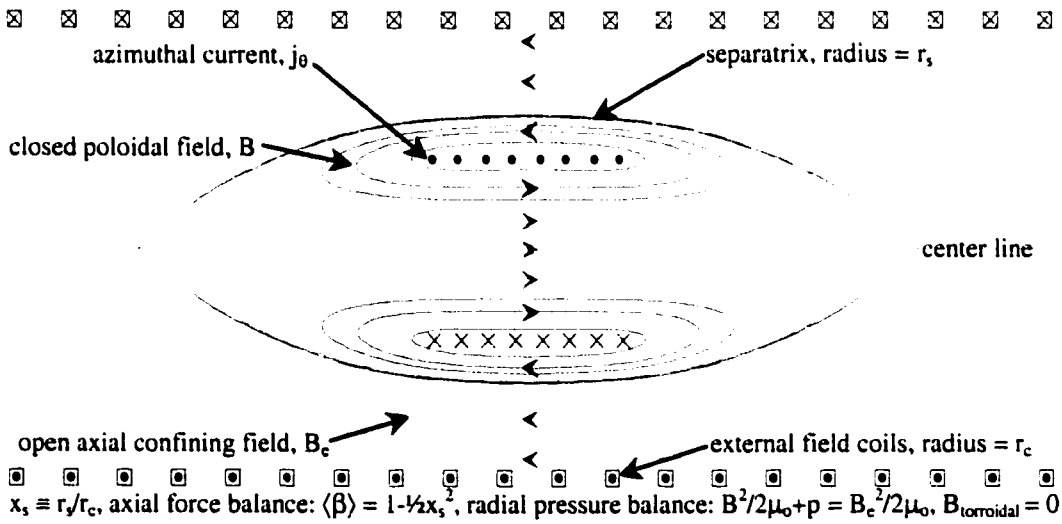


Figure 1.1 The Field Reversed Configuration, FRC.

At present, high energy density FRCs have only been made using the field reversed Theta Pinch (FRTP) technique. This method involves cumbersome high voltage pulsed

power technology, and due to the dynamics of formation it places severe constraints on the resultant FRC. More importantly, this technique is only useful for forming FRCs. It inherently lacks any sustainment capability, and the FRCs so generated decay away resistively. The next step along the FRC research path is to develop a simplified formation technique coupled with sustainment capability.

The star thrust experiment (STX) has been designed to create and then sustain FRCs using a rotating magnetic field (RMF). The RMF is a spatially uniform magnetic field transverse to the FRC's axis of symmetry, that rotates uniformly in time, figure 1.2. It can be generated by two perpendicular wire loops powered by two RF supplies run 90 degrees out of phase. When plasma conditions are properly selected the RMF can both create and then directly sustain the azimuthal current ring that comprises the FRC. Conditions are selected so that the electrons are magnetized to the RMF while the ions are not. Then, as the field rotates it pulls the electrons around, directly driving the azimuthal current and sustaining the FRC. This is in contrast to the field reversed theta pinch technique which uses a rapid axial field reversal to trap an initial reverse bias field and temporarily create the azimuthal current ring.

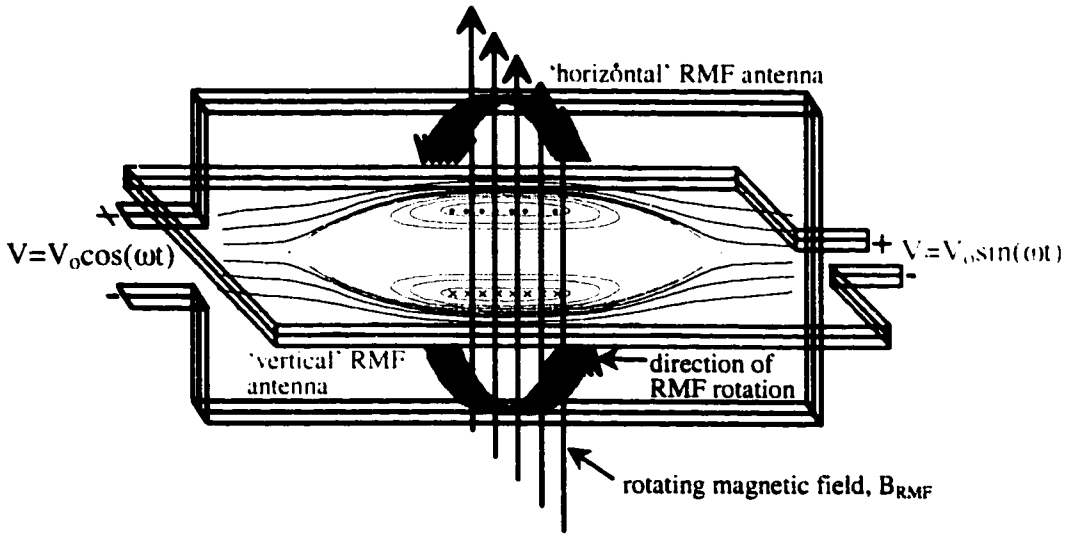


Figure 1.2 The Rotating Magnetic Field Applied to the FRC.

RMF current drive has been demonstrated by several groups[1], but has primarily been investigated by a research group located at Flinders University in Australia[13,15,3,2]. In a series of experiments with different, though typically spherical, confinement vessels, current was driven in a small wall supported partially ionized plasma. STX has been designed to take the next step along this research path in several key areas. It will apply the RMF to a fully ionized plasma with a true FRC equilibrium, one where the RMF amplitude is small compared to the FRC's equilibrium fields, and where the FRC is not wall supported. Specifically, STX has been designed to study the interaction between the RMF and FRC equilibrium, with a focus on the ability of the RMF to sustain the FRC configuration. This is as opposed to prior experiments where the focus was on the general ability of the RMF to drive current.

The initial starting point of STX was to apply the RMF to the source section of the TRAP[22] experiment. There, 50 eV FRCs with kilogauss axial confining fields were made at densities of $10^{21}$-$10^{22}$ $m^{-3}$ in a 3 m long by 0.2 m radius quartz vacuum chamber via the FRTP formation technique. The RMF formation and sustainment of such an FRC would certainly have demonstrated the physics of RMF FRC sustainment. It rapidly became apparent that this source section was not suitable due to screening effects from the axial field magnets. However, sufficient spare equipment existed to build a new vacuum chamber of the same size, with appropriate 'high transparency' axial field magnets. This set the scale of the STX experiment, an order of magnitude larger than prior RMF experiments.

The real challenge facing STX, as well as for all of the previous experiments, was the constructing of a suitable RMF power supply, one that could generate the desired RMF power for the duration of the experiment. The difficulty in constructing a suitable RMF power supplies arises from the very high power needed, a need which arises from the high $\beta$ equilibrium of the FRC, where an internal plasma pressure balances the external magnetic pressure. The plasma must be sufficiently hot to balance this external magnetic

pressure, but until the configuration exists, the field lines are open, and the plasma is difficult to heat. Furthermore, until the plasma is hot, a large $B_{RMF}$, and hence power, is needed to satisfy the RMF current drive conditions, to the point of violating the condition that $B_{RMF}$ is a small perturbation to $B_{axial}$. It is believed that the plasma must be ionized, made sufficiently hot, and the FRC formed on the time scale of particle flow to the wall, all of which requires enormous input power. To illustrate the challenge in the context of STX's design, consider a 1 mT gas of D2 with a 1 kG axial confining field. This would ionize to produce a plasma of $6.4 \times 10^{19}$ $m^{-3}$. Using typical ionization energies of 100 eV per D2 and resulting 5 eV temperatures, 260 J are needed to fully ionize the 0.5 $m^3$ static fill. At 5 eV, the particles have an average speed of 3 cm/μsec, and will strike the wall in a characteristic time of 30 μsec. To form the FRC in this time would require an average 8 MW power input, assuming a perfect coupling to the plasma.

Under such conditions, even more power is required to keep the RMF penetrated. From the RMF skin depth penetration requirement, see chapter 2, using $\delta_{effective}$ = 20 cm and assuming classical resistivity, a 240 G RMF is required to stay penetrated. Amperes law applied axially to the FRC, $BL=\mu_o I_{enclosed}$, coupled with the rigid rotor FRC current profile, $I=0.5ne\omega_{RMF}R^2$, set the RMF frequency to be 390 kHz. This corresponds to a circulating field power of 90 MW over the 0.5 $m^3$ plasma volume. Due to energy being tied up in the near field of the RMF antenna and to the field extending outside the plasma volume, about 5 times this circulating power is needed to produce an RMF uniform to 10% over the plasma volume. With an antenna circuit Q of 25, 18 MW could sustain this circulating power. However, once again assuming classical resistivity, if the plasma were brought to 50 eV, only a 42 G RMF is need to satisfy the penetration requirement, a small perturbation to the FRC. In addition, this could be sustained with a 300 kW RMF supply, something which is much more reasonable.

Though based on a simple analysis, the above discussion made it clear that for STX to work, very high power RMF supplies would be needed, at least initially. Two approaches

were initially pursued to construct suitable supplies. The first involved the ring down of an initially charged LC tank circuit. This would certainly have produced a sufficient RMF power of several hundred megawatts, but the duration of the drive would have been fairly short, limited by the Q of the tank circuit with plasma loading. The second approach, which was eventually selected, involved the use of high power solid state switches to drive the RMF via a resonant tank circuit. It was known that the solid state supplies would never match the initial power output of the ring down of an initially charged LC tank circuit, but they were selected because it was believed that they could drive the RMF for a much longer duration at sufficient power levels. This was a very fortunate decision since most of the new physics that has been learned from STX about the interaction of the FRC with the RMF would not have been learned if the experiment had only lasted for the duration of the ring down of an initially charged tank circuit.

With each switch used in the RMF power supplies capable of delivering a megawatt, the output of 12 switches run in parallel and magnified by a resonant circuit should have delivered the necessary power. Two supplies were built that produced an RMF at power levels vastly higher then anyone had previously realized with solid state switching. Unfortunately, for a variety of reasons discussed subsequently, they did not achieve the desired power levels discussed above, and as a result STX was forced to operate at much lower densities and fields then initially desired. However, enough was learned about the operation of the solid state switches during the STX experiment that construction of much higher power RMF supplies could now be realized, supplies that would allow operation at the initially hoped for densities of $10^{20}$ $m^{-3}$ and kilogauss axial fields. This experiment is presently funded by the Department of Energy as part of the TCS[7] program, though NASA provided the initial construction money because of the FRC's potential attributes for eventual fusion propulsion.

# CHAPTER 2
# THEORY

The RMF drives a strong azimuthal current which reverses the direction of the external axial magnetic field and produces the FRC configuration. Unlike field reversed theta pinch formation where this current is driven by an induced azimuthal voltage caused by a rapid reversal of the external field, the RMF current is driven in an inherently steady state manner which should allow for the subsequent sustainment of the configuration. Though the following explanation is a vast simplification, it explains not only the basic underlying physics, but also aids experimental design by giving first order estimates of various quantities such as the needed RMF frequency and amplitude. A good starting point for understanding the current drive process is the generalized Ohm's law, equation 2.1, coupled with an assumed fully penetrated RMF, represented by equation 2.2.

$$\mathbf{E} + \mathbf{v}\times\mathbf{B} = \eta\mathbf{j} + \mathbf{j}\times\mathbf{B}/ne - \nabla p_e/ne \qquad \text{equation 2.1}$$

$$B_r = B_\omega\cos(\omega t-\theta) \qquad B_\theta = B_\omega\sin(\omega t-\theta) \qquad \text{equation 2.2}$$

Of importance is the relative magnitude of the Hall term, $\mathbf{j}\times\mathbf{B}/ne \sim j_\theta B_\omega/ne$, to the resistive term, $\eta\mathbf{j} \sim m_e\nu_{ei}j_\theta/ne^2$. Their ratio, $\omega_{ce}/\nu_{ei}$, is a key parameter representing how well the electrons are tied to the RMF. $\omega_{ce} \sim eB_\omega/m_e$ is the electron cyclotron frequency or gyration rate about the RMF, while $\nu_{ei}$ is the electron ion collision frequency. It is the time averaged azimuthal component of Ohm's Law that is important to the current drive process, equation 2.3.

$$E_\theta = \eta_\perp j_\theta + v_r B_z + \langle j_z B_r\rangle/ne \qquad \text{equation 2.3}$$

Thus the azimuthal electric field is the result of three terms, $\eta_\perp j_\theta$, the familiar resistive drag, $v_r B_z$, a term due to radial flow, and $\langle j_z B_r\rangle/ne$, the RMF drive term. $E_\theta$ is of key importance since its value determines the rate of poloidal flux growth or decay via Faraday's Law, $V = -d\Phi/dt = \int\mathbf{E}\bullet d\mathbf{l}$. A true steady state equilibrium can only be attained by setting a time averaged $E_\theta$ to zero everywhere within the FRC, a requirement

equivalent to there being no steady state loop voltage within the FRC. Figure 2.1 shows the typical FRC coordinate system along with the conventional direction and sign of various quantities.

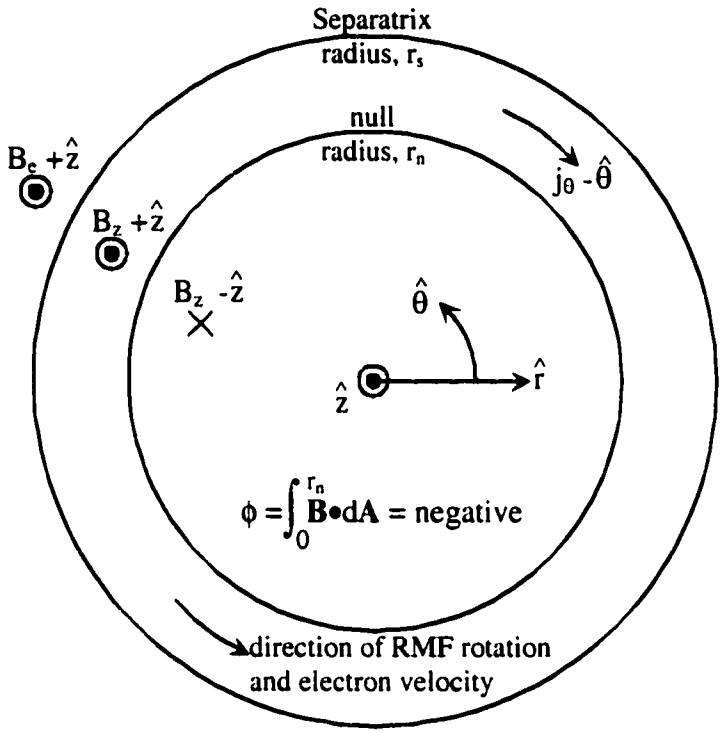


Figure 2.1 FRC coordinate system, conventional definitions

Consider the FRC equilibrium in conjunction with Faraday's law. In equilibrium the FRC's poloidal flux remains constant, $d\Phi/dt$ is zero and there is no azimuthal electric field. When the FRC is either growing or decaying, $d\Phi/dt$ is nonzero and there is an azimuthal electric field, a field set by the azimuthal component of Ohm's law. In the absence of the RMF, and for a moment ignoring the $v_r B_z$ term, equation 2.3 becomes $\langle E_\theta \rangle = \eta_\perp j_\theta$. $E_\theta$ is negative, $d\Phi/dt$ is positive, and the FRC is decaying since the poloidal flux $\phi$ is becoming less negative. The $v_r B_z$ term arises from the radial diffusion of particles. It can counteract the resistive term and even reverse the sign of $E_\theta$, except at the magnetic

null where $B_z$ is 0. It is at this point that flux is lost and the FRC's flux decay or growth rate is determined. The inclusion of the RMF adds the $\langle j_z B_r \rangle / ne$ term to equation 2.3. With the RMF rotating in the proper direction, the same direction as the electron diamagnetic current, the effect of the $\eta_\perp j_\theta$ term can be canceled and $E_\theta$ can be set to zero, or even made positive to attain FRC growth. Since the electrons behave resistively in the axial electric field generated by the RMF, $j_z$ and $B_r$ are always in phase and the $\langle j_z B_r \rangle / ne$ term in Ohm's law enters with a positive sign and counters the $\eta_\perp j_\theta$ term. The phase between $j_z$ and $B_r$ can be seen by applying the differential form of Faraday's law to the RMF field, and then integrating the azimuthal component along the r axis. The effect of the RMF is to create an azimuthal electric field that drives the electron current necessary to sustain the FRC and overcome resistive losses. It is important that the ions do not respond to this azimuthal electric field, for if they did, they would cancel the driven electron current. This simple particle picture has the electrons tied to the RMF and rotating cosynchronously with it while the ions remain at rest.

The above analysis provides for the first requirement on the RMF, that the electrons be magnetized while the ions are not, equation 2.4.

$$\nu_{ei} << \omega_{ce} \qquad \omega_{ci} \leq \omega_{RMF} < \omega_{ce} \qquad \text{equation 2.4}$$

When the Hall term dominates, an effective skin depth can be defined based on the solution to equation 2.3 for the axial current $j_z$ and the associated effective resistivity. This effective skin depth is expressed in equation 2.5.

$$\delta_{effective} = (\omega_{ce}/\nu_{ei})\delta_{classical} = (\omega_{ce}/\nu_{ei})\,(2\eta/\omega_{RMF}\mu_o)^{1/2} \qquad \text{equation 2.5}$$

In order to be consistent with the assumed full penetration, the effective skin depth for RMF penetration must be on the order of the plasma radius $r_p$. This second requirement on the RMF is expressed in equation 2.6.

$$\delta_{effective} > r_p \qquad \text{equation 2.6}$$

The seemingly contradictory statement that as the plasma becomes more conductive, the RMF penetrates farther, can be explained by viewing events from the electron frame of

reference. The difference between the RMF rotation frequency and the average electron rotation frequency, $\omega^*$, is the effective RMF frequency seen by the electrons. As the plasma collisionality decreases so does $\omega^*$, and thus the field penetrates farther. In the plasmas of interest it is the requirement that $\delta_{effective} > r_p$ that is most restrictive.

So far in this simple analysis, the RMF has been treated as an externally imposeable field with full penetration assumed. The issue of RMF penetration into an existing plasma is far more complicated and has been studied both theoretically and numerically on plasma cylinders of uniform density[10,17,14,12,20,7]. The equations governing the system are characterized by two important dimensionless parameters, $\gamma = \omega_{ce}/\nu_{ei}$ and $\lambda = r_p/\delta_{classical}$[11]. Though the penetration process is highly non-linear, penetration tends to occur for $\gamma > \lambda$. Since the plasmas of interest have $\delta_{classical} << r_p$, this is a statement of the above two constraints placed on the RMF, $\nu_{ei} << \omega_{ce}$ and $\delta_{effective} > r_p$, a nice confirmation of this simple analysis. In terms of basic physics, the RMF must create a steady force on the electrons sufficient to balance the drag force they feel due to plasma resistivity.

The preceding is a brief summary of how RMF theory stood prior to the construction of STX, and as such, it was used as the basis for designing STX, something discussed in more detail in the beginning of chapter 3. However, fairly early on in machine operation, it became apparent that the RMF was not fully penetrating the plasma. Using this observation, as well as the observation that there was no measurable plasma density at the separatrix radius, a simple analytic model[8] was developed that combined key elements of RMF current drive with the FRC's two dimensional equilibrium constraint, the average beta condition. The conclusions of this model, which were subsequently demonstrated by a detailed numeric simulation[18], were that if the separatrix density is held below that demanded by the rigid rotor FRC equilibrium, then full RMF penetration and the associated cosynchronous electron rotation are inconsistent with the FRC's natural equilibrium. Rather, the only consistent solution is for the RMF to penetrate just a little past the null radius. The RMF must reach the null radius since there, with $B_z = 0$, it is the

only term remaining in Ohm's law capable of countering the $\eta j$ term and sustaining or increasing the flux. Both the simple analytic model and the detailed numeric simulation were developed at the Redmond Plasma Physics Laboratory as part of the TCS program. Their overall purpose is to broaden the general understanding of the FRC RMF interaction, with a bias towards understanding and hopefully assisting the ongoing experimental effort, of which STX is a part. Having said this, these models will only be discussed in terms of their relevance to the STX experiment and to the general understanding of the RMF FRC interaction presented herein.

Partial RMF penetration raised the issue as to what the mechanism of current drive would be in regions where the RMF did not penetrate, i.e. in most of the interior of the FRC. Though obvious with hindsight, it took the detailed numeric solution to point out the importance of radial flow in driving this current. Prior to this, the flow term had typically been ignored as a non steady state term that really was not important anyway, since at the FRC null where all the flux is lost, flow has no effect on $E_\theta$. Radial flow immediately pointed out the importance of axial flow in what has been termed 'the end run'. In order for the RMF to drive a steady radial inward flow towards the axis of symmetry, the particles must be able to travel axially along the inner field lines, out to the ends of the FRC, and then back in towards the midplane on the outer field lines for the RMF to drive them in once more.

Where the RMF penetrates, it must provide enough torque to overcome the basic resistivity throughout the entire plasma. The resultant force is strong enough to counter outward radial diffusion and result in a steady inward flow. Inside the FRC where the RMF has not penetrated, it is believed that only a density gradient towards the axis of symmetry can sustain the flow necessary for steady state current drive, where the flow arises through natural diffusion down a density gradient. Results from STX will be presented in light of these two important realizations, that current must be driven in a manner consistent with the FRC's own equilibrium, and that radial and axial flow are

important. These realizations explain some of the key experimental observations, while the experiment demonstrates the validity of their importance.

# CHAPTER 3
# STX APPARATUS

The STX device is built around a 3 meter long by 40 centimeter diameter quartz tube. On one end, the vacuum end, is a 16" long by 17" diameter stainless steel chamber that provides vacuum access for all the pumps, gauges and diagnostics. The other end, the high voltage end, is electrically insulated from ground to about 50 kV, and is sealed with a 24" diameter quartz window. Surrounding the quartz tube is the RMF antenna as well as the solenoidal magnets that generate the various axial field configurations. Figure 3.1a shows a scale schematic of the apparatus with key components labeled, and figure 3.1b shows a picture of the apparatus with only the vertical RMF antenna constructed.

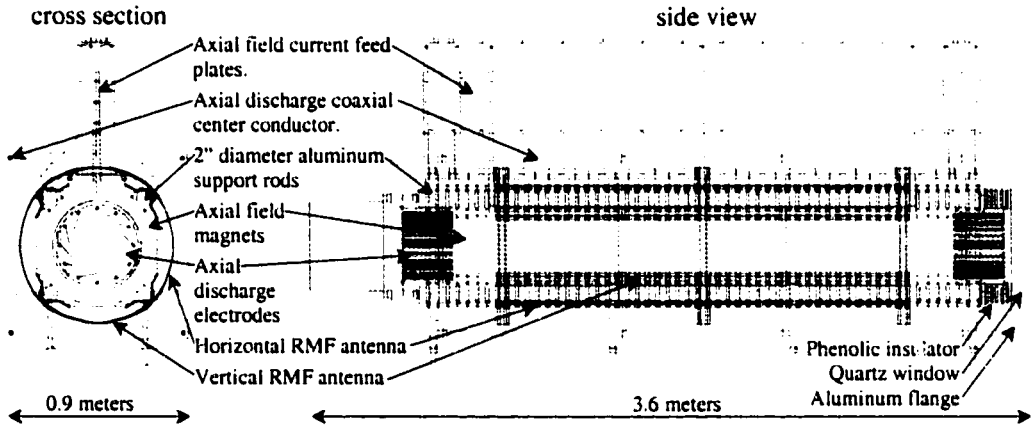


Figure 3.1a Scale schematic of STX

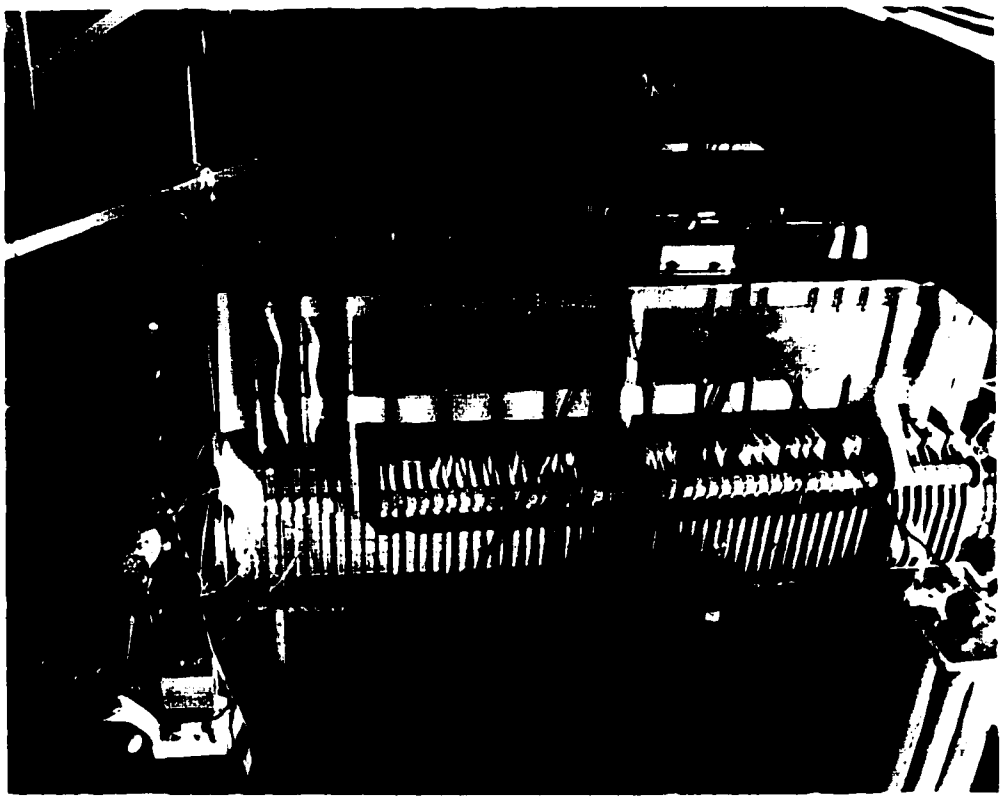

Figure 3.1b Picture of STX during construction

## The RMF Circuit

The most important components of the STX experiment are the two RMF circuits, one for each phase of the RMF, figure 3.2. Each circuit consists of three main elements, the IGBT power supply[23], a transformer, and an LC resonant circuit of which the inductor is the RMF antenna. The IGBT power supply takes a DC voltage and switches it to generate a square wave output with the correct period. The transformer matches the impedance of the IGBT power supply to that of the LC tank circuit for the frequency of interest, the sinusoidal fundamental of the square wave input. The tank circuit responds to this fundamental frequency and generates the RMF, amplifying the sinusoidal input power by a factor of Q.

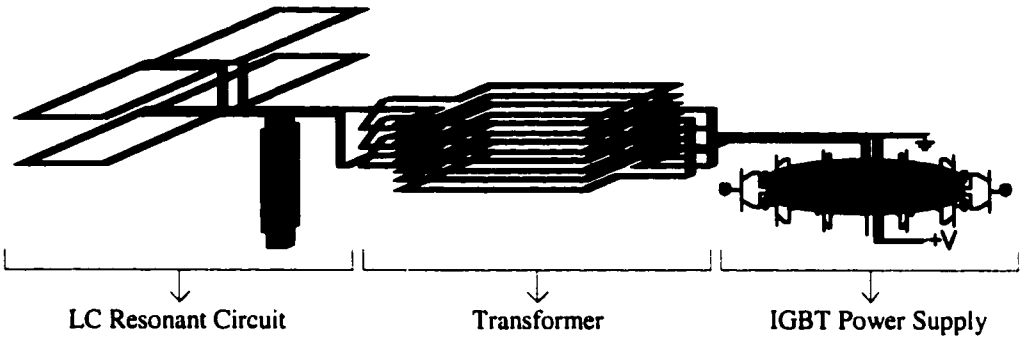


Figure 3.2 One phase of the RMF circuit

## RMF Antenna, LC Resonant Circuit

The simplest way of generating a rotating magnetic field is to take two mutually perpendicular coils and drive them 90 degrees out of phase with sinusoidal power supplies, figure 1.2. Near the center of the coils the field will be a close approximation to the ideal RMF given by equation 2.2. An RMF uniform over a much greater fraction of the coil's area can be obtained by separating each antenna coil into two parallel coils, where the coil separation is set by a Helmholtz minimization to be R when the wires are at radius R from the axis of the machine. It is important to minimize the region of non uniform field since any unused portion translates directly into wasted power. Figure 3.3 shows a cross section of the RMF antenna coil's location with respect to the quartz vacuum chamber, as well as the magnetic field they generate when there is equal current flowing in each of the coils. The coils are assumed to have a length much larger than their width which is a good approximation for the STX RMF antenna whose fields deviate from this approximation by about 5 percent. Contours mark 5 percent variations in the magnitude of $B_{RMF}$ from the field on axis. Each set of parallel coils is designated by its own color, and dots represent current flowing out of the page. It is not yet known if such a uniform RMF is needed, though the radius at which the antennas have been placed was selected in order to achieve this uniformity.

One unintended benefit of this selection has to do with the relative detuning of the circuit that occurs when plasma is present. Had the antennas been placed at a much smaller radius, the change in the circuit's resonant frequency due to the introduction of plasma, or even simple changes in the plasma itself, would have been sufficiently large that some active control of the drive frequency would have been needed in order to avoid shorting out the IGBT power supplies. Even though the IGBTs are not adversely affected, the amplitude of the RMF is. This is due to the high Q nature of the circuit and to series stray inductances in the transformers and IGBT power supplies which cause the voltage applied to the tank to drop as power demands increase. At present, the frequency is selected based on the desired time of circuit resonance, i.e. the time of maximum RMF amplitude, typically when plasma is present. However, the IGBT power supplies would lend themselves very well to being controlled by active feedback, control that would allow the supplies to track the circuits' resonant frequency and maintain a constant RMF amplitude.

Close inspection of the antenna coil set shown in figure 3.2 will reveal that it has actually been split into two parallel coils sets, one to the left and one to the right. This was done to minimize the antenna's inductance. It does not affect the uniformity of the RMF generated since in the central region of coil overlap, currents flow in opposite directions and the local fields cancel leaving a resultant field identical to that generated by a single coil set. Physically each coil consists of a single turn of copper strip 2.5 inches wide by 0.01 inches thick. Each coil is 2 m long by 58 cm wide and is separated from its parallel coil by 33.5 cm. This places the conductors at a radius of 33.5 cm. Each phase of the RMF antenna has an inductance of 0.67 μH. Such wide copper strip was used to reduce the inductance of the antenna. Another 20% reduction of the antennas inductance could be achieved by instead using 2" diameter copper pipe, though constructing such an antenna would be substantially harder. The importance of minimizing the antenna inductance and hence the impedance of the LC tank circuit arose from trying to match the tanks impedance to that of the IGBT power supply. The closer

the two impedances are made, the smaller the turns ratio in the transformer needs to be.

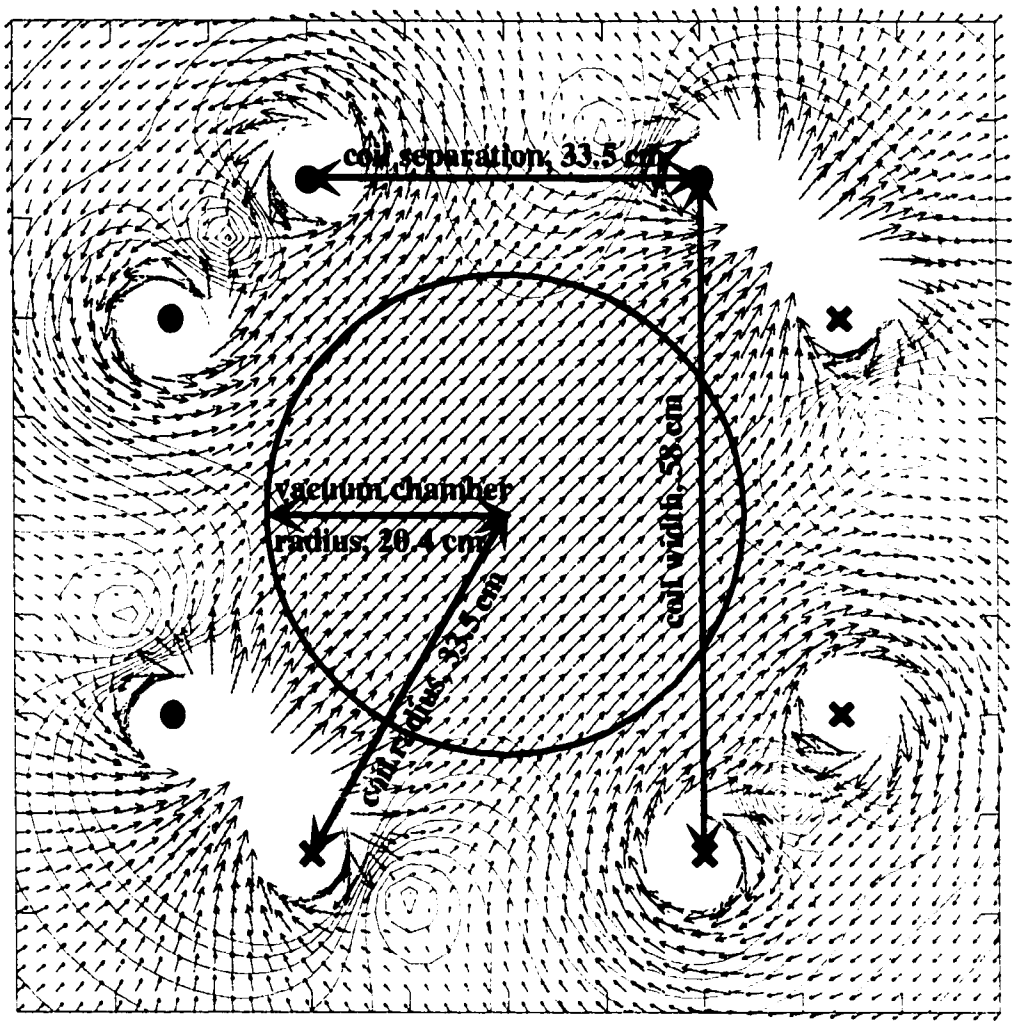


Figure 3.3 Cross section of the RMF with equal current in each conductor.

With the inductance of the antenna set by geometry, and the desired frequency of operation set by the above power considerations, the value of the capacitance was set to be 0.36 μF. To achieve this value, five capacitors each having a value of 80 nF were constructed from aluminum foil and 0.03 inch thick polyethylene sheet placed in mineral oil. Mineral oil, having an inherently high Q, was selected to prevent coronal losses that occur in air at higher voltages. Coronal losses were measured to change the Q of a

separate tank circuit from 40 to 20 as the voltage rose above 5 kV. In this separate tank circuit, the capacitor consisted of a stack of 0.01 inch thick copper plates separated by layers of 0.06 inch thick polypropylene. When placed in oil, the Q of this tank grew to 60. The tank's resonant frequency was 0.5 MHz, with an inductance of 1.6 μH. A spark gap was used to connect the initially charged capacitor across the inductor in order to begin circuit oscillation.

These five 80 nF capacitors were then connected in parallel with the RMF antenna. A parallel resonant circuit was selected over a series resonant circuit so that as the plasma loaded the circuit, the circuit's impedance would fall instead of rise. Thus a power supply driving the circuit at a constant voltage, something most supplies try to do, would simply need to deliver more current in order for the RMF amplitude to remain constant, ignoring the above stated issue of stray series inductance which tends to throttle this current. This parallel connection makes it rather easy to maintain a fairly constant RMF, though it is somewhat hazardous in that both circuit loading and detuning tends to short out the driving power supply, though no more than the tank circuit does when it is first starting to charge. One advantage of the stray series inductance is that it does limit the degree to which the power supplies can be shorted out, though in so doing, it also sets a limit on the maximum power transfer rate to several megawatts.

As it is charged and the circulating current builds, the impedance of a parallel resonant circuit changes from $(L/C)^{1/2}$ to $Q(L/C)^{1/2}$ with a circulating power of Q times the input power. Q is the quality factor of the circuit and is proportional to the total energy stored in the tank circuit divided by the energy lost per cycle. The circuit Q is essentially a free multiplier one gets on the power available to drive the RMF, though not to heat the plasma. In order to maximize this gain it is important that the plasma be the dominant load seen by the tank circuit as opposed to the real resistance in the circuit itself. In vacuum, the constructed tank has a Q of about 60, though this value may be slowly falling. The majority of the resistance, 21 of the total 23 mΩ, resides in the capacitors,

most likely in the connections between the aluminum foil sheets and the copper feeds. The electrical connection was made through compression, and an oil film has likely leaked in between the connection. Unfortunately this seems to be the dominant load seen by the circuit even with plasma present. It would be relatively easy to replace these capacitors though, and a substantial increase in circulating power could be realized. Increasing the Q of the tank circuit allows for higher voltage, and hence circulating power, operation by allowing the use of a transformer with a greater turns ratio.

Substantial thought and discussion was given to the issue of ensuring that the two resonant circuits, one for each phase of the RMF, had the same natural frequency. Care was taken to make sure that the two circuits were constructed identically, and that they saw a similar environment regarding power dissipation. Upon circuit completion, the resonant frequencies were within a few kHz of each other. The final tuning turned out to be rather trivial and consisted of connecting a large inductor in series with the RMF antenna of the circuit that had the lower frequency. This inductor, wound from standard 10 gauge wire is 6 inches in diameter by 8 inches long. After an initial estimate of the actual value needed, turns were added or subtracted until the two resonant frequencies matched. Since the value of this inductor is large compared to that of the RMF antenna, it diverts a negligible amount of power from the RMF.

## The IGBT Power Supplies

Two parallel developmental paths were initially followed in designing and building the RMF power supplies. The first consisted of tapping power out of a ringing high Q tank circuit, and it will be briefly discussed below. The second, and initially less likely to succeed approach, was to use some sort of solid state switch. However, due to the rapid advance of solid state switching technology, about a year into the project suitable switches became available. Subsequently an RMF power supply based on their design, rather than that of a ringing LC tank, was selected.

The switches used are IGBTs, isolated gate bipolar transistors. Essentially high current on-off switches, each IGBT is capable of switching 3000 amps at 1500 volts, and with rise and fall times between 50 and 100 ns, the switches can be used at frequencies approaching a MHz, though most of our testing and operation has been done around 330 kHz. These ratings are substantially outside the factory specifications, and when so operated, pulse durations need to be kept under a few milliseconds to avoid destroying the devices. It is worth noting that individual devices so operated have never failed, but there is reason to believe that such operation is pushing the IGBT's limits. The continuous wattage specifications for switching are typically 400 amps at up to 1700 volts, and at frequencies under 40 kHz. Current surges are allowable and may exceed the c.w. current rating by an order of magnitude for a few milliseconds.

The IGBTs do have some natural over current protection that takes the form of reducing the gate's impedance as the current rises. This reduction in impedance, due in part to a series gate resistance, reduces the drive voltage and allows the IGBT to reduce its current. The current reduction occurs through the development of a voltage drop across the switch, a dangerous event which substantially increases power dissipation in the switch. It is important that the IGBTs not be allowed to enter such a state. This is accomplished through the use of a higher gate drive voltage with minimal series resistance, typically 20 to 25 volts with only the switches' built in 2 Ohm series resistance. The factory recommends 15 volts with 5 to 20 Ohms, where it is assumed that this over current protection is a good thing.

Each of the two IGBT power supplies consists of twelve IGBTs run in parallel, figure 3.4. In addition to the load, the circuit has three key elements, the IGBT, the energy storage and fast capacitors, and the three component snubber. The purpose of the snubber is to minimize voltage spikes caused by the rapid switching off of current when the IGBT opens. This is accomplished by giving the current an alternate low inductance

path through the snubber capacitor and diode, a path which much more gradually stops the current as the snubber capacitor charges. Operation begins with the energy storage capacitors charged to a DC voltage $V_c$ and the IGBTs in an open state with their gate voltage held high. Charging these capacitors takes about a minute, so during actual IGBT operation, the total available energy is set by that stored on the charged capacitors, something typical of high power pulsed power supplies. Circuit point 1 is at a voltage $V_c$ and circuit point 2 is at ground. Assume for a moment that negligible voltage is dropped across the stray inductances, and that the energy storage and fast capacitors are ideal, having infinite size with no stray inductance. Understanding the voltages at points 1 and 2 characterizes the supply behavior, since the only other voltage point, point 3, the voltage across the primary of the transformer, is always at a voltage $V_c$ less than circuit point 1. Figure 3.5 shows a trace of the characteristic voltage waveform developed across the IGBTs as they are switched from closed to open to closed to open.

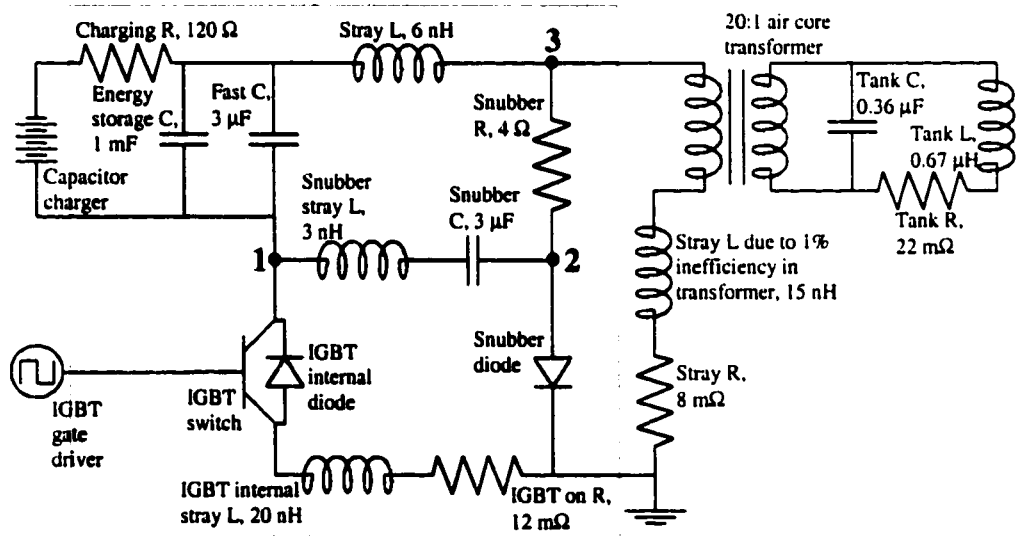


Figure 3.4 The IGBT power supply. Shaded area indicates 12 units in parallel

The discharge begins when the gate voltage switches from low to high, typically -15 to 25 volts, closing the IGBTs. Immediately, point 1 drops to ground, point 2 drops to - $V_c$, and current begins to flow through the IGBTs and the load. The snubber diode blocks this current from entering either the snubber capacitor or the snubber resistor. Due to the inductive nature of the load, this current continues to rise until the gate voltage goes low and opens the IGBTs. Ideally the current would immediately stop flowing, point 1 would return to voltage $V_c$, point 2 would return to ground, and the circuit would be ready for the next cycle. However, two additional effects, both due to changing currents through stray inductances, add their voltages to the voltage $V_c$ at point 1. The first is the immediate voltage spike induced from the switch opening. This spike is due to the 2 nH of stray inductance internal to the IGBTs, and due to the inductance the current encounters as it switches to its new path through the snubber capacitors and diodes, another 3 nH. The second is the gradual rise in voltage across the IGBT as the snubber capacitor is charged, absorbing energy from the current, and thus gradually stopping it. This energy comes from 6 nH of stray circuit inductance and from the inductance of the load.

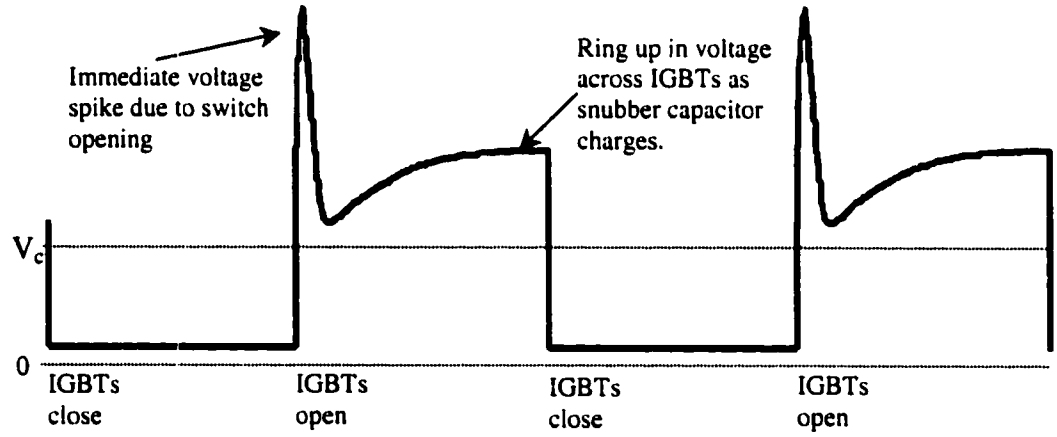


Figure 3.5 Characteristic voltage waveform developed across IGBTs

Notice that at the end of this first cycle, the voltage across the IGBTs is now greater than the charge voltage. Within about six cycles, this voltage reaches a steady state value

of about 1.5 $V_c$. The specific value reached, for a fixed stray circuit and load inductance, is set by the value of the snubber capacitor and resistor. The smaller the snubber capacitor, the higher its voltage must go in order to absorb the energy stored in the stray circuit and load inductances. The snubber resistor only plays its full roll once the voltage across the IGBTs reaches its steady state value. Now when the IGBTs are closed, the voltage at point 1 once again goes to ground, but this time the voltage at point 2 goes to - 1.5 $V_c$ instead of just - $V_c$. Since point 3 has only gone to - $V_c$, current flows through the snubber resistor and on through the IGBTs and load, discharging the snubber capacitors. The value of the snubber resistors is set such that the snubber capacitors are substantially discharged during the IGBT closed state. The final IGBT operational voltage enhancement over the initial charged voltage $V_c$ is then set by the balance between the snubber capacitor charge and discharge rates, and by the circuit inductances.

Regarding the moderately inductive nature of the load, if the tank circuit were driven with a true sine wave at resonance, the load seen by the IGBT drive circuit would appear to be purely resistive. Unfortunately the IGBT circuit is driving the tank with something more like a square wave, which not only has energy in the desired fundamental, but also has lots of energy in higher harmonics, about 50 percent according to a Fourier transform done on the actual waveform. These higher harmonics are shorted out by the tank's capacitance, which when reflected through the transformer appears as an inductance to the IGBTs. Since the tanks capacitance dissipates little energy, most of the energy stored in the harmonics ends up charging the snubber capacitors each time the IGBTs open, and is used on the next cycle to drive current, though some is wasted in the snubber resistor as it discharges the snubber capacitor. The primary concern with this extra circulating energy arises not only from the fact that it represents extra current the IGBTs have to conduct, but also that it leads to a higher voltage overshoot when the IGBTs open. Some attempt is made to limit the energy stored in the higher harmonics by driving the tank with a 40 percent duty cycle instead of the 50 percent duty cycle. Though this does reduce the energy content of the fundamental a little bit, it has a far greater impact on the

energy content of the higher harmonics. There is one unintended benefit of the voltage overshoot on the snubber capacitor. It allows the IGBT driver to be operated at a voltage higher than the maximum charge voltage of the electrolytic capacitors, at present 900 volts. The IGBT duty cycle is both a function of gate voltage as well as collector emitter voltage, so some care is required to maintain this as the circuit parameters are changed, especially when transitioning from low voltage diagnostic operation to high power operation. Increasing the gate voltage tends to increase the duty cycle while increasing the collector emitter voltage decreases the duty cycle.

Now, consider the actual behavior of the energy storage and fast capacitors. The energy storage capacitors are large electrolytics, and as such, are fairly inductive, far more inductive than all other elements in the power supply. The purpose of the fast capacitor is to bypass this large stray inductance, and thus allow for the much lower total circuit stray inductance of 8 nH, 2 nH from the IGBTs, and 6 nH from the rest of the IGBT circuit.

The fast capacitors do not hold enough charge to supply the current the circuit desires, especially the high currents initially required when the secondary tank circuit is just starting to be charged. As a result, for the first few cycles, the voltage across the IGBT actually falls, to approximately half of the normal operating voltage. However, upon seeing a lower voltage across the fast capacitors, current does flow from the energy storage capacitors, at an ever increasing rate, until the average voltage across the fast capacitors is the same as that across the energy storage capacitors. The stray inductance in the energy storage capacitors is such that it takes this current several cycles to grow to the correct value. Such a voltage drop occurs across the IGBTs any time there is a sudden increase in the current demand, i.e. a fall in the load impedance. This is only a short term limitation to the power the IGBTs can deliver, and if the load impedance stays low, after a few cycles the IGBTs will return to their normal operational voltage. Since this effect occurs on roughly half the time scale it takes for the secondary tank circuit to

charge, it partially eliminates the problem of the initially uncharged tank circuit shorting out the primary, a very fortunate occurrence. To further limit the initially high primary currents, the duty cycle of the IGBT driver could be reduced for the first few pulses while the tank circuit is charged. This is presently done on the TCS RMF tube based power supplies, and it will likely be implemented on the STX IGBT power supplies as well.

Still, the largest primary currents do occur when the IGBTs are first turned on, and recent operation indicates that this current, approximately 2 kA per device, is at the limits of device operation as the supplies are presently configured. Previously, when the supplies were pushed, IGBTs would fail at apparently random times, not correlated with any unusually high currents, nor with any other noticeable events. Since then, all the power supply cabling has been cleaned up to minimize possible ground loops and noise pickup. The common gate drive and emitter output unfortunately makes it impossible to completely eliminate ground loops, though careful routing of wires minimizes the loop's area. The result of this improvement is that now when the IGBT supplies fail, they fail as expected, when the primary current is at a maximum during the first few cycles of operation. Each IGBT has an internal stray inductance of 20 nH. If the switch opens linearly in 50 ns when carrying 2 kA, 800 V will be developed across it, in addition to its operating voltage. If the switch opens non linearly, or faster, this voltage spike could be much larger. A failure of this type has occurred thrice at peak current since improving the supplies, and each time, the IGBT's internal diode was found to be shorted. This is consistent with too much voltage being developed across the switch since the manufacturer indicates that when over voltaged, the internal diode will break down at a slightly lower voltage than the IGBT switch itself. Individual devices so operated have not exhibited this problem, though in parallel operation, currents and switching times may not be uniform, pushing some IGBTs harder than others. This point has not been firmly established, and it is still a mystery as to why individual devices can be pushed much harder than the collective.

It is worth coming back to the issue of the IGBTs' gate resistance. In theory, increasing this resistance slows down the rate at which the gate is charged or discharged, and hence, slows down the switching speed of the IGBTs, reducing inductive voltage spikes. At times, the IGBT supplies have been operated with higher gate resistance, 15 to 20 ohms. A fast diode was placed in parallel with this resistance to allow fast switch closing, since on closing inductive voltage spikes are not a concern, though switch heating is. The slower a switch opens, the greater the internal energy dissipation. The higher gate resistance did slow down the switch openings. It also appeared to increase the jitter between switch openings, possibly increasing the inequity of current sharing. Other changes in the IGBT supplies were made as well when this was done, and since the overall supply performance did not improve, the gate resistance was removed. There was no evidence that the IGBTs were failing from being over voltaged, especially since at that point devices where being used where the internal voltage could be, and was, monitored. There was also no evidence that switch heating was, or ever has been, an issue, though based on factory specifications, the IGBT supplies are being operated not too far from where it could become one. Having solved some of the noise pickup issues that likely masked the effects of changing the gate resistance, this point deserves further investigation. Some optimization will need to occur between switch heating and voltage spikes based on desired currents and operation time.

Figure 3.6 shows characteristic waveforms from the vertical IGBT power supply in the presence of plasma. The waveforms from the horizontal supply are similar. During this discharge, the change in energy on the energy storage capacitors was $\Delta E = 0.5C(V_{initial}^2 - V_{final}^2) = 0.5(0.012\times2)(610^2-290^2) = 1530$ J which corresponds to an average delivered power of 4 MW. The typical primary power was $P = 0.5I_{primary}V_{collector\text{-}emitter} = 0.5(8000\times2)(500) = 4$ MW and the circulating power was $P = 0.5I_{circulating}V_{secondary} = 0.5(5000\times2)(6500) = 32$ MW. The ×2 is too account for both the horizontal and vertical supplies. Major sources of energy dissipation consist of the tank's resistance, ~ 1.2 MW, the IGBT's on state resistance of 1 mΩ, ~ 0.1 MW, the IGBT switching activity, ~ 0.1

MW, and the snubber resistance, ~ 2.2 MW, for a total of 3.6 MW. This leaves only 0.4 MW available for not only all other circuit losses, but plasma ionization, heating, and sustainment as well. With plasma present, the circulating voltage and current are pulled down primarily by the plasma detuning the circuit rather than by any real resistive loading. If the IGBT power supplies could track the resonant frequency, the vacuum and plasma waveforms would be nearly identical, indicating that most of the remaining 0.4 MW goes into additional circuit dissipation, not the plasma. Circuit modeling indicates a circuit stray resistance of 7 mΩ, which would account for the remaining power. All of these numbers assume no time dependence of the waveforms, and are based on measurements made at t = 400 μsec.

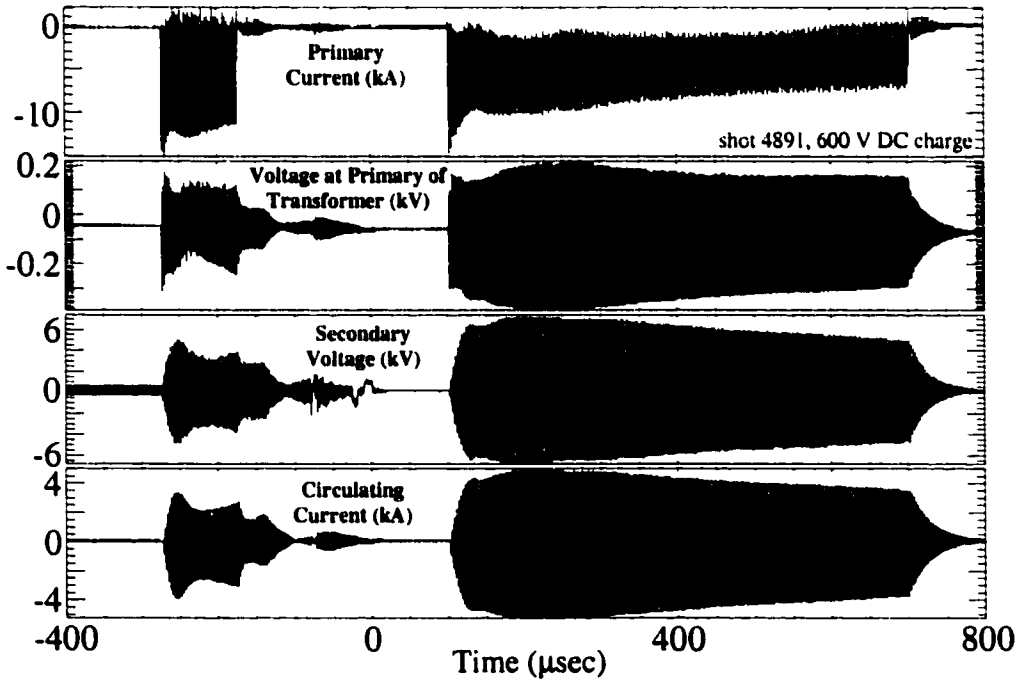


Figure 3.6 Typical IGBT primary and secondary waveforms

There are several reasons why the RMF power supplies are not operating at the power levels initially hoped. One has to do with the difference between individual and group operation. The initial hope was to operate the devices at 1500 V and 3000 A each, not the

present 1000 V and 2000 A apparent maximum. Though the capacitor banks are only typically charged to 600 V, the voltage ring up develops almost 1000 V across the actual IGBTs. Of this 1000 V, only 600 V or so is developed across the primary of the transformer, and another loss is incurred. When first turned on, the IGBTs operate at their maximum current and voltage, though during typical operation the devices operate at much lower power where each device carries only 700 A and is switched at 900 V. The drop in voltage across the IGBTs results from the drop in voltage on the electrolytic energy storage capacitors. A final substantial loss occurs in the transfer of power through the transformer due to its series stray inductance. Combining these losses, a factor of 2.2 from the individual verses group operation, 1.7 from the voltage drop getting to the transformer, 3.2 from accommodating the initial current surge, and 1.3 from the transformer, gives a factor of 15 and explains why STX is not operating at the initially planed for power levels.

Actually, if only one third of these losses were recovered, something which would be fairly easy to accomplish, then the initially planned for RMF power levels would have been exceeded. Recall in the introduction that a rough estimate of the peak real and circulating powers needed was 18 MW and 90 MW respectively. Increasing the IGBT output by a factor of 5 would bring the real power delivered to 20 MW and the circulating power to 160 MW. Hopefully this, at a minimum, will occur in the next iteration of the RMF power supplies.

Each IGBT receives its drive signal from a local driver mounted on the actual device. The close proximity is necessary since the gate has a very low capacitive impedance, and since the IGBTs gate voltage must be cleanly switched in tens of nanoseconds to avoid excessive switch power dissipation. The capacitive nature of the gates impedance makes it difficult to properly terminate a transmission line, something that would be needed with a remote driver given the rapid switching. The local drivers receive their drive signal from a local distribution driver which in turn receives its signal via a fiber-optic cable

from the master IGBT driver. Operating at its simplest level, the master driver generates the two drive signals, phased 90 degrees apart, one for each phase of the RMF. The signals consist of a series of square pulses where the pulse width is varied to control the IGBTs duty cycle. There is not a one to one correlation between the pulse width and the IGBTs on time since the IGBTs take several hundred microseconds to respond to a change in the gate voltage. It is this delay that ultimately limits the frequency at which the IGBTs can be operated. The master driver does have some more complicated modes of operation under development. These include the ability to switch the drive frequency at a particular time, the ability to slowly ramp the drive frequency, and the ability to track the tanks resonant frequency.

The circuit used to charge the IGBT's energy storage capacitors is essentially a voltage quadrupler. It was selected as a low cost means to rapidly charge the capacitors, something it takes about 15 seconds to do. The charger is very rugged and noise immune. It has no sensitive electronics and is simply controlled by being turned on and off. When the voltage falls below a set point it turns on, and when the voltage exceeds another set point it turns off. The set points are typically a volt apart, and since the energy storage capacitors draw a continuous current due to their internal leakage, the charger cycles on and off every few seconds. Mercury relays are used for the actual switching.

## An Alternate Approach to the IGBT Power Supply

The first approach to drive the RMF was to construct 2 high Q tank circuits. The basic idea was to charge a capacitor and then short it across an inductor via a spark gap, establishing an initial circulating power of several gigawatts. A small fraction of this power would then have been tapped out to drive the RMF antenna. Since the power required for the RMF falls rapidly as the electron temperature increases, an LC tank's exponential decay characteristics are well suited to delivering the initially high required

power to a cold plasma, and then a steadily reducing power as the plasma warms.

The LC tank is constrained by $\omega = (LC)^{-1/2}$, $E_{stored} = 0.5CV^2$, and $Q = \omega L/R$, where the Q requirement turns out to be the most restrictive. It is the value of Q that determines the duration of the RMF. Maximizing Q for a given $\omega$ and minimum realistic R leads one to select a large L. This in turn forces the use of a small C, which in turn drives one to a high voltage in order to maximize the energy available to the experiment. L, C, and Q were selected based on a maximum +/-100 kV charge voltage. One tank was constructed with a Q of 300, and was in the process of being debugged. The tank was static charged in oil, but the polypropylene insulation in the capacitor, rated at 3500 V/mil was being physically cracked as the oil surrounding the parallel copper plates broke down at 750 V/mil and allowed current to track along the insulating dielectric surface. The capacitor consisted of a stack of copper plates separated by 0.06 inch thick layers of polypropylene. We hoped to resolve this problem by replacing the oil with propylene glycol, resistivity of $2x10^6$ ohm-cm, and thus grade the potential parallel to the dielectric surface. The extent to which the potential can be graded, i.e. the minimum usable resistivity, is set by the high Q requirement. The effective resistive short to ground must remain large when compared to the impedance of the tank. The tank was filled with propylene glycol and readied for further, though as of yet unfinished, testing. Physically, the LC tank is 6' by 3' by 2'.

A comment is in order regarding the 3500 V/mil rating of polypropylene. Typical references usually quote a value of 600 V/mil for both polypropylene and polyethylene. Many samples of both types of poly were tested of thicknesses ranging from 2 to 30 mils using static DC voltages as well as various sinusoidal AC waveforms at frequencies around 0.75 MHz. Failure typically occurred between 2500 V/mil and 3500 V/mil, with virtually no failures below 2000V/mil, and some samples surviving to substantially higher volts per mil. The voltage hold off capacity for a single static DC charge was usually quite a bit higher as well.

The electrodes used in these tests were 10 mil thick copper plates, 10 cm by 10 cm. Electrode motion due to the shock of rapid charging and discharging, as well as localized breakdown in the oil around the edges of the electrodes posed a much greater threat to the integrity of the dielectric being tested. Each discharge would typically send an array of sparks a few millimeters long spaced a few millimeters apart out into the oil along the dielectric surface. Sharp edges on the electrodes seemed to make little difference, something which might have been expected since the oil was locally breaking down anyway. The book value of 600 V/mil is close to the breakdown value for oil, and we have a suspicion that in some of the tests which gave rise to this value, it was actually the oil which was breaking down, and possibly triggering a secondary breakdown in the poly. This was the same phenomena which was observed to occur in the LC tank filled with oil, as well as on the bench with samples of HDPE. Another possibility is that much thicker samples were tested, and that flaws within the samples lead to the lower rating. Polyethylene and polypropylene samples were obtained from various plastic supply houses and manufacturers, as well as from such things as painter's drop sheets found at local hardware stores. The plastics were all believed to be of a standard commercial quality, and except for one sample which had been deliberately perforated, they all exhibited similar hold off properties.

A comment is also in order regarding the value of Q of 300 mentioned above. It is for the capacitor and inductor alone in oil, with a copper bar in place of the spark gap switch. With the spark gap switch in operation, the tank's Q fell to around 100. Testing was begun, though never finished, as to how to decrease the spark gaps resistance by varying the gap spacing, gas type, and fill pressure. The tank's Q was also adversely effected by the presence of steel in the inductor, or in any other regions where image currents would be generated. Specifically, a steel rod was placed in the inductor that occupied around 0.2% of the inductors cross sectional area, and Q fell from 300 to 150. The drop in Q was consistent with the energy dissipated in the steel from the screening currents. In regions

where magnetic fields would be present, aluminum bolts, instead of steel, were used in the tanks construction. Further the entire tank was placed in an aluminum box to protect it from dissipative materials in its nearby environment. Clean connections are also important. The connections to either end of the copper bar used to replace the spark gap were deliberately left oily for one test. Doing this dropped the Q from 300 to 250 indicating a contact resistance of 1.6 mΩ for a sharp contact surface with a perimeter of 24 cm.

## The Transformer

The transformers match the impedance of the tank, $Q(L/C)^{1/2}$, to that of the IGBT power supplies. An intuitive way of explaining the selection of the transformers turns ratio is as follows. Because of the physical size of the RMF antenna and the desired frequency of operation, the RMF antenna has a characteristic impedance. If one wants to create a given magnitude RMF, one will need to drive a particular current in the antenna. Since the antenna impedance is fixed, the voltage necessary to drive this current is also fixed, and for this particular situation, is much greater then the primary voltage available. Thus the purpose of the transformer is simply to step up the primary voltage by the degree necessary to drive the appropriate current. The transformer's turns ratio is simply set by the ratio of the desired secondary voltage to that of the available primary voltage. If one has an ideal power supply operating at a fixed voltage, this is certainly a correct way to determine the turns ratio needed.

Unfortunately, the actual situation is a little more complicated since real power supplies can only deliver a certain power, typically with some maximum current, $I_m$, at the supplies' operational voltage, $V_o$. The greater the turns ratio, the greater the primary current drawn. Thus one is only free to increase the transformers turns ratio up to the point that $I_m$ is not exceeded. At this point, the power supply will be operating at its maximum power level, and looking into the inputs of the transformer, it will see its load

impedance as $V_o/I_m$, which is the same as its characteristic impedance. The transformer has thus matched the tank impedance to that of the power supply. In general, when one selects the transformer's turns ratio to match the impedance of the power supply to that of the load, one transfers the maximum power from the supply to the load.

Since maximum power transfer from the IGBT's to the tank circuit was desired, the transformers turns ratio was basically set by the requirement that it match the tank's impedance to that of the IGBT power supplies. Unfortunately, it was not quite this straight forward since the actually impedance of the IGBT power supplies is somewhat ambiguous. For the 12 devices in parallel, the collector emitter resistance is approximately 1 mΩ, the series stray inductance has an impedance of approximately 16 mΩ, and the impedance based on the ratio of the voltage to the current is approximately 40 mΩ. The impedance of the tank is not well established either given the sensitivity of Q to the time dependent properties of the plasma itself. In any case, based on these considerations as well as those regarding the actual transformer design described below, a turns ratio of 20 to 1 was selected.

An ideal transformer simply changes the circuit impedance by its turns ratio squared. At any instant in time the power flow into the transformer is equal to the power flow out. Such a transformer has a perfect coupling between the primary and secondary, has an infinite primary impedance, and stores no energy. Deviations from this ideal results in stray capacitance and series inductance as well as a magnetization currents. Specifically, stray capacitance arises from the proximity of windings to each other, stray inductances arise from imperfect primary to secondary coupling, and magnetization currents arise from a finite primary impedance. Both magnetization currents and stray capacitances draw additional current from the primary and result in wasted power, while stray inductances block power from reaching the load. Unfortunately, optimization of any one of these is often in conflict with optimization of another. For the circuit at hand, given the very low impedance nature of the IGBT source, the overriding constraint was that the

stray series inductance be small in comparison. The ability of the transformer to transfer power from the source to the load is related to this ratio, in very much the same way a voltage divider works.

Ignoring stray inductances that occur in the transformer's feed plates and which really have nothing to do with the operation of the transformer itself, minimizing the series stray inductance is equivalent to maximizing the primary to secondary coupling. These are equivalent since a lack of coupling is due to magnetic fields that do not link the primary to the secondary, and it is the energy tied up in these magnetic fields that gives rise to stray inductance. Ferrite is often used to enhance a transformers coupling efficiency, as well as to increase its primary impedance, since they amplify, through concentration, the flux that links the primary to the secondary relative to the flux that does not. Unfortunately, the high power and current transfer requirements made ferrite impractical since ferrite typically saturates at fields of a few kilogauss, and a very large block would have been needed to compensate. The flux that does not couple tends to occur in close proximity to individual windings, and is related to the fields natural fall off with distance from the conductor. Figure 3.7 shows a picture of the typical coupled and non-coupled field. The non-coupled field is minimized by placing the windings very close together, selecting an appropriate conductor geometry, and minimizing the total conductor length. The same things result in increased stray capacitance and decreased primary impedance, both of which require additional current from the IGBTs. The design goal was to keep both of these wasted currents under 10 percent of the total current delivered by the IGBTs. Figure 3.8 shows the actual impedance seen by the source looking through the transformer at the load, assuming perfect coupling and no stray capacitance. Notice how the transformers primary impedance appears in parallel to the reflected impedance of the load.

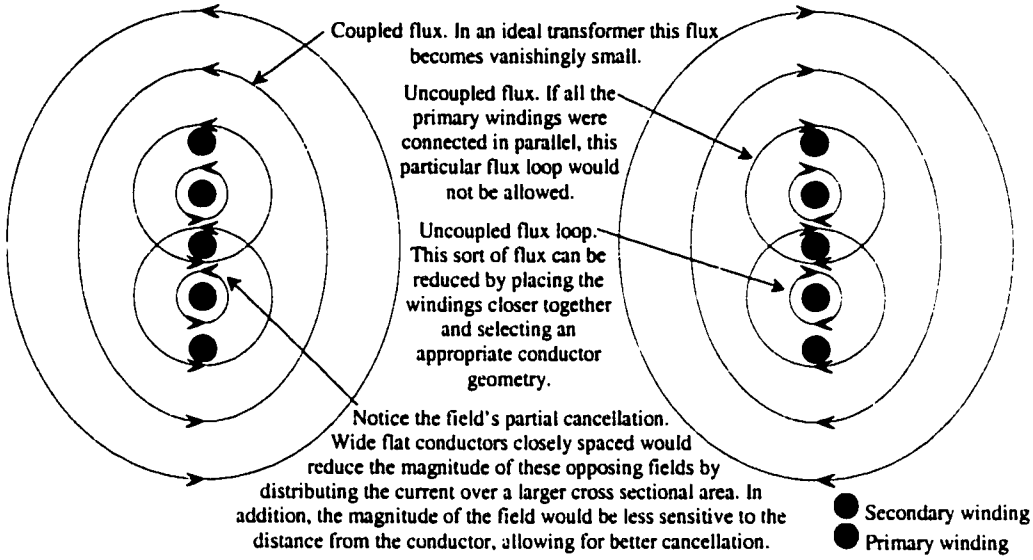


Figure 3.7 Cross section of transformer showing coupled and uncoupled flux

The transformers built are air core, 30 inch wide by 44 inch long by 2 inch thick, and have a single turn primary and 20 turn secondary. Figure 3.2 shows a cartoon schematic of this transformer with 4 of the 21 primary turns shown as well as 4 of the 20 secondary turns. The windings are made of 2.4 inch wide by 0.005 inch thick copper strip separated by layers of 0.030 inch thick polypropylene. The secondary consists of 20 loops connected in series. Separating each of these, as well as on either side, are the 21 primary turns all connected in parallel. Faraday's law, $V = d\phi/dt$, imposes the condition on the primary that the flux through each of the parallel turns be the same since they are all in parallel. In order for this flux not to couple to the secondary windings it would have to twist out of the pile, around a single turn of the secondary, and back into the pile, an occurrence which is energetically unfavorable. Further, multiple field lines doing this around different secondary turns would have their fields cancel virtually everywhere due to the strip line nature of the transformers turns, unlike in figure 3.7 where very little cancellation of non coupled flux would occur. In addition to field cancellation, the use of wide conductors spreads the current over a larger region and proportionately reduces the magnitude of the local field. Since the energy tied up in the magnetic field goes as the

square of its magnitude, reducing the field's magnitude, for a fixed current, results in substantial reductions in stray inductance.

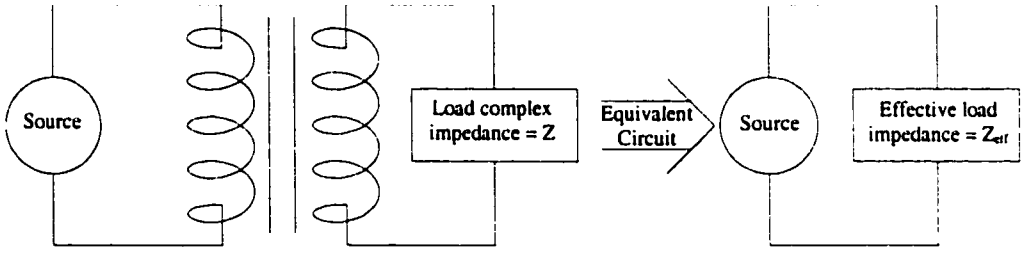


$Z_{eff} = [(a^2Z)^{-1} + (j\omega L)^{-1}]^{-1}$ = complex impedance

a = primary to secondary turns ratio, L = primary inductance, $\omega$ = operation frequency, $j = (-1)^{1/2}$

Transformer is assumed to have perfect coupling and no stray capacitance.

Figure 3.8 The effective impedance looking through a transformer at a load

Each transformer has a primary inductance of 1.5 μH, a series stray inductance of 15 nH, and a resulting coupling efficiency of 99 percent. The stray capacitance, making the worst case assumptions, drains off approximately 3 percent of the primary current, while the magnetization current drains off an additional 3 percent. At a frequency of 330 kHz, 1 nH of stray inductance corresponds to an impedance of 2 mΩ. The 15 nH of stray inductance likely arises in the transformers' feed plates. As shown in figure 3.2, the transformer's feed plates are twin lead in nature. It was realized that this was a very poor design, and consequently, the feed plates were modified to be more parallel plate in nature. However had they been originally built as parallel plate feeds, their inductance would have been much lower. One other source of stray inductance could be the corners in the windings, where the current may neck down and concentrate flux, possibly partially defeating the strip line nature of the windings. At 15 nH, this stray inductance has an impedance on order of the IGBT power supplies' impedance, and unfortunately does restrict the power flow through the transformers. This restriction has been most noticeable when a tank circuit has accidentally been shorted out during IGBT operation.

Resultant peak currents have not exceeded the initial tank circuit charging current spike by very much, indicating a strong throttling as expected by this 15 nH.

## Vacuum System

The main STX vacuum chamber consists of a 40-cm diameter by 3-m long quartz tube with a 5.1 mm thick wall. It is supported at either end by a 1.5 inch thick by 32 inch diameter aluminum flange. The flanges are in turn supported by four 2 inch diameter aluminum rods which run the length of the experiment. These aluminum rods are located at a radius of 13.25 inches and provide the basic structure on which STX is built. Attached to the flange on one end, the vacuum end, is a 16" long by 17" diameter stainless steel chamber that provides vacuum access for all the pumps, gauges and internal diagnostics. The flange on the other end is sealed with a 2 inch thick by 24 inch diameter quartz window, and is insulated to 50 kV from the 4 aluminum rods by phenolic spacers. The phenolic spacers have a much more important roll in that they break a continuous metal loop that would almost completely screen the RMF from the STX vacuum chamber.

A 3000 liter per second cryo pump pumps continuously on the 0.5 cubic meter STX vacuum chamber and keeps base pressures around $3\times10^{-9}$ T. A 50 liter per second turbo pump backed by a roughing pump are used to initially pump the system down to levels suitable for the cryo pump. Pressures are measured with a Televac controller using cold cathode, capacitive manometer, and thermocouple gauges. All valves are controlled by a Labview based control system, the same system which monitors the various pressure gauges.

Gas supply cylinders are connected to a plenum which in turn feeds the main chamber. All static fill pressures are achieved by opening and closing appropriate valves for specific time intervals preestablished in the control system. This allows for machine

operation with all the gauges powered down and electrically disconnected from the system, something which is very important given the high voltage and power nature of the experiment. During an actual shot, the 'ground' determined by the vacuum hardware has been measured to differ by up to a few thousand volts from the ground determined by the data acquisition hardware. Figure 3.9 shows a schematic of the vacuum system.

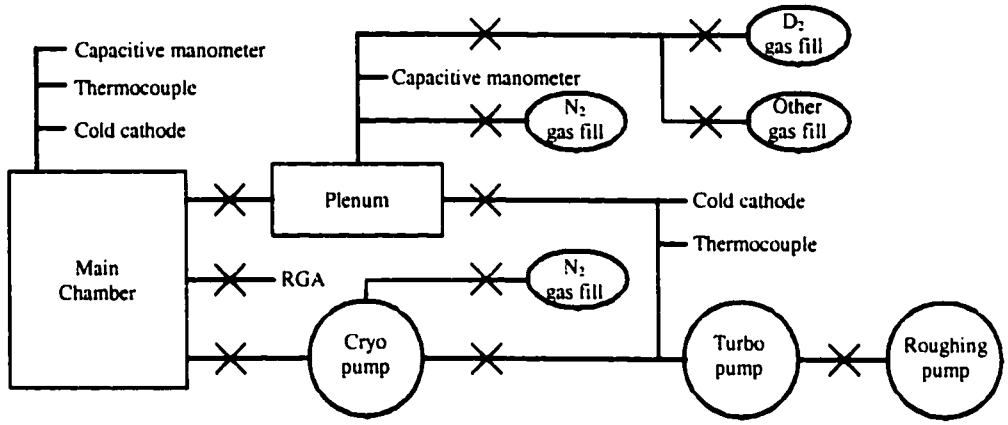


Figure 3.9 Schematic of STX vacuum system

## Control System

High speed data acquisition is done with (10) 8-channel DSP digitizers operating in Camac crates. These digitizers are 8-bit, sample at up to 10 megabits per second, and can store up to 32768 samples per channel. They have a variable full scale range from 0.5V to 5V with an offset adjustable to allow this range to vary anywhere between fully negative and fully positive. Most signals are conditioned, typically integrated or amplified, before entering the DSP digitizers. The signal conditioning hardware resides in NIM crates mounted in the same racks as the Camac crates. All of this data acquisition hardware resides in a screen room with 0.25 inch thick steel plate walls and an isolated power supply. Preferably, signals are coupled through fiberoptics to the screen room. Most of the time this is not possible, in which case great care is taken to only reference the signals to the screen room's ground. Such signals are carried in shielded cable which has been

run in a manner to minimize possible ground loops and flux coupling. From the screen room, data is transferred via a fiberoptically isolated serial highway driver into an MDS data base residing on a VMS system. Data is analyzed using IDL.

High speed trigger signals originate from 2 programmable 12-channel Jorway timing units. These have various trigger and gate options with microsecond resolution and delays of up to 17 seconds. The entire data acquisition system is triggered when the cryo pump valve starts to open. Almost immediately, the 40 MHz source is gated on. A delay of around three seconds follows while the pressure falls to the half millitorr level, at which point the vast majority of trigger signals rapidly follow. They are primarily used to control the axial and rotating magnetic fields, though a few are used to control the diagnostics as well. The DSP and Jorway units are synchronized to an external clock running at 10 MHz. The triggering of the entire system is synchronized to 60 Hz. Though the Jorway triggers have microsecond resolution, shot to shot, when run for three seconds, they have a timing jitter of a millisecond, which limits the ability to synchronize to 60 Hz. This jitter originates from variations in the external clock frequency. The Camac crate fans generate a large noise signal at about 4 times the 60 Hz frequency, and an ability to synchronize to this noise to better than a millisecond jitter would certainly be helpful. One possibility involves triggering the entire system approximately three seconds closer to FRC formation, while having Labview control the system pump down and 40 MHz preionization.

All of the low speed system control of such things as isolation relays, power supplies, capacitor charging, and vacuum system operation, is done with a Group3 Control Net data acquisition system operating on Labview NT. This is a system explicitly designed to operate in a pulsed power environment. It utilizes fiberoptic isolation, signal conditioning, and error detection and correction software. Precautions similar to those taken to protect the high speed data acquisition system are also taken to protect this system. Signals are optically isolated, disconnected during machine firing, or transmitted

along shielded, electrically isolated and carefully placed cable. The system has a capacity of 72 digital I/O signals, 16 analog in signals and 8 analog out signals, around 80% of which are in use. Typical communication times take around a few milliseconds. At present, minimal effort has been put into programming the control system, and it operates at a very basic level. During machine operation, a collection of independent programs are run simultaneously. These include a program for the vacuum system, a program for the IGBT power supplies, and a program for the axial field banks. Another set of programs controls digitizer initialization and data acquisition. Labview does have the capability of linking all these together, something which will eventually be done. One of the first improvements would be to add some equipment protection logic to prevent things like the vacuum system from accidentally being opened to air.

**Magnet System**

Fifty-six single turn epoxy coated magnets spaced 5.0 cm apart run the length of the experiment and are used to create the various axial field configurations. The magnets have an inside diameter of 45.21 cm and an outside diameter of 59.69 cm. They have an axial thickness of 0.635 cm which, when compared to the magnet spacing of 5.0 cm, gives them an 87% transparency to the RMF. Kilogauss field strengths were designed for, though due to the lack of available RMF power and subsequent low density operation, actual fields used are an order of magnitude smaller.

The magnets have been explicitly designed to allow for flexible operation. They are readily connected in series or parallel, with single or multi turn configurations, and with positive or negative polarity. A wide variety of rise times and axial field configurations are possible. At present, the central 48 are jumpered together into 12 parallel 4-turn magnets that create the main confinement field. These are powered from the central axial field current feed plate, figure 3.1. The next 4 epoxy coated magnets, two on each side, have been left disconnected. They were initially intended to create a mirror field to

prevent the FRC from drifting axially out of the machine, something which has occurred without a mirror field. They were also intended to isolate the confinement magnets from the final 2 magnets on either end which were to be used to create a cusp field for the axial discharge system. Instead, the two magnets on either end of the machine are used to create the mirror field necessary to axially confine the FRC. Placing the mirror field as far out as possible allows for a little space to observe the FRC that is not under the RMF antenna. There are two additional current feed plates located on either end of the machine to power these eight magnets in a low inductance manner. The outer most two magnets on either end are designated as the end magnets, while the next two in are designated as the mirror magnets. The central 48 magnets are designated as the confinement magnets. Axially, the center of the machine is defined to be z = 0, with z decreasing towards the vacuum end and increasing towards the high voltage end.

These three groups of magnets are collectively powered by 4 individual ignitron switched capacitor modules[9] left over from the LSX/mod machine, the A4P bank. Each module consists of a plus and minus side, each side of which can contain from one to five 14 μF capacitors connected in parallel. Ten 100' lengths of coaxial cable have been run from each module to the STX current feed plates. A wide range of circuit inductances can be obtained by connecting from one to ten of these, with or without their braids. These four modules can be collective charged to three distinct voltages, ranging from a few hundred volts to +/- 25 kV. The modules have been designated as the confinement (Cn), bias (B), smooth (S), and end (E), modules (banks), for the roles they play in generating the various axial fields.

Each ignitron module is equipped with a crowbar ignitron, as is the central current feed plate. The stray inductance through the crowbar on the central current feed plate, the master crowbar, is less than 50 nH. Each bank is capable of being triggered and crowbarred independently. Unfortunately only 6 trigger units were available for use. Three have been used as triggers for the ignitron switches, and three as crowbars. Figure

3.10 shows the circuit configuration for the confinement field magnets to which three of the four ignitron banks are connected. Figure 3.11 shows characteristic magnetic waveforms generated by each of these three modules on axis at z = 0. These waveforms were generated with the end coils energized as well as with plasma present. They are shown only to indicate the typical individual bank behavior, and the types of waveforms that were combined to generate the desired axial field. Actual amplitudes as well as start and crowbar timings have been changed. The high frequency ringing at the start of each waveform is due to the PI bank, described subsequently, being fired, while the waveform's oscillation about a varying offset arises from coupling with the end coils. The end bank is connected to the end coils and is used to generate the mirror field.

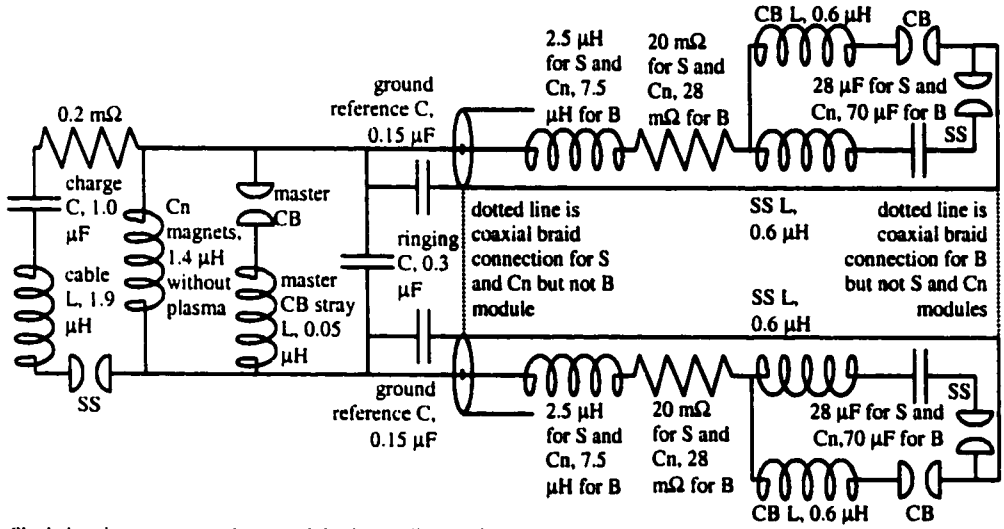


Shaded region represents three modules in parallel, the B S and Cn modules. B = bias, S = smooth, Cn = confinement, CB = crowbar switch, SS = start switch

Figure 3.10 Circuit configuration for generating the axial field

Several thousand shots were taken in an attempt to optimize the axial field. The large number of free parameters, coupled with the various coil interactions and plasma feedback, as well as the various preionization schemes, not to mention temperature and aging effects, made optimization very difficult, and greatly limited the controlled and continuous adjustability of the axial fields. The banks were not designed to produce such low, long lasting axial fields. A major improvement would be to replace this system with

a programmable IGBT driven system. Such a system using 50 IGBTs powering the coils in parallel through appropriate resistors could produce steady kilogauss fields with microsecond rise times.

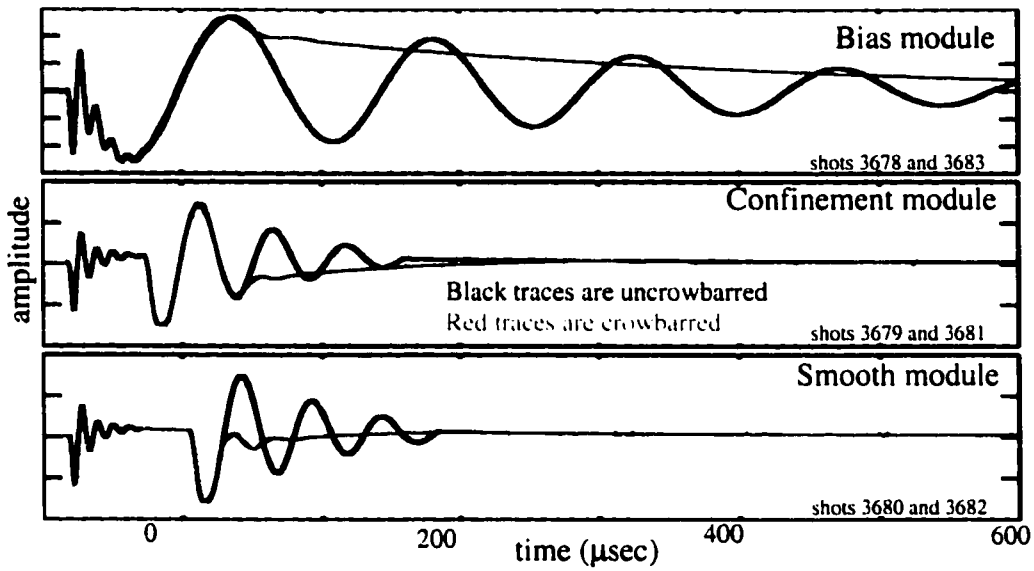


Figure 3.11 Magnetic waveforms generated by individual ignitron modules

## Plasma Ionization and Heating, Modes of Operation

One of the most difficult aspects of STX was, and still it is, achieving a suitable target plasma for the RMF. There are two distinct issues. The first is how to generate the initial seed electrons necessary to initiate the breakdown. The second is how to take a cool partially ionized plasma and turn it into a hot fully ionized plasma, a process which must occur in the plasma's characteristic Alfven time for the FRC equilibrium to be created. The initial plan was to use a kilowatt 40 MHz RF preionizer, the 40 MHz source, to generate the initial seed electrons, the first of which was dubbed Alice, and then use the RMF itself to fully ionize and heat the plasma. The presumed advantage of doing it in this manner was that the RMF would start out fully penetrated and ready to drive current, side stepping the issue of how long it takes the RMF to penetrate the plasma[17]. When the

RMF is screened, it drives little current. Such an issue will be confronted head on by the TCS experiment where the RMF will be applied to, and have to penetrate, a hot fully formed FRC. Unfortunately, the STX RMF power supplies were unable to deliver the tens of megawatts necessary to ionize and heat the plasma, so other methods were developed.

Since the power required to ionize and heat the plasma scales with the static fill density, the first approach was to simply operate at a lower static fill pressure. One millitorr required about 10 times the available power so 0.1 millitorr should have worked just fine. During initial machine operation generating Alice, the initial seed electron, as well as the subsequent breakdown did. Unfortunately, as the vacuum system became cleaner, with typical base pressures of $3\times10^{-9}$ torr, the minimum pressure at which Alice could be reliably generated increased from less than 0.1 millitorr to 20 millitorr. Further, without Alice, none of the subsequent ionization or heating methods would work. This occurred despite steady improvements in the 40 MHz source.

Initially the output from the 40 MHz source passed through a 2.5 turn impedance matching transformer and capacitor, and into an antenna running the length of the STX machine. The antenna itself was 3 meters long and consisted of the insulated center conductor from RG59 coaxial cable. The circuit was tuned to maximize the brightness of the discharge at the desired static fill pressure. For the duration of each discharge, typically tens of milliseconds, the STX quartz vacuum chamber lit up like a giant fluorescent light bulb, with a gentle purple glow. Though the antenna was broadcasting substantial power, the discharge was actually occurring through an electrostatic coupling between the plasma and the antenna.

The 40 MHz source presently in use has been designed to optimize this electrostatic discharge by maximizing the electric fields created in the vacuum chamber. This was accomplished by replacing the antenna and matching transformer with a high impedance

twin lead transmission line. The voltage, and hence electric fields, are amplified by the ratio of the transmission lines impedance to that of the source, through the buildup of a standing wave. A factor of 10 was achieved as compared to the prior factor of 2.5 gained from the impedance matching transformer. Such amplification occurs when the length of the transmission line is a half integer multiple of the source's wave length. A full wavelength transmission line was selected and run down one side of STX and back the other. This placed the wavelength nodes at either end of STX and the voltage maximums symmetrically on either side. Care was taken to make sure that the transmission line was held as close as possible to the quartz vacuum tube since the electric fields fall fairly quickly with increasing distance. The electric fields near the transmission line were strong enough to visibly break down the air outside the vacuum chamber in a darkened room. Figure 3.12 Shows a schematic of the 40 MHz source as well as a cross section of the electric fields generated. The sources frequency was tuned to maximize the electric fields in vacuum since it is the initial generation of Alice that is hardest. Once a few seed electrons are present the glow discharge proceeds readily to higher levels of ionization. The impedance and hence resonant wavelength of the transmission line do indeed change during the discharge and this results in about 25 percent of the power being reflected back into the 40 MHz supply. In vacuum, the 40 MHz source delivers 1000 W into a 50 Ω load by developing 223 V across it. Since the impedance of the twin lead transmission line is 520 Ω, this means that 2300 V is developed at the voltage maximums on either side of STX.

Though this change in the 40 MHz source created a dramatic improvement in the ability to generate Alice, it still only works reliably at pressures above 20 mT. To get to lower fill pressures the discharge is initiated at 20 mT and then, over the course of a few seconds, the system is pumped down to lower pressures, at which point the main ionization and heating mechanisms are begun. Initially when the system was dirty the glow discharge could be maintained in this manner down to what appeared to be arbitrarily low pressures. Unfortunately, as the system became clean, the discharge

extinguished itself somewhere below 0.5 mT, setting a lower operational limit. This pressure is not well-known due to the dynamics of the pump down and the lack of any reliable gauge reading in this pressure range. It is likely not even an equilibrium pressure as such. The pump down curves used to establish the 0.5 mT value deviate from the expected exponential decay, possibly due to gas evolution from the wall. If a pressure is extrapolated based solely on exponential decay, STX is being fired at a much lower pressure. The manner in which the breakdown becomes relatively insensitive to time tends to indicate that this is the case and that the pressure is dominated by flow from particles temporarily adhering to the quartz wall. Since the conductance along the length of the quartz tube is nearly equal to the conductance into the cryo pump, the flow is likely sonic without any global equilibrium pressure.

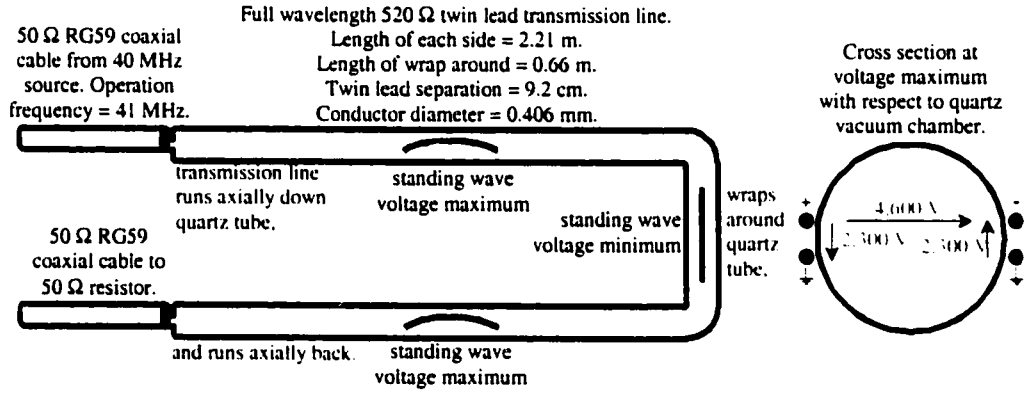


Figure 3.12 Schematic of 40 MHz source and transmission line cross section.

The next step is to fully ionize and heat this weekly ionized gas. Several different methods have been developed to do this, though the process that is actually used is a combination of these different methods. Individually, each one was insufficient, but together they achieve the desired result. The process begins with the application of an oscillating magnetic field, OMF, i.e. one phase of the RMF. Though the RMF itself works fairly poorly at ionization, the OMF works quite well. A burst from the vertical supply is followed by a burst from the horizontal in order to drain the capacitors of the two RMF supplies equally, figure 3.13-5a. This process is then followed by a rapid

ringing of the axial magnetic field about zero by the PI bank, the 4 key components of which are shown to the far left in figure 3.10. It uses ringing capacitors and inductors to apply large voltages to the confinement magnets. The larger this voltage, the larger $d\phi/dt$ is, and the greater the ionization and heating. The charge capacitor is typically charged to 20 kV, though due to a mismatch of impedances, the ringing capacitor actually achieves and then applies a much higher voltages to the axial field magnets, on the order of a factor of 2 or so larger than initial charge.

At this point, the standard FRTP technique of making FRCs is employed. Though it lacks any ability to sustain the FRC, it is great at ionizing and heating the plasma, even at the very low voltages used in the STX device As a point of comparison, FRX-C[21] operated with a loop voltage of 42 kV/m, LSX operated with a loop voltage of 12 kV/m, and STX forms FRCs with a loop voltage of 2 kV/m. An initial bias field is introduced into the plasma and then this field is rapidly reversed forming a conventional FRC. The rapid field reversal, due to impedance mismatches, once again charges the ringing capacitor. The capacitor in turn applies a high frequency short lived oscillations to the axial magnetic field. These oscillations, in the presence of plasma, are rapidly damped, creating additional heating.

Depending on the specific selection of timings and amplitudes, the rapid field reversal will result in an FRCs of various quality, ranging from those that die so quickly they are barely detectable to one's lasting for nearly 100 μsec. The RMF has been applied to the better of these FRCs, and the results will be discussed later. Usually the full RMF is applied 100 μsec later, during which time all field reversal typically decays away and the plasma settles into a more quiescent state. Additionally, axial flow out the ends of the machine may be important in further reducing the plasma density. The effects of varying these timings have barely been studied and could certainly use further investigation. Having achieved full ionization, the plasma is then ready to become the target of the

RMF. Figure 3.13 shows a time history of the relevant magnetics along with a summary of the steps described above.

An axial discharge system was also constructed to help heat and ionize the plasma. 12 stainless steel plates containing 6 stainless steel electrodes, each of which is 3 mm by 3 mm by 25 cm long, are placed in an annular arrangement with a mean radius of 33 cm and width of 10 cm at either end of the STX vacuum chamber. The electrode tips are located between the mirror and end coils. The electrodes on the vacuum end of STX are in good electrical contact with the metal flanges and equipment of the vacuum system, i.e. ground, while the other set of electrodes is in good contact with the aluminum flange which comprises the high voltage end of STX. The power supply consists of a 4 μF capacitor capable of being charged to 25 kV. A spark gap switch connects this capacitor to 4 identical coaxial cables which in turn are connected to either end of STX. The braids of these cables are terminated on the vacuum end of STX, while the 4 center conductors run down the length of the machine, symmetrically placed at a radius of 61 cm, and connect to the high voltage end of STX. These cables are properly terminated, each into a 35 ohm coaxial carbon composition resistor, in order to help avoid the hazards possible voltage ring up could cause the internal probe.

Initial operation showed the axial discharge to be very effective at ionizing and heating the plasma. Unfortunately, there were some side effects which rapidly led to its disuse. The time at which the axial discharge would break down the plasma was very erratic and the breakdown itself was not very reliable. Further, its use caused the IGBT power supplies to stop operating, likely due to some sort of noise coupling. By far the most serious problem involved the axial discharge arcing to and destroying the internal magnetic probe, a very important, delicate, and difficult to construct diagnostic. Through static testing outside the vacuum chamber, the internal probe was believed to have a sufficient voltage hold off capacity, though measurements of the actual voltages developed within the plasma were never made. It was assumed that the coaxial cable

termination resistors would limit the voltage to that of the initial charge. Either the voltage hold off ability of the probe changed in the presence of plasma, or the actual applied voltages were much higher. In any case, these problems led to the discontinued use of the axial discharge system and to alternative ionization and heating methods being developed. The system has been kept around since it does allow for a very interesting experiment, the introduction of toroidal fields into an FRC, an experiment we hope to perform at some point.

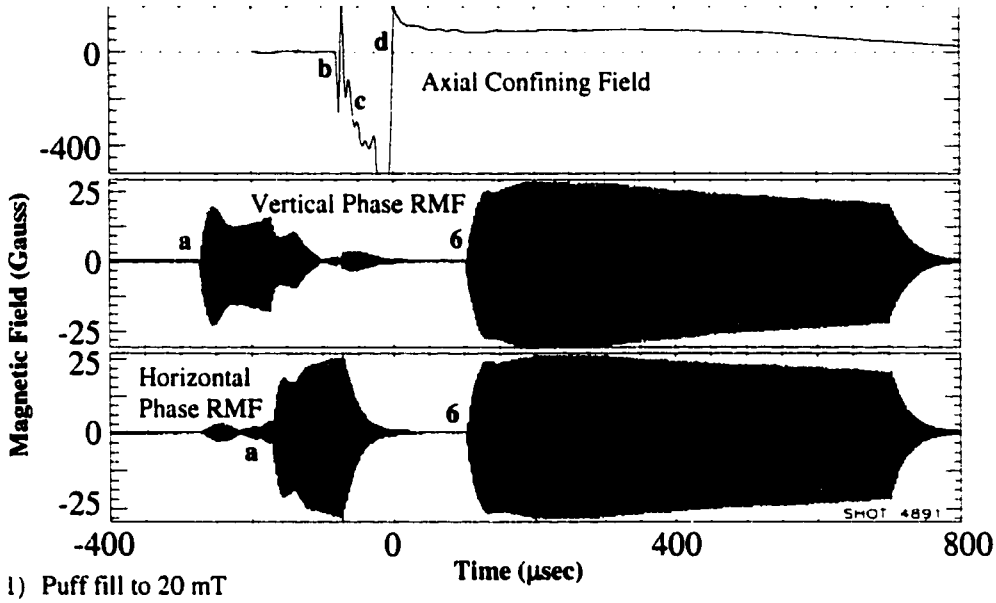


1) Puff fill to 20 mT
2) Turn 40 MHz source on at -3.0 sec
3) Open cryo pump gate valve and start system pump down
4) Fire STX when pressure reaches desired level, typically 0.4 mT
5) Ionize and heat plasma with:
   a) individual phases of RMF
   b) ringing of axial field with PI bank
   c) introduction of reversed bias field
   d) rapid field reversal
6) Form and sustain FRC with full RMF

Figure 3.13 Time history of STX magnetics.

One additional heating system has inadvertently been partially developed, the high Q LC tank circuit described above. It could be used as an Alfven heater by driving an m=0 k=0 Alfven wave. The wave would be driven by connecting the tank to the axial field magnets where it would add a 0.5 MHz AC component to the DC confinement field.

Numeric simulations indicate that this should result in rapid ion heating due to the wave being heavily damped by the 2-D radial and axial FRC oscillations. The rapid ring down of the ringing capacitor in the presence of plasma is believed to be an example of this sort of heating, though at much lower power levels. Rather than driving the entire axial field magnet set, a better approach might be to apply such an oscillating field to just the mirror magnets at either end of the machine. Periodically squeezing the ends of the FRC should drive a similar wave, and it may be less of a perturbation to the equilibrium than oscillating the entire axial confinement field. Further, combining such a high voltage oscillating circuit with the mirror field should be easier than combining it with a programmable low voltage axial field system.

# CHAPTER 4
# STX DIAGNOSTICS

## The Internal Magnetic Probe, Physical Description

The most important diagnostic on STX is the internal magnetic probe. The probe consists of a chain of 24 magnetic pickup loops wound from 50 micron diameter copper wire. Each pickup loop is approximately 1.1 cm long by 0.15 cm wide and is composed of eight individual turns of the copper wire. The leads to each of the pickup loops are also made from this thin copper wire and have been twisted with about 10 twists per cm in order to reduce stray flux coupling. The pickup loops are joined together in exactly the same manner as links in a chain, and consequently, adjacent loops are nearly orthogonal.

The chain of 24 individual magnetic probes, along with the leads, are housed in a beryllia tube 27 cm long with a 0.2 cm outside diameter and a 0.15 cm inside diameter. The leads to the probes run down the length of the beryllia tube and out the lower end into a quartz tube parallel to, and resting in, the bottom of the 40.5 cm diameter STX vacuum chamber. The beryllia tube is affixed orthogonally to this quartz tube and pokes radially up into the STX vacuum chamber, passing through the $r = 0$ axis of symmetry. The tip of the beryllia tube is capped with a small piece of boron nitride approximately 0.75 cm long with a 0.3 cm diameter. Through pulling the quartz tube, the probe can be translated axially along the length of the STX vacuum chamber, from the center of the machine all the way down to the vacuum end. Rotating the quartz tube rotates the probe side to side, though measurements were never made with the probe in any position except pointing vertically up into the STX vacuum chamber and passing through the axis of symmetry. Figure 4.1 shows a schematic of the probe's positioning in STX.

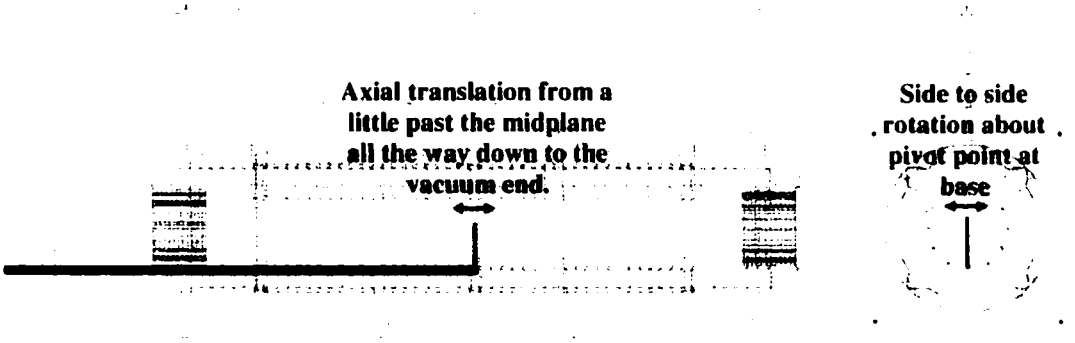


Figure 4.1 Positioning of the Internal Magnetic Probe

Since the individual pickup loops have no sensitivity to magnetic fields running along their length, keeping the probe in this orientation eliminated all sensitivity to the vertical component of B, or in this case, all sensitivity to the vertical component of the RMF. This leaves the probe with a sensitivity only to axial components of B, the axial field, and the transverse components of B, the horizontal component of the RMF. Within the beryllia tube, each probe was oriented to have a sensitivity to both the axial and transverse components of B. Table 4.1 shows the orientation and location of each of the pickup loops.

The interpretation of data becomes much nicer when one considers that the probe also lies along a radius. In cylindrical coordinates, this means that the magnetic probe has no sensitivity to radial components of B, but does measure azimuthal and axial components. Since the probe lies along a special radius, the vertical radius, ideally there is a one to one correspondence between the horizontal component of the RMF in Cartesian coordinates and the theta component of the RMF in cylindrical coordinates.

Using cylindrical coordinates simplifies data analysis, though it assumes that the vertical and horizontal components of the RMF have equal amplitude, something which in theory is true by definition. Unfortunately, the actual RMF is created from a horizontal and vertical component, and in vacuum, depending on the frequency and

amplitude of operation, the vertical and horizontal components of the RMF have been measured to differ in amplitude by as much as 20 percent. Even though throughout much of this thesis the probe will be analyzed and discussed as if it were actually measuring the azimuthal component of the RMF, one needs to keep in mind that this is an assumption, and that what is actually being measured is the horizontal component of the RMF. In the presence of plasma this assumption may be fairly good since only a true RMF can penetrate past the classical skin depth. Thus, this distinction may only manifest itself in vacuum or at the edges of the plasma. Since we do not have another probe lying along the horizontal radius to simultaneously take measurements, we cannot verify that this is true, though the physics of the problem certainly indicates that it should be.

Table 4.1 Location of Individual Internal Probe Coils

| coil # | degrees clockwise from z axis | radial location of center of coil (cm) | coil # | degrees clockwise from z axis | radial location of center of coil |
|---|---|---|---|---|---|
| 1 | 65 | -5.2 | 2 | -20 | -4.2 |
| 3 | 73 | -3.1 | 4 | -22 | -2.0 |
| 5 | 55 | -0.9 | 6 | -25 | 0.2 |
| 7 | 45 | 1.2 | 8 | -30 | 2.3 |
| 9 | 54 | 3.4 | 10 | -35 | 4.4 |
| 11 | 53 | 5.5 | 12 | -45 | 6.6 |
| 13 | 38 | 7.7 | 14 | -40 | 8.7 |
| 15 | 40 | 9.7 | 16 | -30 | 10.8 |
| 17 | 35 | 11.9 | 18 | -32 | 12.9 |
| 19 | 34 | 14.0 | 20 | -16 | 15.2 |
| 21 | 63 | 16.2 | 22 | -20 | 17.1 |
| 23 | 62 | 18.2 | 24 | -13 | 19.2 |

## The Internal Magnetic Probe, Electronics

The internal magnetic probes operate on Faraday's law, $V_{out} = Nd\Phi/dt = NAdB/dt$, where $V_{out}$ is the voltage developed around a single turn of the probe, N is the number of turns in the probe, $\Phi$ is the flux through the probe, A is the probe area, and B is the

magnitude of the magnetic field. Flux penetrating the loop generates a loop voltage proportional to the change in flux. The signal from these probes is electronically integrated to provide a direct measure of the magnetic field, $B = (1/NARC)\int V_{out}dt$, where R and C are the resistor and capacitor values used to accomplish the integration. Figure 4.2 shows a schematic of the circuit used. It consists of a 20 microsecond integrator followed by a times 20 amplifier. Such a high gain circuit is needed due to the very small size of the magnetic probes and to the need to accurately measure small changes in small fields.

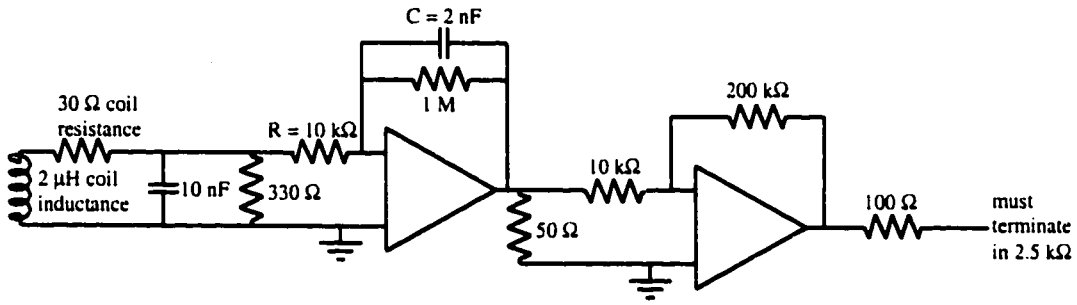


Figure 4.2 The Internal Probe Integrators and Amplifiers

Typical axial fields in STX have an amplitude of 100 G with a few hundred microsecond rise and fall time, while typical RMF fields have an amplitude of 25 G with a microsecond rise and fall time. At the input to the integrators, the axial fields generate peak voltages of a few millivolts, while the RMF generates peak voltages of several hundred millivolts. At the output of the amplifiers, these each produce typical maximum voltages of a few hundred millivolts. Since the digitizers used have a peak sensitivity of 2 mV per digital count, the internal probe should be able to measure STX fields down to the Gauss level. In reality, signal noise limits the probe's resolution to a few Gauss.

The environment in which the probes operates is harsh. They are embedded in a plasma being driven by a multi megawatt and kilovolt RF power supply, in addition to being exposed to all sorts of high voltage and current switching noise. In this

environment the probes are attempting to measure millivolt signals. As might be expected, several elements have been included in the circuit to help control noise pickup.

The first is a tight twisting of all the probe leads all the way back to the BNC bulkhead feed through into the screen room a hundred feet of cable away. This twisting keeps the effective area between the twin lead small compared to the pickup area of the probe itself and effectively eliminates false signal caused to by stray flux coupling through the twin lead. The leads are even twisted at the junction between the very fine probe wire and the 24 gauge wire which runs back to the screen room, a junction which occurs about 5 ft. away from the vacuum end of STX.

The second noise control technique involves running all the leads through a thick walled copper pipe to shield them from electrostatic noise and rapid field changes. This copper shielding extends from the base of the beryllia tube all the way back into the screen room where it joins the general screen room ground, the same ground used by the probe's electronics and digitizers. It is also at this point that one side of the twisted twin lead is grounded and the signal is transferred to coaxial cable. Care is taken to make sure that this copper shield only contacts ground at the screen room, something which is done in order to avoid potentially damaging ground loops. Without this shield, or with the shield floating, electrostatic coupling is sufficient to melt the very thin probe wires at weak spots, typically at the points they have been soldered to. Many probes were lost before this discovery was made. Unfortunately, at the vacuum feed through, this copper shield inadvertently weakly contacted the STX vacuum system ground, a ground which was already defined through a very inductive path by the 480 V AC power supply to the cryo pump, and additionally, by a moderately inductive path back to hard earth ground. This inadvertent ground loop introduced noise many times the actual signal size at the RMF frequency. Prior to this contact, the screen room ground, also a moderately inductive hard earth ground, had been measured to differ from the STX vacuum system ground by several thousand volts during a shot. Though still risking a potentially large

ground loop with the 480 V AC ground, the STX vacuum system connection to hard earth ground was removed, and instead the STX vacuum system was grounded to the screen room ground through the copper housing on the probe. Converting the inadvertent ground to STX's only hard ground sufficiently eliminated this noise pickup.

The third noise control technique involves a 10 nF capacitor strapped across the probe leads at the point just inside the screen room where the transition is made to coaxial cable. This capacitor interacts with the 30 ohm lead resistance to produce an RC time of 0.3 microseconds and thus effectively shorts frequencies over three MHz. This capacitor was explicitly put in place to attenuate pickup from the 40 MHz source. Without it, the 40 MHz source would induce large offsets in the signals and would often end up railing the integrators and amplifiers. The fourth noise control technique involves terminating the output of the integrator into 50 ohms. Doing this limits its frequency of response to under a MHz, but it also makes the signal very quiet and allows the overall circuit to have such a high gain.

Three standard noise control techniques have not been included in the design of the probe. The first is the lack of an electrostatic shield over the magnetic probes themselves, and the portion of the leads contained within the beryllia tube. Such shields slow the response time of the magnetic probes to the time it takes the magnetic field to soak through the metal shield. For this reason, an insulating probe housing was selected. A very high frequency of response was desired, and sufficiently thin metal shields were both impractical to make and install given the probes very small size. Such a shield would have had to been placed inside the already crowded interior of the beryllia tube. With a few micro Henry inductance and a few hundred ohm termination resistance, the magnetic probes could respond to frequencies approaching a hundred megahertz, though at present the electronic circuit limits the frequency of response to just under a megahertz, a frequency which is adequate for the STX experiment. It is the probes very small size which inherently allows them to operate at such a high frequency since it gives

them such a small inductance. The typical STX RMF frequency is around 350 kHz, while the STX digitizers run at 10 MHz.

The second is the use of differential integrators and amplifiers. These are presently under design and will hopefully eliminate some of the noise pickup which likely arises from capacitive coupling to the probes and the portion of the leads not covered by the copper shield. Ideally, the probes should have no sensitivity to the vertical component of the RMF. In vacuum however, the signal pickup from the vertical phase of the RMF is about 25 percent of the real signal pickup from the horizontal phase. When the pickup loops and leads are shielded, the pickup of the vertical field is greatly reduced, something which indicates the pickup is coming from a capacitive coupling. Such a shielding is observed to occur when the plasma covers the probes and screens out the RMF. This still needs to be confirmed by extending the copper shield over the entire probe structure and verifying that the pick up of the vertical field does indeed go to zero.

The third is also presently under construction, and involves the use of batteries to power the probe's electronics. At present the integrators and amplifiers suffer from 60 Hz noise pickup. They have a gain greater than 10,000 to 60 cycles, and stray microvolt signals are amplified to levels where they cause problems. This is particularly true since the 60 cycles is measured to have a very large harmonic content at 4 to 6 times the fundamental frequency, which gives it a similar frequency content as the axial fields, and makes its much harder to filter out or isolate. This noise is generated primarily by the Camac crates running in the screen room. It is picked up by ground loops in the braids of the many parallel coaxial cables running from the ground at the probes input to the screen room to the ground at the integrators and amplifiers and finally to the ground at the digitizers. The use of batteries would eliminate all of these ground loops by allowing the signals to float all the way to the input to the digitizers. The copper shield that the twisted twin lead runs in would still be grounded at the screen room wall but the twisted pairs themselves would not be grounded, but would pass on through to the inputs of the

differential integrators and amplifiers floating on their battery power supply. Ground would only be defined to the signals at the output of the amplifiers at the point they passed into the digitizers. There would still be many cables in parallel with the potential to create ground loops, but they could be kept bundled tightly together to minimize this problem. Further, at this point the desired signals would be large and not susceptible to a small 60 Hz noise.

## The Internal Magnetic Probe, Probe Material Selection

In designing the internal probe for the STX plasma, the overriding consideration was that the probe be a small, and hopefully negligible, perturbation to the STX plasma. Important constraints were that the probe had to survive the plasma, that the materials needed to construct the probe were available, that the pickup loops had to be big enough to measure the field changes, and that we had to be capable of manufacturing the probe. The two free parameters available to minimize the impact of the probe on the plasma were the probe size and the probe housing material.

The first free parameter is obvious, the smaller the probe, the smaller its perturbation to the plasma. To estimate this perturbation, we simply assumed that plasma would be free to flow to the probe at its sonic speed, $C_s = (kT_e/m_i)^{0.5}$, and that all the energy of any particles reaching the probe would be lost. The characteristic energy of the particles reaching the probe however, can be several times their typical energy in the equilibrium plasma, though this possibility will be ignored in the following discussion and comparison. The reason for the increase in energy of the particles reaching the probe surface has to do with ambipolar diffusion and the development of a sheath which accelerates the ions into the probe, and which only lets the highest energy electrons through. Further, if the probe oblates and contaminates the surrounding plasma, radiative losses can become enormous. On the other hand, an insulating sheath can develop that slows the flow of particles and energy to the probe, something which was believed to

have occurred on most of the materials tested in the TRAP[22] plasma, and which will be discussed subsequently.

Since each particle has 1.5kT of thermal energy and 1.0kT of compressional energy, the energy flux to the probe is $2.5C_snkT$, where n is the electron density and T is the electron temperature. In STX, the ions are cold in comparison and their contribution can be neglected. With a typical average radial density of $2\times10^{18}$ $m^{-3}$ and temperature of 60 eV, 250 $W/cm^2$ are delivered to the probe. With a probe surface area of 15 $cm^2$, this corresponds to a total drain on the plasma of roughly 4 kW, a small but non negligible load compared to the average power flow into the plasma from the RMF. The eventual size of the probe was determined by the size of the smallest probe housing we could obtain in an appropriate material, in this case the beryllia tubing. As a point of comparison, the probe housing has a radius of 1 mm, while the plasma Debye length of 0.04 mm, an electron gyroradius of 2 mm, and a few eV ion gyroradius of 20 mm in the typical 100 G STX fields. R. H. Lovberg[16] provides a much more thorough discussion of these and subsequent issues which have only been sketched out here in an approximate manner.

The selection of the probe housing material was more complicated, though in the end we simply selected the best material available. We began the process by considering how the probe material would likely react to the energy flux from the plasma, and by considering what material properties would optimize this response. There are two general sorts of responses to the incident heat flux. Either the probe can absorb the heat and transport it away from the surface, or the probe surface can shed the incident energy through vaporization. Since it was essential that the probe not contaminate the plasma, we wanted to optimize the probe's ability to absorb and transport heat from its surface, though from the standpoint of probe survivability, vaporization certainly works quite well. Quartz and alumina are believed to behave in this latter manner.

The above analysis points towards the desired material properties, that the material has a high melting point, that it can absorb lots of heat, and that it can rapidly transport the heat away from the surface. The ability of the material to absorb energy is based on the probes specific heat and density, c and $\rho$, while the probes ability to transport heat from the surface is based on its thermal conductivity, $K$. The melting point was used as a measure of when the material would be destroyed, as opposed to the often used boiling point, since in vacuum, many materials have an unusabley high vapor pressure well below their boiling point. Possibly a more accurate assessment would have been obtained by using the temperature corresponding to a fixed vapor pressure when comparing materials.

Certainly if the entire probe melted it would be destroyed, but more often than not for these pulsed experiments it is only the surface that melts, an event which would not necessarily destroy the probe. This brings up an important point in deciding what temperature to use. There are two extremes in the way the probe can respond to the incident heat. The first is that the probe has a very high thermal conductivity and its temperature rises more or less uniformly from the incident heat flux. Were this the case, the probe would certainly be destroyed at its melting point, though a more important temperature to consider would be the temperature at which the probe's innards melts. Most wires along with their insulation melt at temperatures far below that of the refractory probe housing. At the other end of the spectrum, the interior of the probe does not know about the incident heat flux until long after it has stopped. In this case surface melting would likely not destroy the probe, and the more appropriate temperature to select would be based on when the probe material starts to contaminate the plasma. The criterion used to decide which is more relevant is based on the relationship between the duration of the heat flux and the time it takes for the heat to fully penetrate the probe. Based on the heat equation, $(K/\rho c)\nabla^2 T = \partial T/\partial t$, a characteristic penetration time is given by $t \sim \rho c x^2/K$, where x is the characteristic penetration distance.

With the above discussion in mind, a figure of merit, $K\rho cT_{melt}^2$ was assigned to each of the materials consider. The larger this number the greater the given materials ability to withstand the heat load and not be damaged nor contaminate the plasma. Table 4.2 lists the properties of a variety of materials along with this figure of merit. Not accounted for in this figure of merit, are such things as how prone the material is to cracking given a high incident heat flux coupled with a nonuniform temperature distribution, or how damaging any material that boils off is to the plasma, among many other possible considerations. In terms of impurities radiation, the low Z elements are certainly far less damaging than the high Z elements, and consequently for an equivalent impact on the plasma, far more of a low Z material could be allowed to vaporize and enter the plasma.

Table 4.2 A Comparison of Materials

| | $T_{melt}$ (°K) | $\rho$ (g/cm$^3$) | $K$ (W/°Kcm) | c (J/g°K) | $T^2K\rho c$ |
|---|---|---|---|---|---|
| | | | | | |
| Tungsten | 3700 | 19.0 | 1.80 | 0.13 | 60.9 |
| Molybdenum | 2900 | 14.0 | 1.50 | 0.25 | 44.2 |
| Copper | 1400 | 8.9 | 3.90 | 0.38 | 25.9 |
| Tantalum | 3200 | 17.0 | 0.55 | 0.17 | 16.3 |
| Gold | 1400 | 19.0 | 3.00 | 0.13 | 14.5 |
| Platinum | 2045 | 21.5 | 0.73 | 0.13 | 8.5 |
| Aluminum | 1000 | 2.8 | 2.40 | 0.90 | 6.0 |
| Titanium | 2000 | 5.0 | 0.20 | 0.65 | 2.6 |
| Inconel | 1700 | 8.2 | 0.30 | 0.20 | 1.4 |
| Indium | 450 | 7.3 | 0.80 | 0.23 | 0.3 |
| | | | | | |
| Diamond | 3800 | 3.5 | 26.00 | 0.52 | 683.3 |
| Berylium Oxide | 2800 | 3.0 | 2.60 | 1.00 | 61.2 |
| Boron Nitride | 3300 | 2.2 | 1.80 | 0.71 | 30.6 |
| Aluminum Nitride | 2300 | 3.3 | 2.00 | 0.71 | 24.8 |
| Silicon Nitride | 2200 | 3.4 | 2.20 | 0.63 | 22.8 |
| Graphite | 3600 | 2.0 | 1.50 | 0.50 | 19.4 |
| Magnesium Oxide | 3100 | 3.6 | 0.50 | 1.10 | 19.0 |
| Silicon Carbide | 2700 | 3.2 | 0.43 | 1.40 | 14.0 |
| Tantalum Carbide | 4600 | 14.0 | 0.22 | 0.17 | 11.1 |
| Boron Carbide | 2700 | 2.5 | 0.28 | 0.92 | 4.7 |
| Aluminum Oxide | 2300 | 2.6 | 0.26 | 0.80 | 2.9 |
| Silicon Oxide | 1900 | 2.6 | 0.02 | 0.74 | 0.1 |

Fortunately, in addition to these theoretical considerations, the TRAP experiment provided an ideal facility to actually test various probe materials and evaluate their impact on a plasma in a much more challenging environment. Unlike the 60 eV $2\times10^{18}$

STX plasmas, the TRAP plasmas were 120 eV at densities of $5\times10^{21}$. To make matters worse, they were translated across the test materials at velocities of $1.2\times10^{5}$ m/s. At these speeds, the plasma's translational energy was 1/3 of the internal energy, where the internal energy consisted of a 1.5 kT thermal component plus a 1.0 kT compressional component. The plasma was passing over the test material at 15% of the sound speed, and virtually all visible surface melting occurred on the side of the material facing the oncoming plasma. The corresponding energy flux was roughly 5 MW/cm$^2$. The plasmas were a couple of meters long and had a dwell time on the probe material of around 10 microseconds.

Quartz, alumina, beryllia, and molybdenum were tested. 20 cm long pieces with 1 to 2 mm diameters were poked radially into the vacuum tube through which the TRAP FRC was translated. Only one material was tested at a time. Several cleanup shots were typically taken, and then for another few shots, the TRAP FRC was translated over the probe material. The quartz and alumina destroyed the plasma immediately, with virtually all the plasma energy and field reversal being lost before the end of the plasma had even finished passing over the probe material. The intensity of the impurity radiation blew the measuring bolometer off scale as soon as the plasma contacted either probe material, though rapid photo imaging showed the alumina to take at most a couple of microseconds longer to light up than the quartz did. This is consistent with the expected time for the surface to melt based on the measured incident heat flux shown in table 4.3. The surface melting time is given by $\tau_{melt} = 0.25\pi K\rho cT^2/P^2$ [16]. P is the incident energy flux and T is the surface melting temperature. In terms of material damage, both the alumina and quartz became a silvery gray, especially where the plasma heat load was the highest. This was more visible on the alumina than the quartz since the alumina was white while the quartz was clear. This coloration change was interpreted to mean that oxygen had been driven off leaving the heavier aluminum or silicon behind, something which was confirmed with a surface resistivity measurement on the alumina. The surface of the side of the material facing the oncoming plasma showed clear signs of melting as well.

Table 4.3 A Comparison of Materials Tested in the TRAP Experiment

| | outter radius (mm) | inner radius (mm) | density (g/cm3) | measured delta T based on thermocouple inside probe (K) | specific heat (J/gK) | incident energy to give measured delta T (J/cm$^2$) | theoretical incident energy based on sonic flow to probe (J/cm$^2$) | % measured incident energy differs from theoretical incident energy | thermal conductivity (W/Kcm) | time for probe core to know about incident energy flux (msec) | energy penetration distance for a 10 microsecond pulse duration (mm) | material melting temperature (K) | required incident energy to heat material to energy penetration depth to melting point (J/cm$^2$) | % joules to heat material in energy penetration depth differs from theoretical incident energy | time for surface to melt based on theoretical energy flux, (microseconds) | time for surface to melt based on measured incident energy flux (microseconds) |
|---|---|---|---|---|---|---|---|---|---|---|---|---|---|---|---|---|
| beryllia | 1.0 | 0.38 | 3.0 | 50 | 1.00 | 6 | 50 | 13 | 2.60 | 5 | 0.029 | 2800 | 16 | 31 | 2.45 | 36 8 |
| quartz | 1.0 | 0.50 | 2.6 | 50 | 0.74 | 4 | 50 | 7 | 0.02 | 241 | 0.003 | 1900 | 1 | 1 | 0 01 | 0 3 |
| alumina | 1.6 | 0.80 | 2.6 | 50 | 0.80 | 6 | 50 | 12 | 0.26 | 51 | 0.011 | 2300 | 5 | 11 | 0 11 | 1 8 |
| molybdenum | 1.4 | 0.76 | 14.0 | 150 | 0.25 | 26 | 50 | 52 | 1.50 | 10 | 0.021 | 2900 | 18 | 37 | 1 77 | 1 6 |

The molybdenum and beryllia did not appear to adversely affect the plasma, at least as far as plasmas decay rates were considered. For the bolometer looking directly at the probes, line radiation did increased by about an order of magnitude, though the detector stayed on scale. Like the quartz and alumina, the beryllia started radiating as soon as the plasma contacted it, while the molybdenum had a delayed response, taking around 10 μsec longer to reach its peak on the detector. Interestingly, this peak occurred in a very low density residual plasma just after the bulk of the plasma had passed over the probe. The molybdenum did have the pre existing axial FRC guide field embedded in it prior to the FRC passing over it, and since the penetration time for the magnetic field was about

twice the plasma pulse duration, these fields could have helped shield the probe from the full impact of the plasma.

The metal did suffer from one problem the insulators did not, it shorted out radial electric fields, and in so doing, drew arcs into and out of the plasma. The metal was pitted in the vicinity of these arcs. The side of the metal facing the oncoming plasma also showed signs of melting, with some sort of vapor redeposition occurring in scattered bands a few millimeters wide on the backside of the probe material. Rods of tungsten showed a similar behavior, in addition to becoming very embrittled. Being an insulator, the beryllia did not draw arcs from the plasma, but like the quartz and alumina, its surface did become somewhat gray, and like all the probes, the surface facing the oncoming plasma showed clear signs of melting. All of the probe materials developed a slight distortion, a bend, presumably due to surface melting only on one side and inducing or relieving stress. So far, the impacts of the probe materials on the plasma are consistent with the relative figure of merit assigned to each material.

A thermocouple was installed inside each of the materials to be tested, and it measured the final equilibrium temperature of the material. Since the material came to thermal equilibrium in a time short compared to radiative or conduction losses, and since the duration of the heat load was well known, the change in temperature of the material could be directly correlated with an average energy flux into the material. Table 4.3 shows this data and compares it to the theoretically expected incident energy, as well as to the maximum energy the probe should have been able to absorb based on the surface being held at the melting point for the duration of the plasma pulse, and the heat being able to penetrate a characteristic distance in that time.

All of the materials absorbed less energy than theoretically expected, with the molybdenum absorbing about half what was expected, and the beryllia, quartz, and alumina absorbing about 10 percent of what was expected. The theoretically expected

heat flux would have been expected to melt all of the material surfaces in a time short compared to the time of the incident heat flux. It appears that some sort of sheath developed that shielded the probe materials from this high incident energy flux. For the three ceramics, the effectiveness of this sheath at shielding the probes appeared to be somewhat independent of the probe material itself. It is believed that the reason that molybdenum absorbed much more heat is due to the initially embedded magnetic field reducing the high incident energy flux and thus restricting the development of a protective sheath. It took the molybdenum much longer than the other materials to start radiating, indicating the lack of such a protective sheath, or more generally, plasma contamination. With less of a protective sheath, more energy was able to reach the molybdenum's surface, and since molybdenum rates quite well as a probe material, it was able to absorb this reduced energy without generating any additional protective sheath.

Based on the measured incident heat flux, the only material surface that should not have melted was the beryllia. This is consistent with the quartz and alumina destroying the plasma while the beryllia did not. Even though the molybdenum surface rapidly melted, it's large mass likely prevented it from diffusing into the plasma. The vapor redeposition on the backside of the probe is supportive of the molybdenum boiling but not leaving the probe surface, as is the fact that that the molybdenum probe did not destroy the plasma. As to why the molybdenum radiated so brightly after the plasma had past, a possibility is that without the high surrounding plasma pressure, some of the vaporous molybdenum was free to expand into, and interact with, the hot surrounding residual plasma.

There is also evidence that vapor redeposition occurred on the quartz as well. Based on the surface being held at the melting point for 10 microseconds, the quartz absorbed 10 times the maximum energy it should have been able to absorb. The rapid melting and boiling of the quartz is certainly what destroyed the plasma, but the only way it could have absorbed the energy it was measured to have, was for the energy to have been

transferred to the probe over a much longer time than the duration of the FRC on the probe. Such a gradual energy deposition can be explained by a hot sheath slowly condensing on to the probe surface once the hot plasma was gone. Given the figure of merit for quartz, during the FRC's presence, material likely boiled off the probe surface at a rate sufficient to prevent any real energy deposition in the bulk material itself.

The molybdenum and alumina absorbed close to the maximum energy expected based on the surface being held at the melting point for ten microseconds, while the beryllia absorbed about one third of the maximum energy it could have. This is consistent with the beryllia not contaminating the plasma since, after the development of a protective sheath, it was able to absorb all of the incident energy without further melting or boiling. Even though the alumina absorbed close to the energy expected, its surface still rapidly melted and contaminated the plasma.

Using the above information, beryllia was selected as the material of choice for the internal magnetic probe housing. Fortunately, it was commercially available in the necessary size from the Brush Wellman facility located in Arizona. No other suppliers of such long thin tubes of beryllia are known of, and even the general Brush Wellman sales people will deny making such a shape. In terms of having an impact on the plasma, the probe does not appear to perturbed the STX plasma in any measurable way. Shots were taken with and without the presence of the probe, and there was never an observable difference in any of the other diagnostics based on the presence or absence of the probe, at least after a few initial clean up shots.

## The Internal Magnetic Probe, Probe Data Analysis

The goal of the two primary data reduction programs, bcalz.pro for the axial component and bcalrmf.pro for the azimuthal component, is to extract the true magnetic field signals from the contaminated raw signals. The contamination sources includes

such things as 60 cycle noise, integrator droop, and electronics induced offsets, to name a few of the known ones. Unfortunately, the contamination was sufficiently severe on some channels as to render the data unusable. Specifically, only the odd numbered loops produced usable axial field data, while the even numbered loops produced the best azimuthal field data, though some of the odd loops also produced usable azimuthal field data. The difference has to do with the loops relative orientation and sensitivity to the given fields. With some of the improvements discussed above, we hope to be abie to recover both field components from each loop, and thus effectively double the spatial resolution of the existing probe.

After applying a scaling correction to the data, the axial field program, bcalz.pro, begins by subtracting the 60 cycles contamination from the signals. During each day of operation a special vacuum reference shot is taken where nothing is fired, and only the 60 cycles is recorded on all of the channels. Enough pretrigger samples are taken for the 60 cycles to be scaled and phased with that in the actual data, and then subtracted from it. Next, a linear correction is applied to the data to help remove signal drift, drift partly due to integrator droop. At the appropriate time just before the axial field banks are fired, the signals are all shifted to have zero amplitude. Late in time, after all plasma effects have disappeared, the deviation between the internal probe signals and the known field based on the excluded flux array is calculated. A linear correction is then applied from the time of the initial zeroing to this time to remove the deviation and give all of the signals the correct amplitude at this later time. Certainly the drift in time is not linear, but this linear correction does a good first order job of removing it. The final correction the program does is to remove the RMF component from the signal. At present, due to its speed of execution, a simple smoothing of the data at the appropriate interval is used. The results were verified to be consistent with those obtained by using the more appropriate fft to remove the RMF component.

Appropriate selection of the two points for the linear correction is important. During the application of the initial OMF, before any axial fields are fired, an offset is rapidly acquired which then slowly decays away over several hundred microseconds. The first zeroing is done just after this offset is acquired, but before any of the axial field banks are fired. Unfortunately, this is a somewhat difficult point to locate, if it even exists, since the offset can continue to gradually grow on into the time of interest. The amplitude of this offset varies from shot to shot, and it is responsible for the largest uncertainty in the data. Since there is no correlation between this offset on any of the channels, the error introduced is a random error as far as radial plots at a specific time are concerned. However, this error is systematic when the field at a given location as a function of time is considered since the offset slowly varies for the duration of the entire shot, from zero early and late in time when the signals are matched to the known field amplitude. To obtain the best linear correction, the time of the second offset correction should be placed as close to the disappearance of all plasma effects on the magnetic field as possible.

Figure 4.3 shows a plot of all the axial field signals for a plasma free shot. The scatter of the lines is indicative of the absolute spatial random error as well as the absolute systematic temporal error. Four sets of vacuum shots are shown for a time period centered between the times at which the data is forced to a particular value. This illustrates not only the maximum error, but also how the error causes the various signals to move with respect to each other. From these graphs, a reasonable estimate of the error is $\pm$ 5 G. The black trace is the axial field signal used to calibrate the other traces and is measured by the excluded flux array. The reason that the other traces tend to average above this trace in the center of the plots is due to the use of the linear correction to remove integrator droop. The internal probe measurements have a greater droop then the excluded flux axial field measurements, so a linear correction based on the deviation late in time will tend to overestimate the values earlier in time midway between the two end points that have been fixed for the linear correction. This does tend to introduce a small

systematic error into all of the internal probe measurements, and the next iteration of bcalz.pro will likely use a higher order correction for removing the integrator droop.

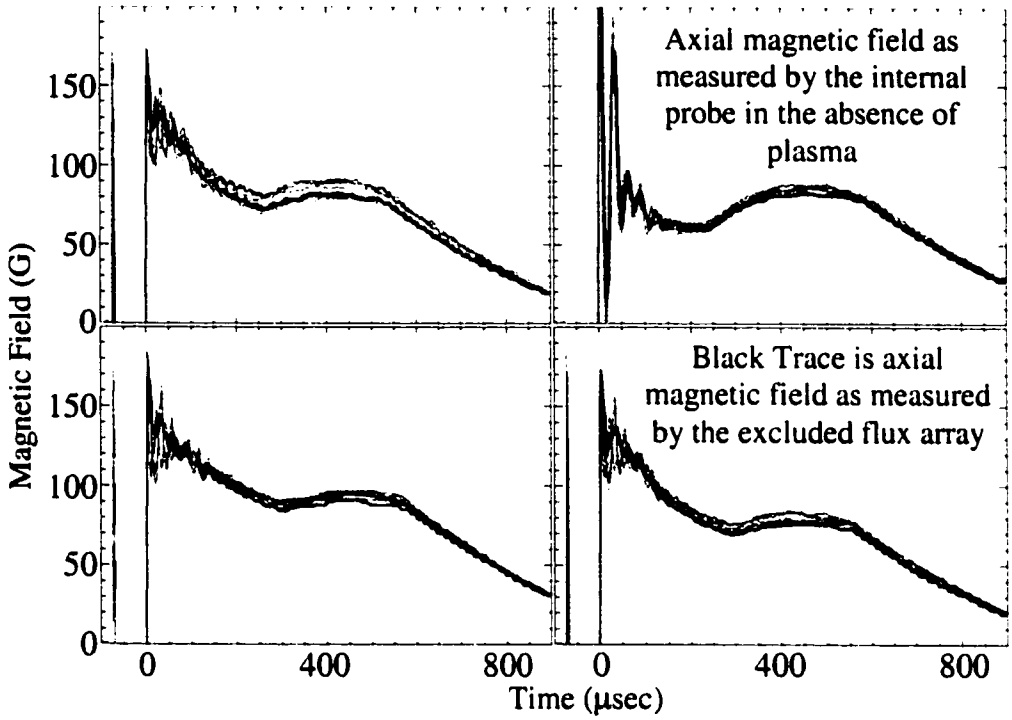


Figure 4.3 Typical uncertainty in internal probe data

The RMF program, bcalrmf.pro, generates two signals from each loop, the true theta component of the RMF, and the envelope of this theta component. The program begins by applying a smooth zeroing to the ends of the data outside the range of interest. This makes the data continuous from period to period and allows for a better fft. Next, the fft is done and the frequency range of interest is selected. Following this, the signals are scaled based on the RMF being fired in the absence of plasma, in which case the loops should all produce the same amplitude and phased signal. Only the horizontal phase of the RMF is used to generate this calibration signal since electrostatic noise pickup from the vertical supply contaminates the signals. Figure 4.4 shows this contamination for a vacuum shot. The upper traces show the envelope of the theta component of the RMF expected based on the measured current in the horizontal phase of the RMF antenna. Interestingly, the green trace should have been zero when only the vertical phase of the

RMF was fired, but when both phases of the RMF circuit were charged as was the case here, and only one phase was actually gated on and off, the other phase often had a little bit of current driven in it as well. This was not fully investigated, though possibilities include such things as one phase coupling energy into the other high Q circuit, or noise from one of the supplies gating the IGBTs in the other on and off.

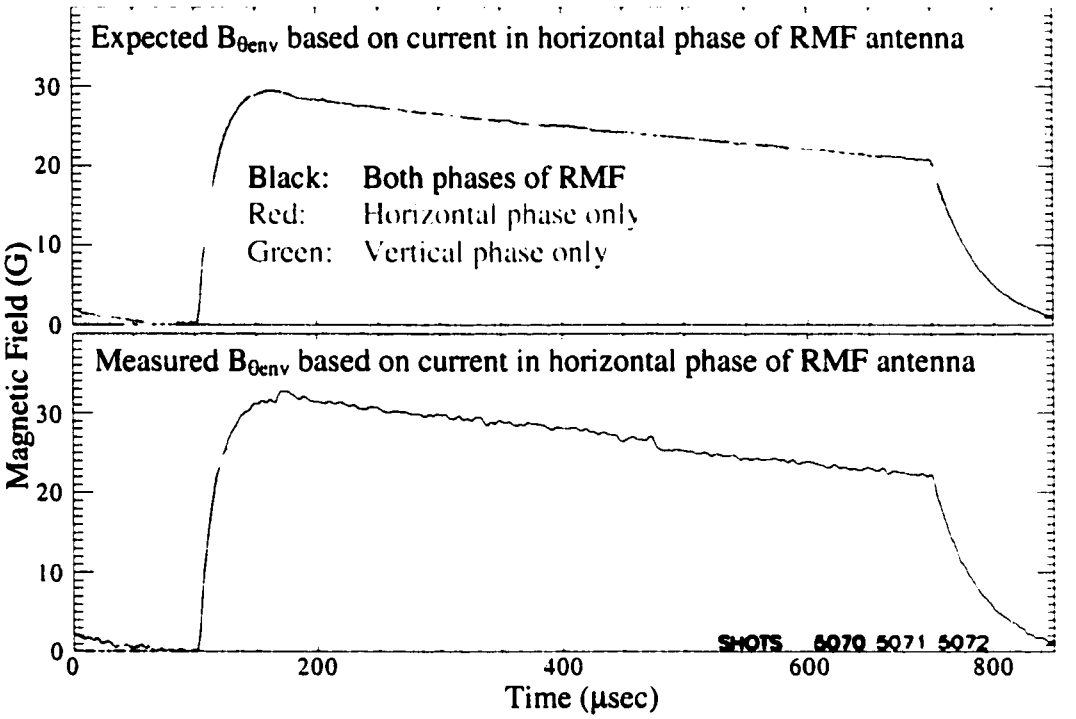


Figure 4.4 RMF noise pickup on theta component of internal probe, vacuum shot

The lower set of traces shows the measured envelope of the theta component of the RMF, $B_{\theta env}$. The firing of the vertical phase has added around a 3 G contamination to the expected signals based on the current in the horizontal antenna. This contamination likely scales with the amplitude of the vertical phase, and not that of the horizontal, so as a percentage error, as illustrated by the lower green trace, it can become rather large. Electrostatic pickup from the horizontal supply also possibly contaminates the signals, though so far, we have not explicitly addressed this issue since without plasma present, the pickup would be indistinguishable from the true field itself used to calibrate the probe. Unfortunately, the noise not only changes the amplitude, but the phase as well, and

it is sufficient to prevent any double probe matrix inversion to separate the axial and azimuthal field components, at least in vacuum where this noise is most prominent. Figure 4.5 shows traces of the RMF theta component, $B_\theta$, with plasma present when the plasma was fully screening the RMF from the traces shown. Now, a $\pm$ 2.5 G signal contamination is apparent. This is smaller than the previous 3 G since by the point in time of these traces, the vertical supply has rung down somewhat. Based on this, the uncertainty assigned to the azimuthal component of the RMF is $\pm$ 10 % of the vacuum field that would be present based on the current in the vertical antenna, or in general $\pm$ 3 G for typical operation. It is fortunate that in frequency space the axial and azimuthal field components are different enough that an fft can be used to accomplish their separation. The final step of the program is to generate the envelope signal.

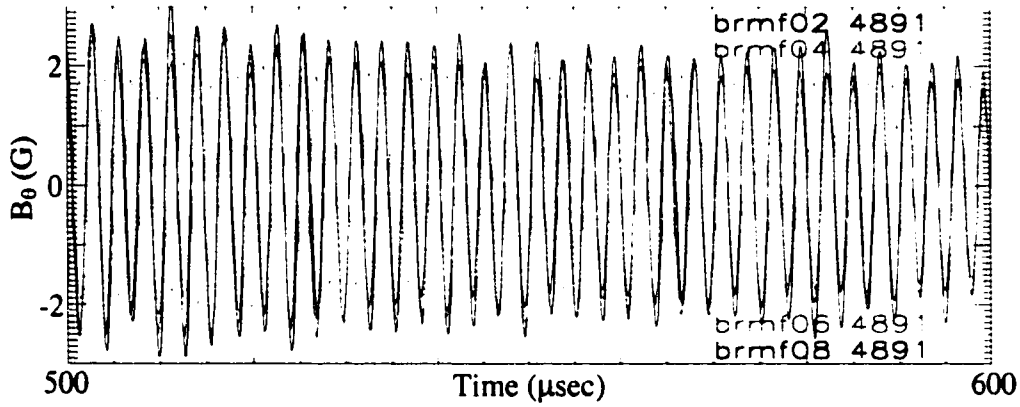


Figure 4.5 RMF noise pickup when plasma screens internal probe

## The Excluded Flux Array

The excluded flux array measures the total flux, $\phi$, through the axial field magnets, the magnitude of the external magnetic field, $B_e$, and the value of the excluded flux, $\Delta\phi$. $\Delta\phi$ is the additional flux that would be present if $B_e$ uniformly extended radially in to the axis of symmetry. These measurements can be used to calculate many useful quantities such as the plasma radius, $r_s = (\Delta\phi/\pi B_e)^{0.5}$, or the plasma energy per unit length, $E_p = B_e\Delta\phi/2\mu_o$. Such arrays have been well described elsewhere[4,25] along with the various

assumptions that are made in deriving other plasma parameters such as radius, energy, or length, and only details unique to this system will be presented here. Table 4.4 lists signal names and their axial location, as well as other pertinent circuit details, while figure 4.6 shows the balancing circuit used. Individual $B_e$ and $\phi$ measurements were made by simply removing the other loop from the circuit.

Table 4.4 Calibration numbers used in the excluded flux array

| Signal Name | Axial Location (cm) | Hoffman Box 10 Channel Number | DSP Slot Number | DSP Channel Number | Integrator Channel Number | Integrator Value (μsec) | Termination Resistance, $R_{dt}$ (Ω) | Flux Loop Resistance, $R_\phi$ (kΩ) | Signal Attenuation | Calibration Number in Transform Table | Signal Name | Axial Location (cm) | Hoffman Box 10 Channel Number | DSP Slot Number | DSP Channel Number | Integrator Channel Number | Integrator Value (μsec) | Termination Resistance, $R_{dt}$ (Ω) | Flux Loop Resistance, $R_\phi$ (kΩ) | Signal Attenuation | Calibration Number in Transform Table |
|---|---|---|---|---|---|---|---|---|---|---|---|---|---|---|---|---|---|---|---|---|---|
| FconfHV | 2.5 | 13 | 16 | 5 | 30-1 | 192 | 26.0 | 2.78 | 1.000 | -22.210 | Fconf | -2.5 | 12 | 16 | 4 | 20-6 | 188 | 25.7 | 2.76 | 1.000 | -22.880 |
| BconfHV | 2.5 | 14 | 16 | 6 | 30-2 | 192 | | | 1.000 | 1.496 | Bconf | -2.5 | 11 | 16 | 3 | 20-5 | 188 | | | 1.000 | 1.479 |
| XF07 | 7.5 | 15 | 16 | 7 | 50-1 | 55 | | 2.52 | 1.000 | 6.120 | XF06 | -7.5 | 10 | 16 | 2 | 40-6 | 55 | | 2.65 | 1.000 | 6.120 |
| XF08 | 27.5 | 16 | 16 | 8 | 50-2 | 55 | | 2.53 | 1.000 | 6.360 | XF05 | -27.5 | 9 | 16 | 1 | 40-5 | 55 | | 2.77 | 1.000 | 6.670 |
| XF09 | 47.5 | 17 | 18 | 1 | 50-3 | 58 | | 2.73 | 1.000 | 6.110 | XF04 | -47.5 | 8 | 14 | 8 | 40-4 | 52 | | 2.6 | 1.000 | 6.670 |
| XF10 | 67.5 | 18 | 18 | 2 | 50-4 | 56 | | 2.59 | 1.000 | 6.110 | XF03 | -67.5 | 7 | 14 | 7 | 40-3 | 55 | | 2.72 | 1.000 | 6.740 |
| XF11 | 87.5 | 19 | 18 | 3 | 50-5 | 58 | | 2.74 | 1.000 | 6.230 | XF02 | -87.5 | 6 | 14 | 6 | 40-2 | 58 | | 2.95 | 1.000 | 6.140 |
| XF12 | 107.5 | 20 | 18 | 4 | 50-6 | 56 | | 2.70 | 1.922 | 11.720 | XF01 | -107.5 | 1 | 14 | 1 | 40-1 | 59 | | 2.88 | 1.932 | 11.490 |
| B12 | 112.5 | 21 | 18 | 5 | 30-3 | 188 | | | 1.000 | 1.333 | B01 | -112.5 | 3 | 14 | 3 | 20-2 | 188 | | | 1.000 | 1.380 |
| F12 | 112.5 | 22 | 18 | 6 | 30-4 | 188 | 26.2 | 2.91 | 1.000 | -23.440 | F01 | -112.5 | 4 | 14 | 4 | 20-3 | 188 | 26.5 | 2.86 | 1.000 | -23.250 |
| FmirrorHV | 122.5 | 23 | 18 | 7 | 30-5 | 192 | 25.4 | 2.70 | 1.914 | -42.830 | Fmirror | -122.5 | 2 | 14 | 2 | 20-1 | 188 | 25.6 | 2.64 | 1.936 | -42.060 |
| FendHV | 132.5 | 24 | 18 | 8 | 30-6 | 188 | 25.3 | 2.75 | 1.935 | -43.600 | Fend | -132.5 | 5 | 14 | 5 | 20-4 | 188 | 25.5 | 2.64 | 1.914 | -43.360 |

The flux loops sit at a radius where they measure the total flux through the axial field magnets. The flux is given by $\phi = RCR_\phi V_{out}/R_{dt}$, where R and C are the integration resistor and capacitor, $R_\phi$ is the flux loop resistance, and $R_{dt}$ is the termination resistance. These values are known accurately enough that no additional calibration is needed. There were very slight deviations in pairs centered about the z = 0 plane believed to arise from errors in the measured values of the circuit components, and signals were scaled such that symmetrically located loops would produce identical signals. This is the reason why the calibration numbers used in the transform table as show in table 4.4 deviate slightly from what one would calculate using the above formula. The symmetry of the loop, magnet, and magnet feedplate locations dictated that the true flux had to be the same in symmetric pairs. With $\phi$ and the coil radius, $r_c$, accurately known, the loops measuring $B_e$ were calibrated with a vacuum shot by scaling the measured signal to satisfy the relation that

$B_e = \phi/\pi r_c^2$. The $\Delta\phi$ signals were calibrated by placing a sufficiently thick walled aluminum cylinder of known radius into the axial field magnets. The calibration numbers by which the $\Delta\phi$ signals needed to be scaled were calculated based on the quantity $(\Delta\phi/\pi B_e)^{0.5}$ being equal to the radius of the aluminum tube.

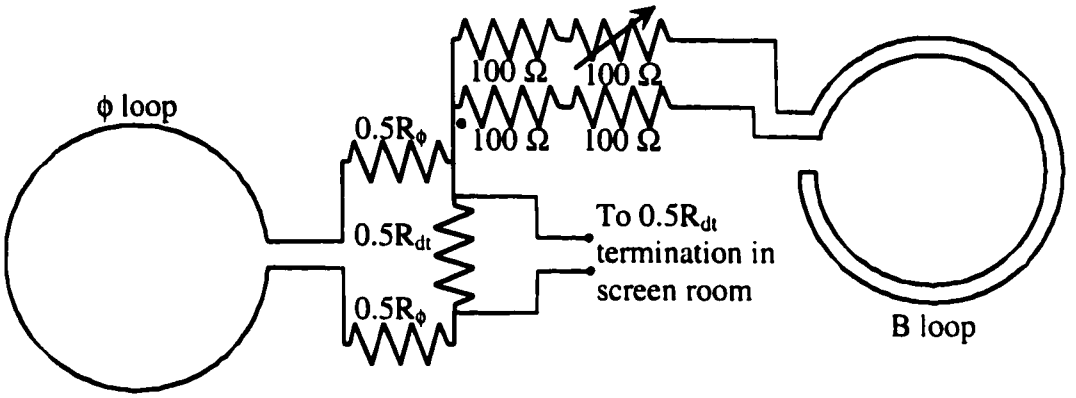


Figure 4.6 Exclude flux array balancing electronics

The $B_e$, $\Delta\phi$, and $\phi$ signals did have a slight droop in time, something partly due to the integrator droop. As with the internal probe signals, these signals were zeroed at the beginning before any fields were present, and then the appropriate linear correction was applied to zero the signals late in time once all the fields had disappeared. In addition, the $\Delta\phi$ signals had the appropriate vacuum reference signal subtracted[4]. In other experiments, the excluded flux radius $r_s$ is typically calculated based on the relationship $r_s = r_c(\Delta\phi/(\Delta\phi+\phi))^{0.5}$. However, possibly due to near field effects, i.e. the $B_e$ loops being in the near field of the individual 4 turn axial field magnets, the $B_e$ and $\Delta\phi$ measurements had an additional droop not seen in the $\phi$ measurements. By calculating $r_s$ based on $r_s = (\Delta\phi/\pi B_e)^{0.5}$, the droop was naturally cancelled. Since Be is not measured at the location of each $\Delta\phi$ loop, with the exception of the $\Delta\phi$ loops located at either end of the main confinement field coil set, a local value is calculated based on $\pi r_c^2 B_e(z) = \phi + \Delta\phi(z) = \pi r_c^2 B_e - \Delta\phi + \Delta\phi(z)$, where now the explicit z dependence is being shown. $\phi$ has experimentally been measured to be constant axially in the central 10 axial field magnets

where it is measured near the z=0 plane. However since $\phi$ once again has the different characteristic droop from $B_e$ and $\Delta\phi$, it is also replaced by $\pi r_c^2 B_e - \Delta\phi$ measured at the same central location as $\phi$ itself. The final expression used to calculate $r_s$ is thus $r_s = (\Delta\phi(z)/(\pi B_e - \Delta\phi/r_c^2 + \Delta\phi(z)/r_c^2))^{0.5}$. Though we did not implement it, a better Be and $\Delta\phi$ could be calculated based on $B_e(z) = (\pi r_c^2 B_e - \Delta\phi)/(\pi r_c^2 - \pi r_s^2(z))$ and $\Delta\phi(z) = B_e(z)\pi r_s^2(z)$ combined with this better droop free measurement of $r_s$. All of the above mentioned calibrations are done by the program xfr.pro.

## The Interferometer

The interferometer consists of a 1.06 μm Nd-Yag laser arranged in a Mach-Zender configuration. Given the low density of the plasmas, the use of a longer wavelength laser would certainly be more appropriate, but this laser was all that was available. The one advantage of using this wavelength though is its ability to pass through quartz. Given the quartz end windows on STX as well as the quartz vacuum chamber, this allowed interferometric measurements to be made virtually everywhere. Most of the time, the laser makes a double pass axially along the length of the STX device with the beam located at a radius of 14 cm, right near the FRC null. Figure 4.7a shows the long term behavior of the interferometer as it randomly drifts from fringe to fringe. Figure 4.7b shows the raw data during the time of interest with plasma present, keeping the same vertical scale as in figure 4.7a. The black trace in figure 4.7c is a zoom in, in amplitude, of the data shown in figure 4.7b to illustrate that the plasma produces a very clear though small response in the interferometer, shifting the interference by about 10 % of a fringe. The large oscillation at the end of the trace in figure 4.7b is due to the interferometer deliberately being kicked to show where the fringe extrema are. These are needed to get an absolute calibration on the fractional fringe shift induced by the plasma. Unfortunately, since the interferometer is being operated at the lower limits of its sensitivity, only when the fringe stays in its central region of peak sensitivity for the entire plasma duration is useful data collected. This corresponded to about 1 in 5 shots.

On the remainder of the shots, at some point during the time of interest, the fringe passes through a region of minimum sensitivity, and no useful data is collected. This interferometer does have a quasi-quadrature capability, but it was not implemented due to time constraints and the very small plasma induced fringe shift.

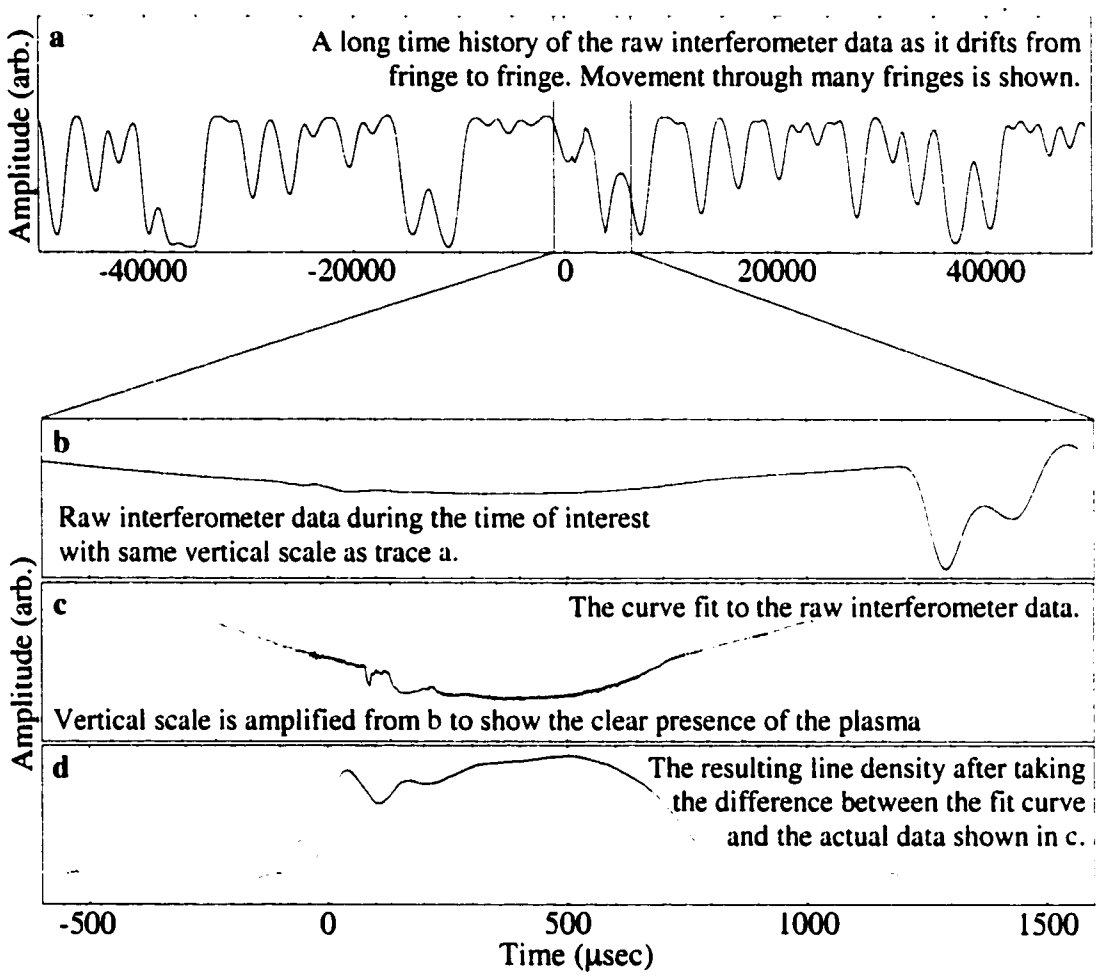


Figure 4.7 Interferometer calibration

To further complicate matters, the random drifting of the fringe has a time scale characteristic of that of the plasma duration. This prevents any simple linear correction. Instead, the drift is removed by fitting a fifth order polynomial to the data during a window of fixed duration just before the plasma is formed and after it is gone, and then subtracting it from the data. Figure 4.7c shows such a curve fit to the data, where the

data points fit to run from -550 to -200 μsec and from 850 to 1200 μsec. Unfortunately, the length of these windows, as well as how close one brings the windows to the presence of the plasma, both effect the density calculated from the interferometer data. Though one can use a general knowledge of what the plasma is doing when to help set these free parameters, there is still likely a 25 percent error in the density measurement from the curve fit alone, independent of any assumptions being made about the axial density profile of the FRC.

Twenty-five percent error bars are assigned based on the reproducibility of the interferometer reading for identical shots with various parameter adjustments being made. An error of this nature would manifest itself by slowly rising and then disappearing on the same time scale as the plasma density itself. This does mean that a good relative density comparison can be made when considering sufficiently short time intervals, or when considering densities early on in the shot, or those late in time. Also, since the curve fit error should be random from shot to shot, trends that consistently show up from one shot to the next are also believable. An example is the steady increase in density from 200 to 600 μsec shown in figure 4.8. Figure 4.7d shows the resulting line density from taking the difference of the two curves shown in figure 4.7c. Indications that the curve fit is good are that the density starts and ends at zero, that during the initial field reversal the density does not go negative, and that a curve fit to the data before any analysis is done produces the same result as one fit to and subtracted after the density has been calculated ignoring the drift. The program used to make these corrections is ddl.pro.

Figure 4.8 shows the line density for 5 identical shots where the curve fit windows were set from -475 to -225 μsec and 800 to 1050 μsec. The reproducibility of the data seems to be optimized when the program is run with these curve fit windows for the typical STX shot. It is not known whether the differences in the traces are due to shot to shot differences, or if they are solely due to errors in the curve fit, but the excluded flux traces for the same set of shots certainly show better agreement.

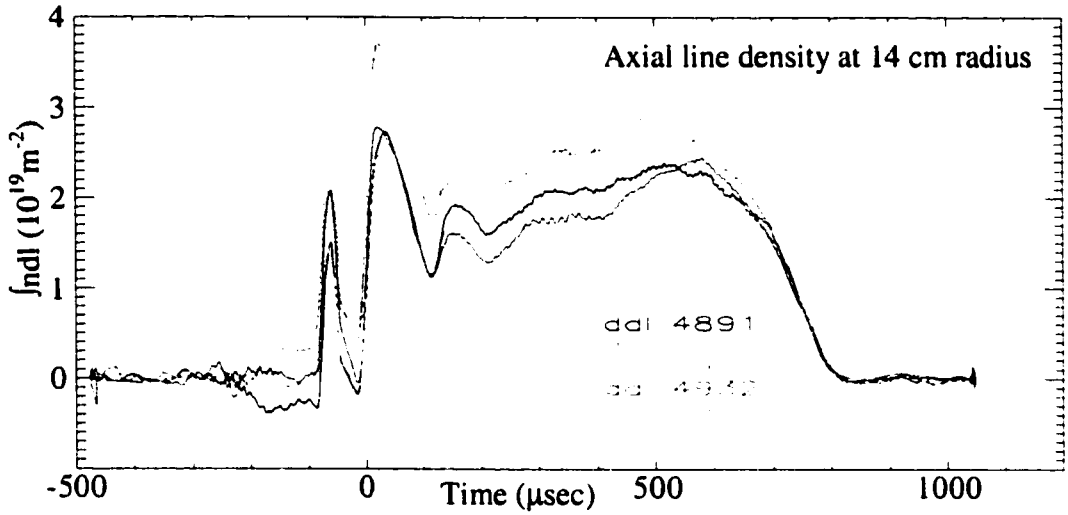


Figure 4.8 Reproducibility of measured line density for identical shots

## The Langmuir Probe

Though Langmuir probes are notoriously difficult to operate in the presence of oscillating fields, a triple Langmuir probe was constructed that could axially scan over the same region as the internal magnetic probe. The probe tips consisted of 0.5 mm diameter platinum wire housed in 2 mm diameter by 17 cm long berylia tubes. The platinum wires stuck out 2 mm past the end of the berylia tubes. As with the internal magnetic probe, the Langmuir probe could be rotated azimuthally as well, which allowed radiuses from 3 to 20 cm to be scanned. Of note in the probe electronics are an inline 23 Ω resistor and 160 μH inductor used to limit the size of arcs, L-C resonant circuits used to block changes at the RMF frequency, and dummy probe leads to cancel out capacitive effects from the long leads going to the probe tips. These components were included to help combat signal contamination caused by the RMF. The probe's bias was typically 42 V. Initially this voltage was sufficient to push the probe fully into ion saturation. However, as hotter FRCs were made, this voltage became insufficient, though it was never readjusted to a higher level. The consequence is that the Langmuir probe data is ill suited to provide absolute measurements, though fortunately, it still works well to provide relative measurements.

The Langmuir probe does suffer from one problem that initially seriously brought into question the validity of its measurements. The problem is an oscillatory pickup with a fundamental at the RMF frequency, and with an amplitude larger than the true probe signal. The amplitude of the fundamental as well as that of the higher harmonics varies depending on the probes placement within the plasma, and with no plasma present, the oscillations disappear. Upon careful study though, the oscillations do not appear to have jeopardized the probe data. First, despite the oscillations, the probe can clearly be brought into ion saturation, indicating that the oscillations do not represent a true sweeping of the probe on its characteristic I-V curve. Since the oscillations bring the probe current to zero or less often enough, independent of the probe's bias potential, that if they represented a true sweeping of the probe's potential, then increasing the probe's bias would always increase the average current collected, and ion saturation would not be reached until such time as the minimum in all the oscillations stayed well above 0. Just the fact that the oscillations made the probe current negative is indicative that they do not represent a real sweeping of the probe's potential since negative currents correspond to negative densities. Second, when the oscillations are smoothed away, the resulting ion saturation currents make sense, having the right time history, providing believable radial density profiles consistent with the interferometer, and start at and end at zero without acquiring any stray offsets. Third, the installation of the L-C blocking filters had a minimal impact on the amplitude of the oscillations. If the oscillations represented a true sweeping of the plasma potential then the L-C filters should have substantially changed their amplitude. At present, it is believed that these oscillations arise from a large common mode signal due to an electrostatic coupling to the plasma, a problem seen quite readily on the internal magnetic probe. As such, they would not jeopardize the Langmuir probe data. A simple test of this thought would have been to install a transformer into all of the probe leads that blocked common mode signals. Such a test was not done during STX operation since other possible explanations were being explored and we were not then as aware of the hazards and prevalence of common mode signals arising from

electrostatic coupling. The same can be said of the offset acquired on the internal magnetic probe signals. Having not explicitly verified the source of these oscillations, the Langmuir probe data is certainly not rock solid, though it is much more believable than it initially appeared.

## Spectroscopy

A variety of light gathering diagnostics were also employed. These included a monochronometer, an emission array, and two doppler broadening diagnostics. Of these, the monochronometer was by far the most useful. It gathered light from a chord passing through the axis of symmetry near the midplane of the FRC. It was typically set up to observe the CIII line at 2297 Å, though a variety of other lines were also occasionally looked at. CIII at 2297 Å was chosen in part because there were no substantial nearby contaminating lines, and it was readily observable. Among the dozen or so common lines scanned for, virtually no other ones were detectable during the low density equilibrium period. Many certainly never even had time to become populated. The lack of observable lines was unfortunate since the hope in scanning for them was to gain some direct information about the plasma temperature, either through line ratios, or more simply, through the line's very existence or absence. One other line was observed at 4647 Å, another CIII line. Many more lines were observed during the initial plasma ionization when the fields approached the kilogauss level and densities were much higher, but these occurred in a highly dynamic situation outside the time of interest. More lines were also visible in some of the earlier plasmas made which were formed at higher fields and densities.

Though not providing temperature information, the monochronometer did provide very useful information about the impurity level in the plasma. In a very direct way, this was accomplished by comparing signals from pure deuterium to those of deuterium doped with one percent carbon dioxide. Figure 4.9 shows these traces for the CIII line at 2297 Å. From these traces, it appears that the plasma has about a 1 % carbon impurity

level. This is after extensive plasma scrubbing of the vacuum system, described below. It is encouraging that the two traces have a similar fractional difference both during the high density and field initial ionization as well as during the plasma sustainment phase since it indicates impurities are not continually evolving off the wall at any higher of a rate than that of the $D_2$. It also indicates the field reversal at t = 0 did not substantially increase the impurity level either. In both traces, the largest peak just before t = 0 has been clipped by the digitizer, but the preceding peak allows the comparison to be made. A similar comparison was made with the 3064 Å OIV line at much higher fields and densities. Though the plasmas were very different in nature, and the vacuum system was likely not as clean as it was during subsequent operation, this test indicated an oxygen impurity level around 0.25 %. One should keep in mind though that at higher densities, proportionately fewer contaminants are swept off the wall during field reversal. An RGA was also used to examine vacuum system contaminants, and it found hydrocarbons to be by far the biggest source, particularly those associated with turbo pump oil. Subsequent examination of the system pump down procedure from air yielded a possible procedural error which could have led to turbo pump oil contaminating the system. This error has been corrected, but the machine has not been operated often enough since then to determine if it was indeed the source of carbon contamination.

The most important function of the monochronometer was to provide relative impurity information. By monitoring the brightness of a given line, CIII at 2297 Å, under some sort of standardized shot, the relative cleanliness of the system could be determined. Knowing the relative cleanliness of the system was essential since the ability to create and sustain FRCs was critically dependent on this cleanliness. Within a given shot, the monochronometer also proved useful at measuring the relative impurity level. Specifically, it very clearly indicated when the plasma struck the wall through a sharp increase in the particular line's intensity. Such events correspond very nicely with sharp increases in the separatrix radius as well as abrupt increases in the excluded flux radius. Such a spike in the impurity radiation occurred around 600 μsec and is shown in figure

4.10. Notice the lag between the time of likely wall contact, and the increase in the impurity radiation. Wall contact does not typically occur until the separatrix radius is several centimeters past the wall, as it is here.

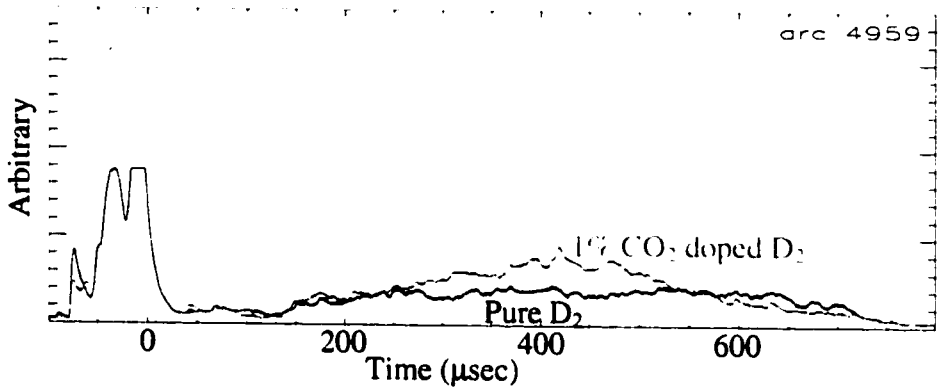


Figure 4.9 Impurity radiation at CIII 2297 Å line

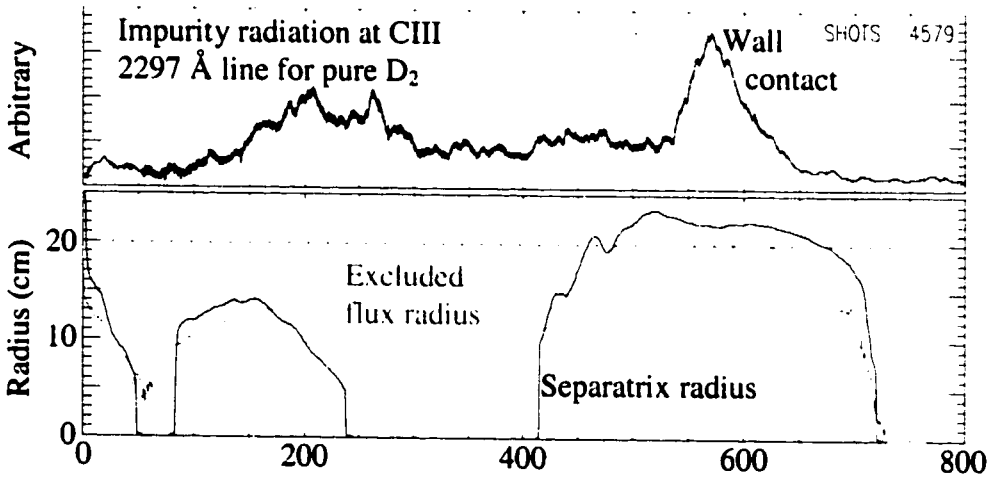


Figure 4.10 Wall contact and impurity radiation

Given the importance of the system's cleanliness, it is worth coming back to the issue. Cleaning the system typically involves several hundred shots. The axial field banks were rung to produce initial kilogauss fields while the RMF was run. Typically 3 shots in deuterium at ~ 2 mT were taken, followed by 3 shots in argon at ~ 2 mT. It took several

hundred shots of repeating the above steps to clean the system after each pump down from air. As usual, the breakdown was initiated at around 20 mT and then the system pumped down to the desired pressure before the banks were actually fired. The idea behind this method was to combine the impurities with deuterium which would chemically liberate them from the quartz, and then to use the argon to scrub the sticky hydrogen compounds from the wall. The ringing of the banks scoured the walls with plasma, while the RMF drove the particles off the wall and radially inwards. All this is just a guess as to what happened, though through trial and error, this system with these fill pressures alternated between these gasses in this manner with the axial field ringing and RMF running proved to be quite effective at cleaning the system.

The emission array consisted of a fan of 9 channels looking at emission in a relatively line free region in the visible spectrum between 500 and 600 Å. The channels looked along different chords located near the midplane of the plasma. Though the emission seemed to correlate with the plasma density, very little effort was put into effectively using this diagnostic. This partly had to do with the plasma having a large radius with a hollow core, a profile which is not conducive to an inversion that yields useful radial information.

One of the two doppler broadening diagnostics consisted of an ICCD spectrometer operated by Dr. Samuel Cohen of Princeton Plasma Physics Laboratory. In addition to providing broad spectrum of all the lines present in STX, the spectrometer could accurately record time averaged line profiles from which the ion temperature could be deduced. As expected, the ion temperature turned out to be no more than the couple eV expected from the molecular dissociation of deuterium. Unfortunately, the spectrometer was only operated on STX during its initial stages of operation, long before the plasmas of interest discussed here were made. The other doppler broadening diagnostic consisted of a 16 channel photomultiplier tube used to look at the profile and time dependence of various lines. Though only operated briefly on STX, it saw no significant evidence of any

significant ion temperature or rotation. STX stopped operating before it was realized that it would be very interesting to look end on for axial flows, though this is something which will hopefully happen in the future on either STX or TCS.

# CHAPTER 5
# STX DATA

The presentation and discussion of STX data has been divided up into the following basic parts. It begins with a presentation of the basic STX operating point in order to give some familiarity with the plasmas being studied as well as the diagnostics used to probe them. Then, in the next chapter, the data is discussed in the context of the new understanding of the RMF current drive process, with particular attention being paid to the importance of axial and radial flow as well as to the importance of current being driven in a manner consistent with the FRC's equilibrium profile. These two issues then lead naturally into a discussion of STX's inability to drive a steady state FRC equilibrium.

## Basic STX Data

It would be nice to present STX data as scans through parameter space covering such things as density, confining field, and RMF amplitude, to name a few. Such scans could be used to both determine and verify scaling laws, as well as point the way towards improved operation. Unfortunately, due to a lack of available RMF power, STX has been forced to operate at essentially only a single point in parameter space. The RMF amplitude is set to the maximum allowed by the IGBT supply while the density is set to the minimum for which pre-ionization is still possible. Since the RMF frequency is fixed by the tank circuit, the axial field strength is determined as well, and it unfortunately pushes the lower limits of operation of the axial field banks. The consequences are that the axial field is not readily adjustable, and that changes in amplitude result in changes in waveform, which in turn substantially alter the plasma behavior. In light of this, STX data will be presented as though the machine were only operated at one characteristic set of parameters, a set designated as STX's basic operating point. Some very limited scans through parameter space have been performed, and the resulting data will only be presented to the extent that it helps explain STX's behavior and the underlying physics.

Experimentally, the first trace looked at is the excluded flux signal, figure 5.1. Though it is a weak predictor of the presence of field reversal, since the RMF is so effective at driving current even if reversal is not obtained, it does provide immediate information about the effectiveness of the current drive. The larger the amplitude and the greater the persistence in time, the better the shot. With a few exceptions, all optimization of STX was done through comparison of the excluded flux signals. Unlike the internal probe signals which required substantial processing and computational time, the excluded flux signals were immediately available for display upon completion of the basic data acquisition. The decay in the signal from 0 to 100 μsec is the decay of the conventionally formed FRC used to help ionize and heat the initial target plasma. The RMF was only turned on at 100 μsec.

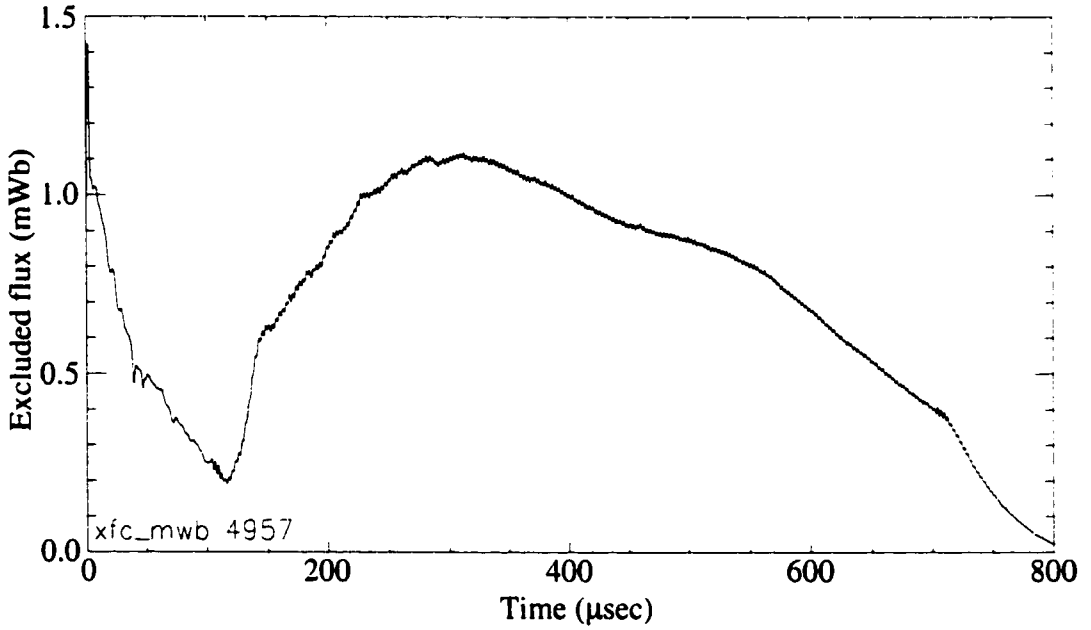


Figure 5.1 Typical excluded flux signal.

Figure 5.2 shows the coil flux $\phi$ normalized to the coil radius, and the edge magnetic field $B_e$. These are both far from the ideal flat traces one would have liked, though considering that the banks and magnets were only designed to produce relatively flat

fields for approximately 100 μsec, the traces are far better than they initially were. Notice how flux is driven from the magnets as the FRC's poloidal flux grows, and then how the coil flux starts to slowly increase at ~ 300 μsec as the FRC decays away. The axial field magnets are certainly not flux conserving, though they are flux shaping, in that axially the coil flux is held constant until the very end of the coil set. The issue of the coil flux increasing in time will be discussed subsequently, since it is believed to be in part responsible for the gradual loss of RMF drive and field reversal. Both the analytic[8] and numeric[18] RMF simulations assume the presence of true flux conserving coils.

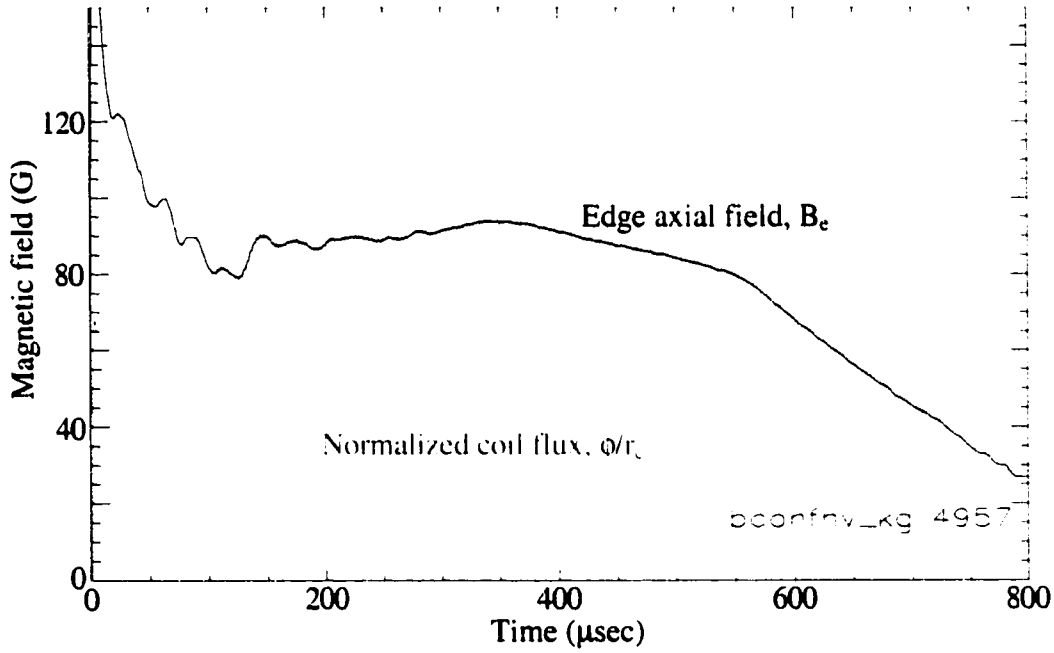


Figure 5.2 Typical coil flux and edge magnetic field.

Several thousand shots were taken to optimize the axial fields, all of which had to be done with plasma present. The plasma is a sufficient perturbation to the axial field that it is meaningless to optimize the fields in vacuum. Additionally, each different set of operating conditions required its own field optimization, something which made it very difficult to change plasma conditions and then compare the resulting behavior. Different plasmas give rise to different axial fields and fluxes which in turn profoundly impacted

the plasma's behavior and mask subtle differences arising from other sources. Figure 5.3 shows the internal axial fields at various radii. Once again, one can see the decay of the initial conventionally formed FRC during the first 100 μsec. Notice the strong oscillations within this FRC, oscillations which fortunately become much less, and then disappear in the RMF driven FRC.

Figure 5.4 shows the FRC's poloidal flux determined from the internal $B_z(r)$ measurement. Except for very brief periods, the poloidal flux was always increasing or decreasing, at rates typified by those shown in this figure. Most often, and under a wide variety of conditions, a rapid flux buildup is followed by a gradual decay. There is a brief quasi steady state period from 300 to 400 μsec.

Figure 5.5 shows the theta component of the RMF at various radii within the plasma. The initial ratcheting in and out of the plasma for a few hundred microseconds is typical before the penetration depth settles down into a more quiescent state. Except for a few very rare instances of brief duration, the RMF never penetrated substantially more than shown here. Traces at radii smaller then 12 cm are not shown since they are all flat with no RMF penetration, and only show the typical noise pickup. These signals are more succinctly shown in figure 5.6 which only plots the envelope signal of the RMF amplitude. The black trace in this figure shows the RMF field that would be produced in vacuum with the plasma antenna currents. The difference in magnitude between this trace and the edge trace with plasma present is due to screening currents flowing in the plasma and amplifying the RMF by about a factor of two at the plasma edge.

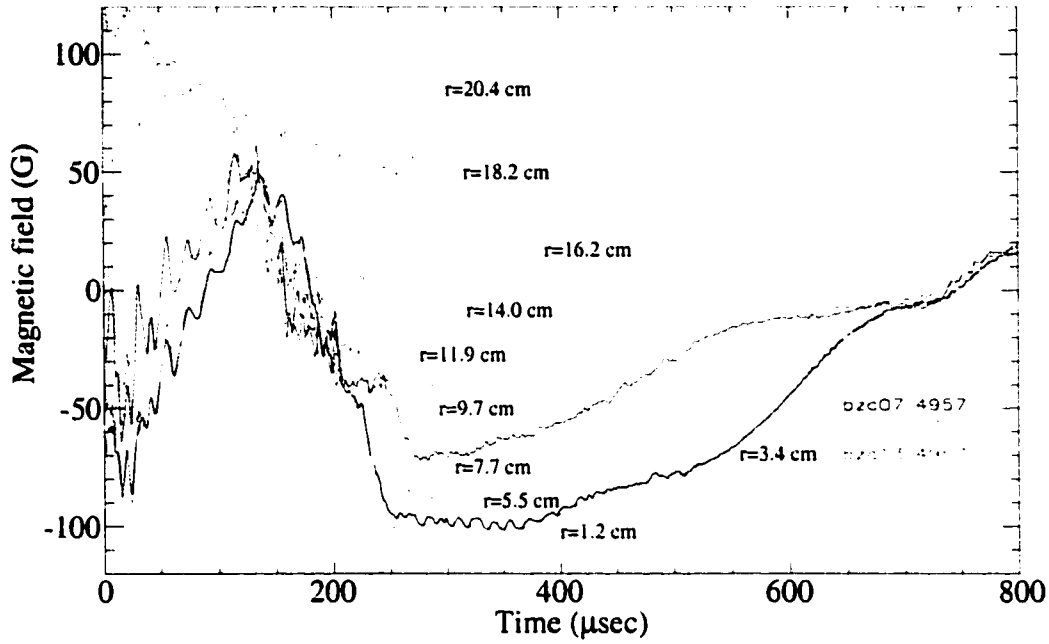


Figure 5.3 Typical internal axial fields

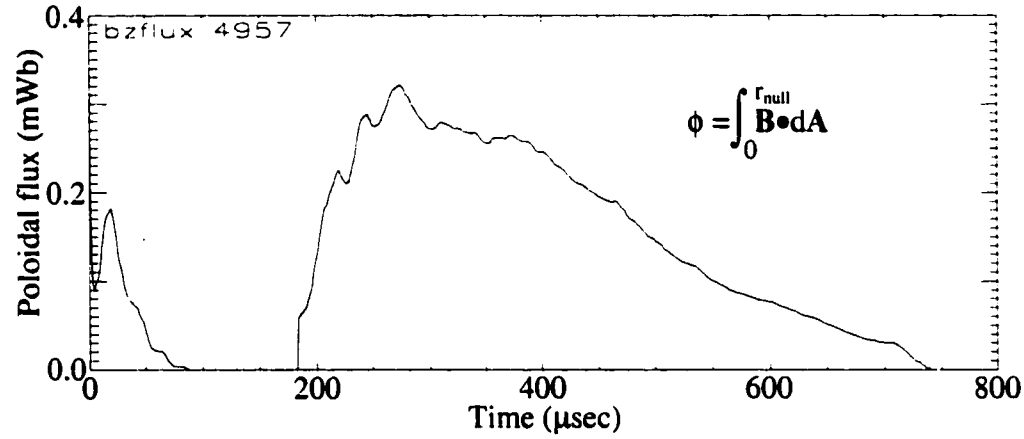


Figure 5.4 Typical FRC poloidal flux

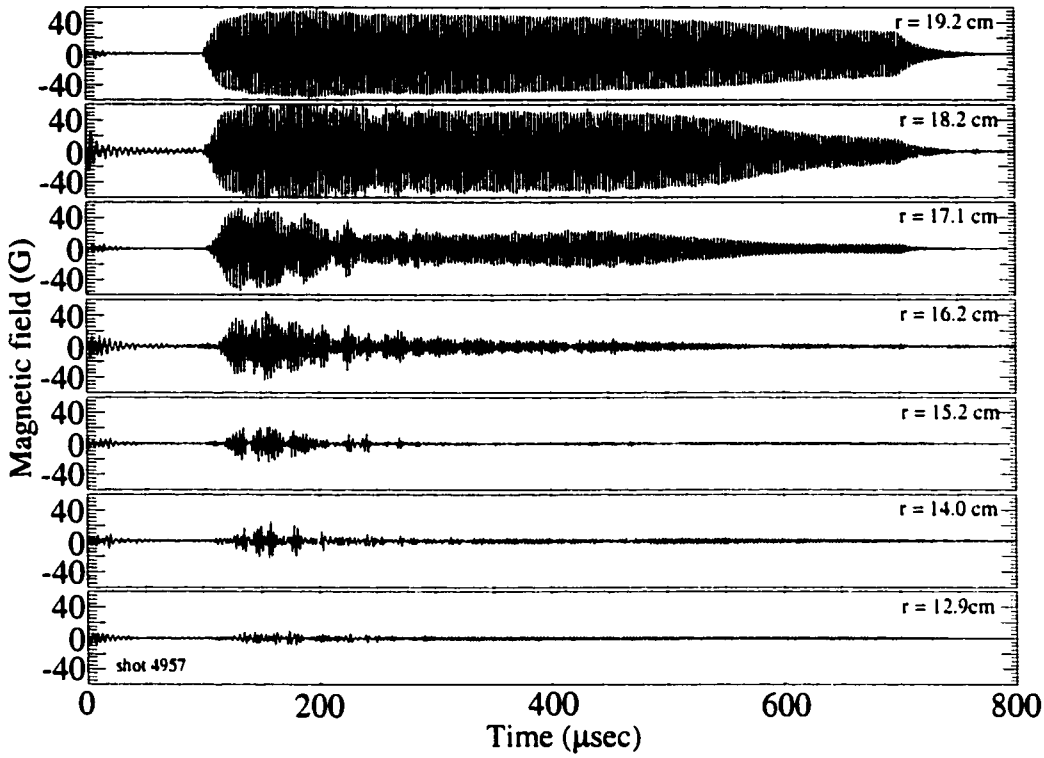


Figure 5.5 RMF $B_\theta$ penetration vs. time at different radii
(Vacuum $B_\theta$ is ~25 G and is shown in figure 5.6, black trace)

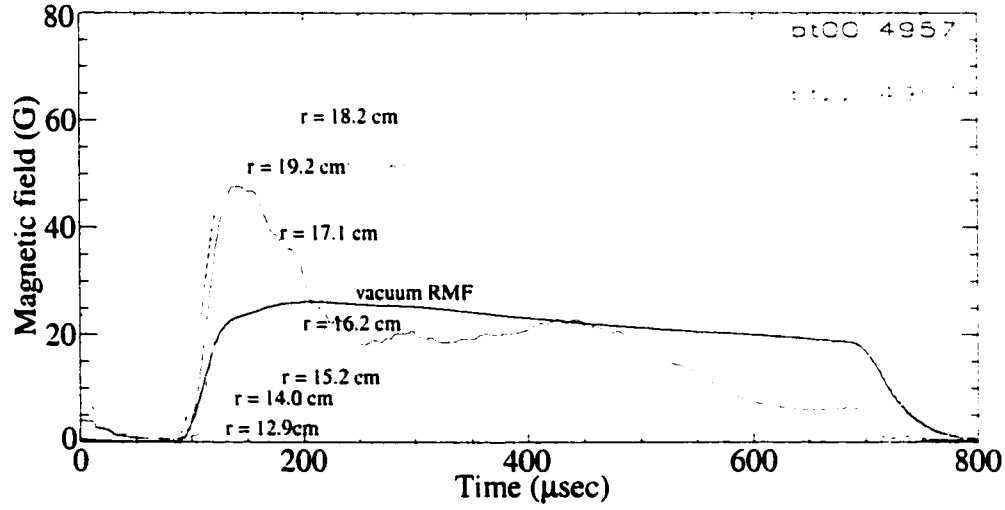


Figure 5.6 RMF $B_\theta$ envelope signals at different radii
(Relevant plasma radii shown in figure 5.7)

Figure 5.7 shows the excluded flux radius, $r_{xf}$, the separatrix radius, $r_s$, the null radius, $r_n$, and the separatrix radius divided by the square root of 2, $r_{srt}$. In conventional FRCs where p is a function of $\psi$, the square root of two times less then the separatrix radius should be the null radius, something which is not the case with these RMF driven plasmas. However, notice how $r_n$ and $r_{srt}$ overlay in the conventionally formed FRC, as would be expected. Another deviation from the land of conventional FRCs is apparent if one compares $r_s$ to the poloidal flux shown in figure 5.4. As the poloidal flux gradually decays to zero, $r_s$ remains fairly constant due to the plasma transitioning slowly to a high a beta $\theta$-pinch type plasma, an issue which will be discussed subsequently.

It remains a mystery as to why the excluded flux radius is less than the separatrix radius. This phenomena is persistent shot to shot over a wide variety of conditions. Much effort has been put into examining the details of the excluded flux array in an attempt to track down what appears to be some sort of error, but to no avail. One would expect the excluded flux radius to always lie outside of the separatrix radius, with them becoming concurrent only as the separatrix density fell to zero. Notice how the separatrix radius exceeds the wall radius of 20.4 cm. Wall contact typically only occurs when the separatrix radius exceeds the wall radius by a few centimeters, a testament of the low to non existent separatrix density. The very rapid rise and fall of the separatrix radius is characteristic behavior. It occurs because the RMF generally removes all forward field inside its penetration depth before it actually starts to reverse any field. Then, the first reversed field occurs at the RMF penetration depth, something which immediately places the separatrix radius quite far out since the RMF never penetrates very far in. Many attempts were made, all unsuccessfully, to create plasmas with smaller separatrix radii. This is an issue which is tied to the observation that the RMF only directly drives current near the wall, and it will be discussed subsequently. The jumping around of $r_n$ is due to a difficulty in locating the $B_z$ field zero crossing given the very flat field profile at the null, and as shown here it has little to do with actual plasma dynamics.

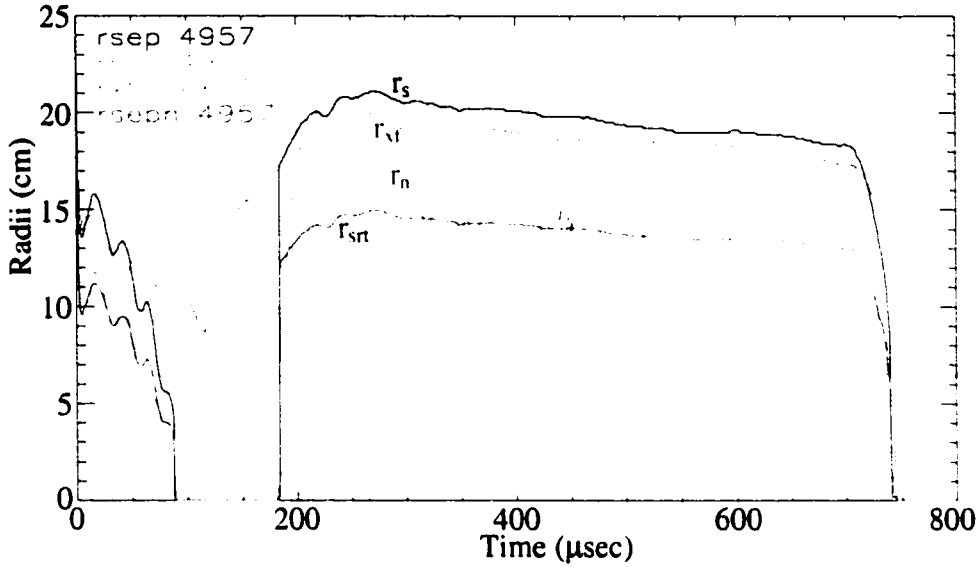


Figure 5.7 Typical excluded flux, separatrix, and null radii

Figure 5.8 shows the electron temperature and peak density. Both of these quantities are derived with use of the internal $B_z(r)$ measurements, and their derivation is discussed in great detail subsequently. From Doppler broadening measurements, the ions are believed to be cold, having at most a few eV of energy. Notice the initial dynamic behavior during flux buildup, and the settling down into a more quiescent state. The black trace is from a typical shot while the red trace is the average of several typical shots stored as a fictitious shot 5000. It is useful in calculating data in other identical shots where the internal probe was in a location that prevented a direct temperature inference for those shots, such as the series of shots where the axial scan was done with the internal probe.

Figure 5.9 shows the total plasma energy per meter of length, $E_{totpm}$, and the particle inventory per meter of length, $N_{totpm}$. These are calculated using parameters measured at the z = 0 machine midplane; though axially, there is little variation until one approaches the end of the RMF antenna. During initial flux buildup, field reversal extends 10 to 15 cm past the RMF antenna, but rapidly shrinks to the length of the RMF antenna as soon as flux buildup stops. Then, during the gradual flux decay phase, the plasma grows in

length back out to 15 cm past the end of the RMF antenna. It is prevented from extending farther due to the presence of a strong mirror field. These traces indicate a fairly constant particle and energy inventory for the duration of the plasma.

Figure 5.10 shows the plasma average beta, $\langle\beta\rangle = \int p2\pi rdr/(B_e^2/2\mu_o)$ integrated from 0 to $r_s$, the average $\beta$ for everything inside the quartz vacuum wall at 20.4 cm, $\langle\beta_{wall}\rangle = \int p2\pi rdr/(B_e^2/2\mu_o)$ integrated from 0 to 20.4 cm, and the average beta based on the traditional FRC average beta condition, $\langle\beta_{xs}\rangle = 1 - 0.5x_s^2$, where $x_s = r_s/r_c$. The plasma pressure p is directly determined from the $B_z(r)$ measurement through radial pressure balance. These plasmas have an unusually high $\langle\beta\rangle$ which is certainly not consistent with the traditional FRC equilibrium $\langle\beta_{xs}\rangle$. In a conventional FRC as the poloidal flux disappeared, $B_e$ would fall, as would n and T, and the plasma would grow axially. In these RMF driven plasmas, plasma pressure simple replaces the disappearing poloidal flux, with no substantial changes in n or T.

Figure 5.11 shows the ratio of the separatrix plasma pressure to the peak plasma pressure, $p_{nsep}$, and the ratio of the axis of symmetry plasma pressure to the peak plasma pressure, $p_{naxis}$. Since the temperature is assumed to be uniform, these are the same as the ratio of separatrix or axis of symmetry density to the peak density. Notice how high and similar these curves are for the initial conventionally formed FRC, as expected. In the RMF driven FRC, the wide separation of these two traces is another clear indication that p is not a function of $\psi$. These traces are from the same flux surface. The RMF is believed to be actively driving particles in off the outer field lines, a point which will be discussed in much more detail subsequently. Figure 5.12 shows the time evolution of the pressure profile normalized to the peak pressure. These are radial profiles taken at z = 0. They clearly show inventory replacing poloidal flux.

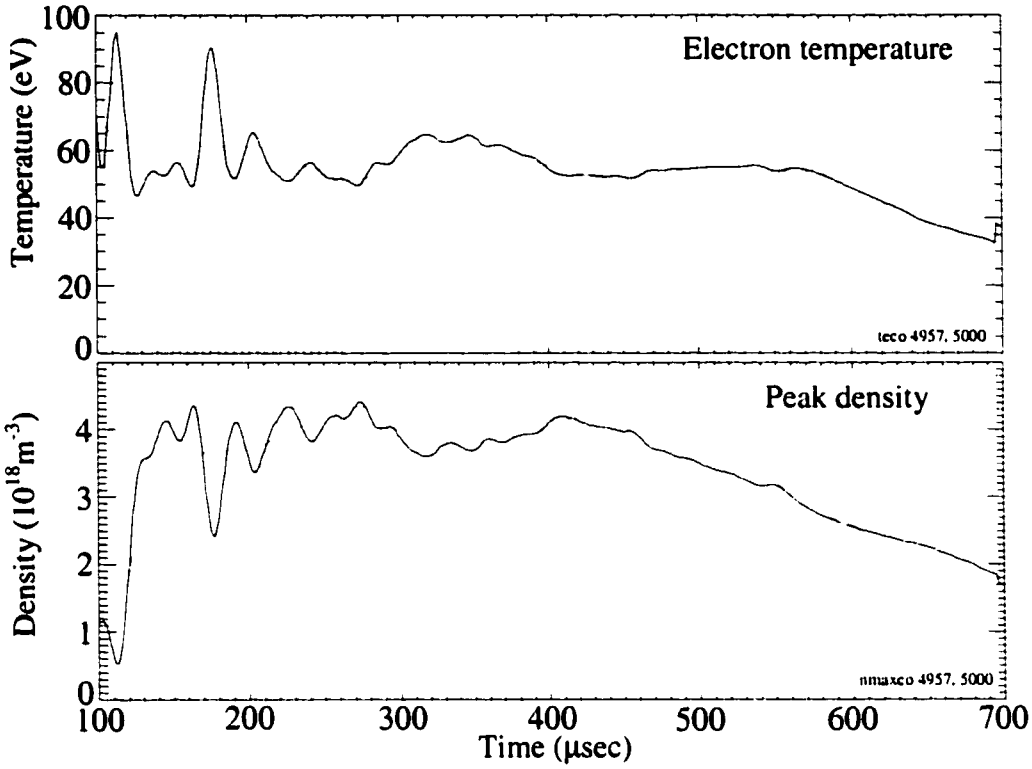


Figure 5.8 Typical electron temperature and peak density

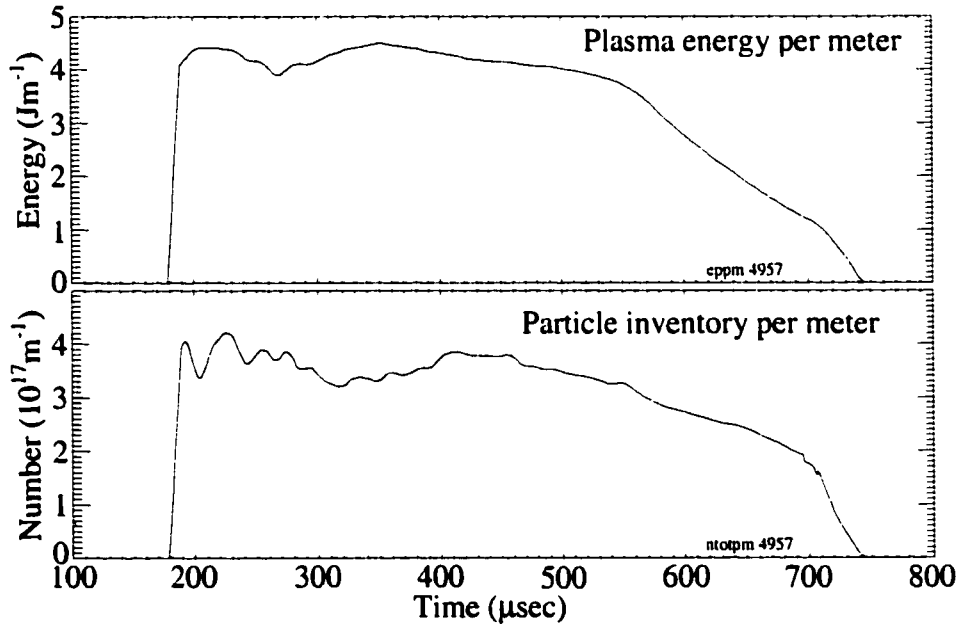


Figure 5.9 Plasma energy and inventory per meter length

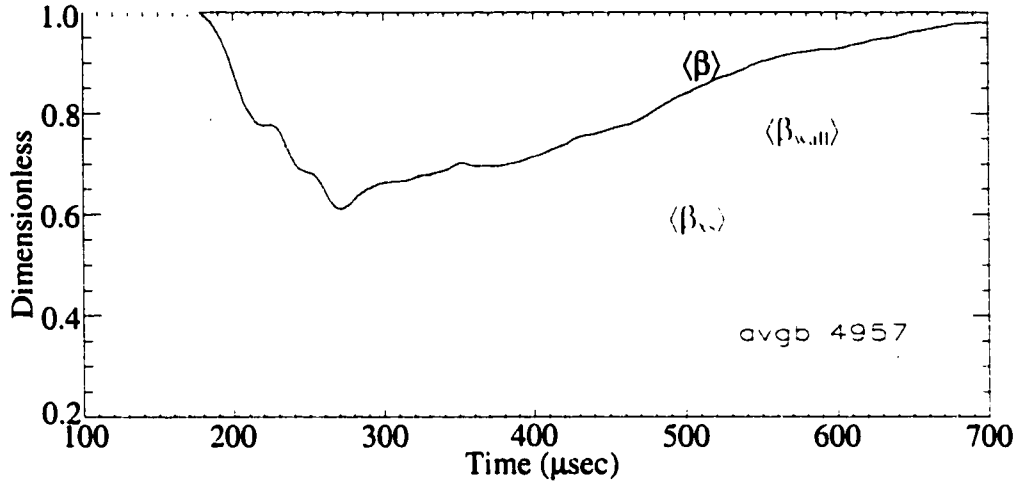


Figure 5.10 Plasma average betas

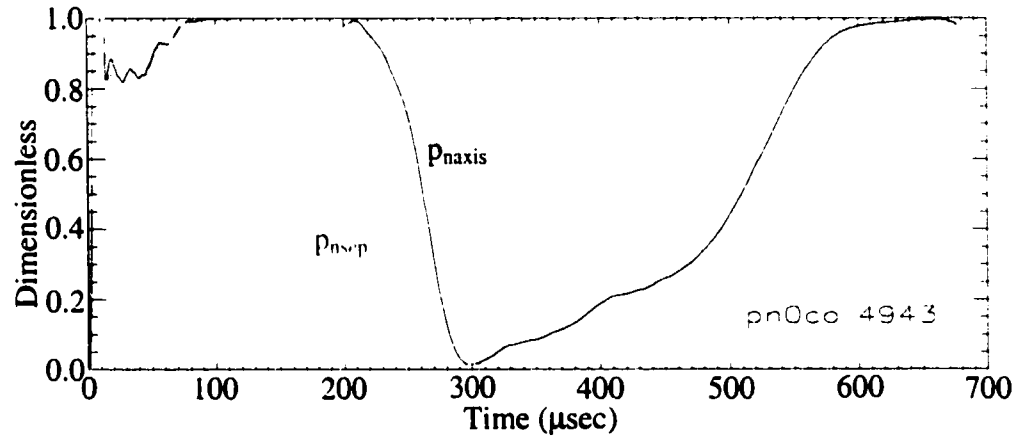


Figure 5.11 Separatrix and axis of symmetry normalized pressure

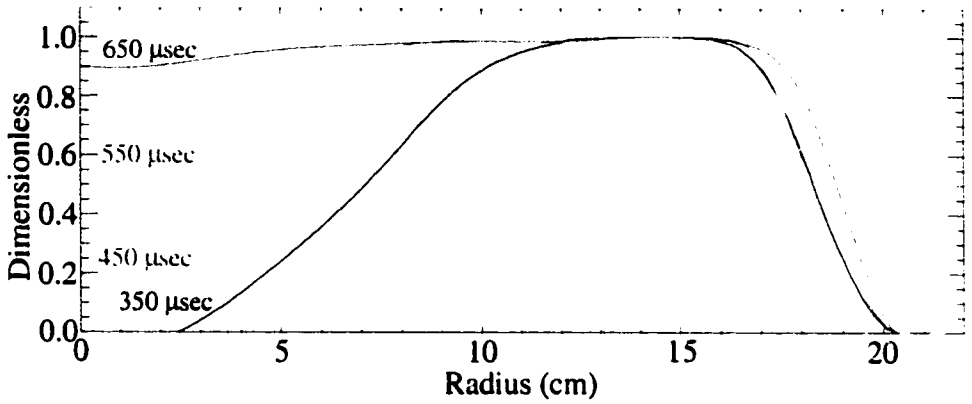


Figure 5.12 Time evolution of the relative pressure profile.

Figure 5.13 shows the typical $B_z$, $B_\theta$, and $B_r$ radial profiles, as well as the radial density profile. $B_\theta$ and $B_r$ are the peak values of the oscillatory RMF field components. The RMF penetrating to the approximate null radius is very typical, and its penetration depth does not change substantially for the duration of the shot, except very early on during the rapid flux buildup. Figure 5.14 shows the radius at which the theta component of the RMF amplitude falls to 40 % of its peak value compared to the location of the null radius. The use of 40 % as opposed to some other percentage is quite arbitrary in showing the RMF penetration depth. What is important is the relative separation between the RMF penetration depth and the null radius. As expected from the theory, this distance is small to negative during flux buildup, but grows larger during decay as the RMF and null move away from each other. Figure 5.15 shows the $B_z$, $B_\theta$, $B_r$ and n plots for a series of times during the plasma's life. As flux is lost, notice the evolution into a high beta plasma column. It is believed that the strong mirror field at the ends aids in confining the plasma in this state, since the field lines are certainly open but the state is persistent. Figure 5.16 shows the coil flux normalized to the coil area for this mirror field.

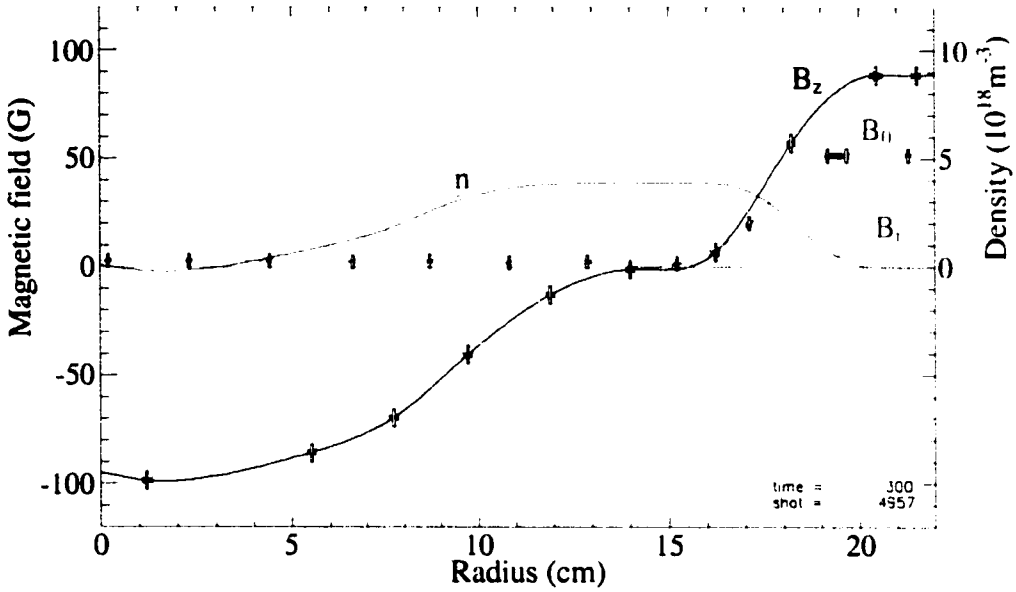


Figure 5.13 Typical $B_z$, $B_\theta$, $B_r$ and n radial profiles at t = 300 μsec

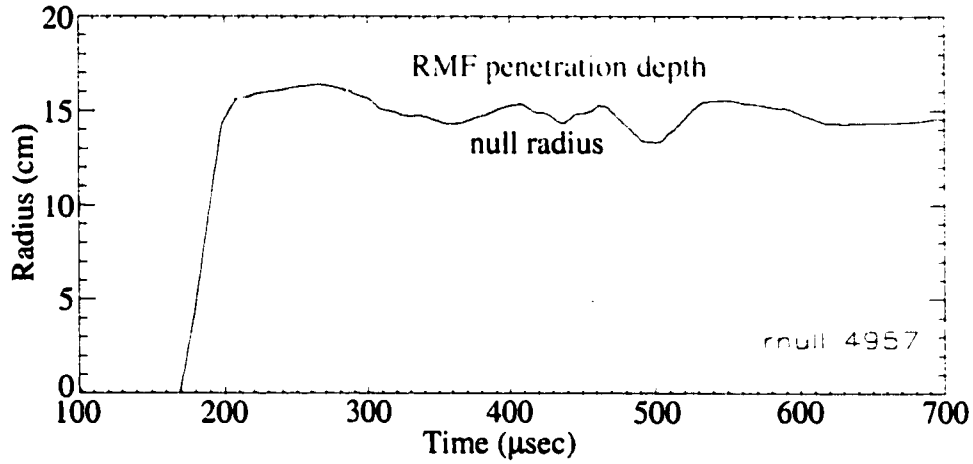


Figure 5.14 Radius at which RMF amplitude falls to 40 % of it maximum

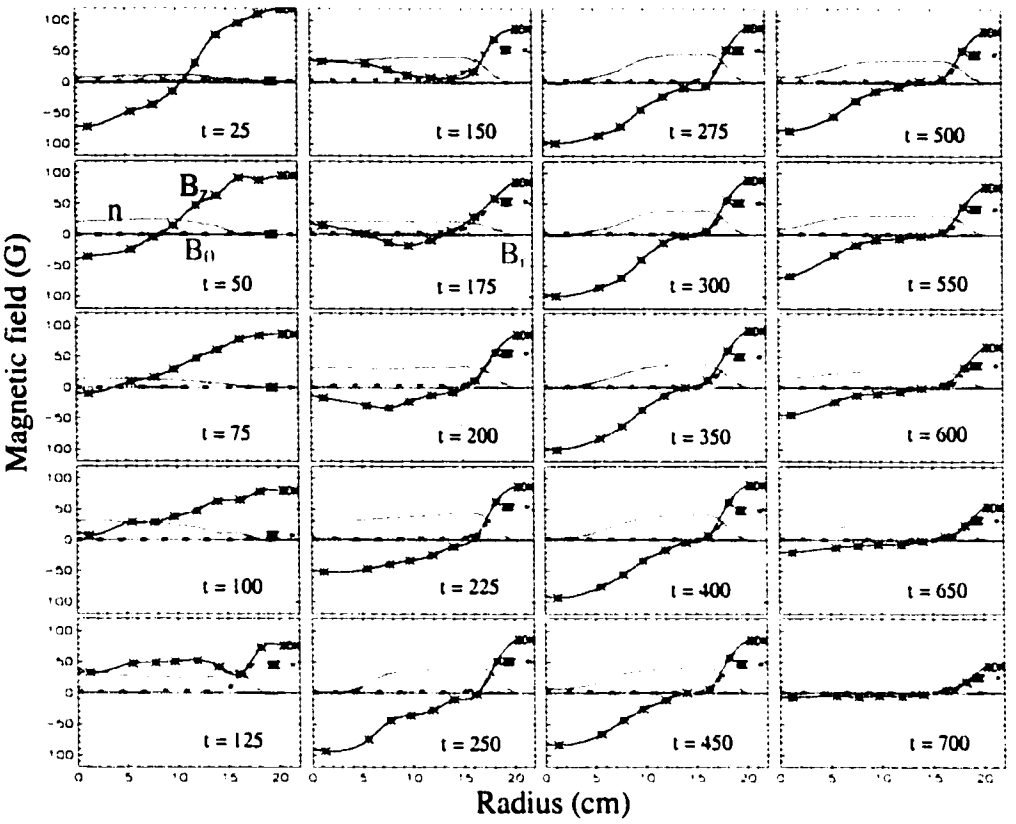


Figure 5.15 A time history of radial profiles

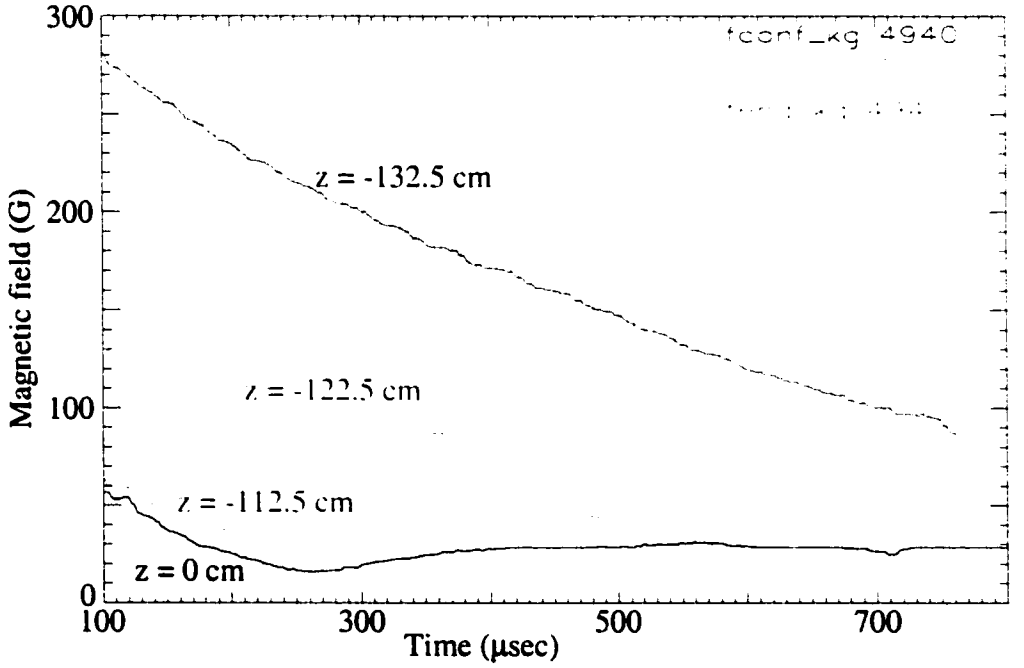


Figure 5.16 Axial profile of the STX mirror field coil flux normalized to $r_c$

## A Comparison to Experiment and Simulation

Even though the STX plasmas were substantially different from the Flinder's rotomak plasmas[13,15,3,2], there are some striking similarities in the radial profiles, as shown in figure 5.17. Both the 10 L and the 50 L rotomak machines drove plasmas that exhibit the same flattening of the axial field profile across the null, and a similar RMF penetration depth to approximately the null radius. Such a field flattening and partial RMF penetration are also seen in Milroy's[18] numeric simulations, as shown in figure 5.18. Another prediction from the numeric simulation shows up quite strikingly in the STX data, that of RMF slippage and field twisting. Figure 5.19 shows a numerically simulated cross section of what the RMF field lines should look like in a partially penetrated plasma. At some location where the RMF field becomes weak enough that it can no longer provide the torque necessary to fully drive the plasma, it begins to slip and then twist up. Figure 5.20 shows the RMF amplitude as a function of time at various radii from both the simulation and the STX experiment. Notice how the RMF phase slips in time as one moves radially into the plasma, until the RMF is fully screened. A particularly nice agreement is obtained between the amount of phase slippage and the drop in amplitude at 175 μsec. The beginning of the experimental trace shows one of the rare times when the RMF actually started fully penetrated. The reason for it in this shot is that the initial ionization was very weak which allowed the RMF to penetrate. However, as the plasma density grew, the RMF started to slip, and then was rapidly driven out to the null radius. The second third of the experimental traces show the RMF beginning to repenetrate a little, and then getting kicked back out, something also seen in the beginning two thirds of the numeric simulation traces. Such slippage was initially a prediction of the simulation, and then when looked for, was found to be occurring in STX. Also notice, that as the RMF is screened, its amplitude just outside the screened region builds. At 140 μsec, the RMF was already starting to be screened from near the axis of symmetry.

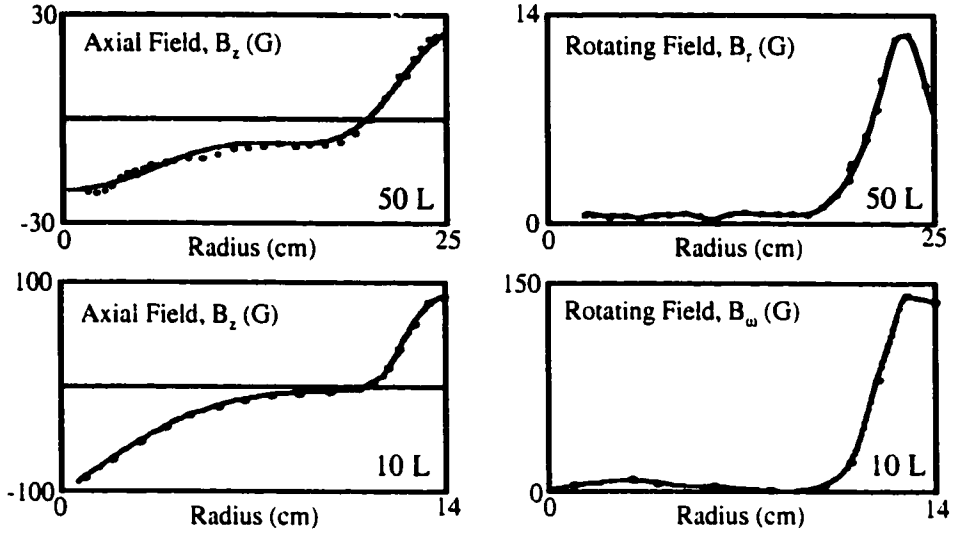


Figure 5.17 Flinder's 10 L and 50 L rotomak radial magnetic profiles

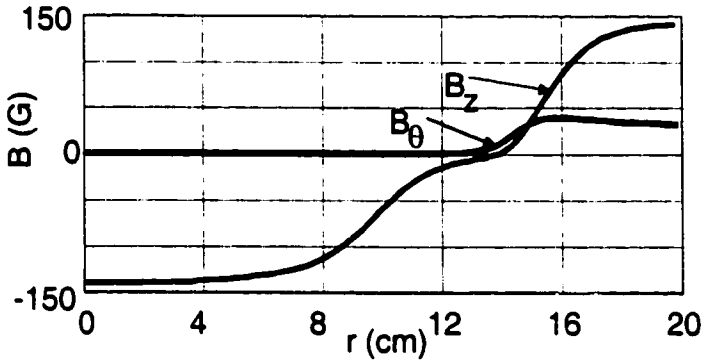


Figure 5.18 Radial field profiles from Milroy's numeric simulation.

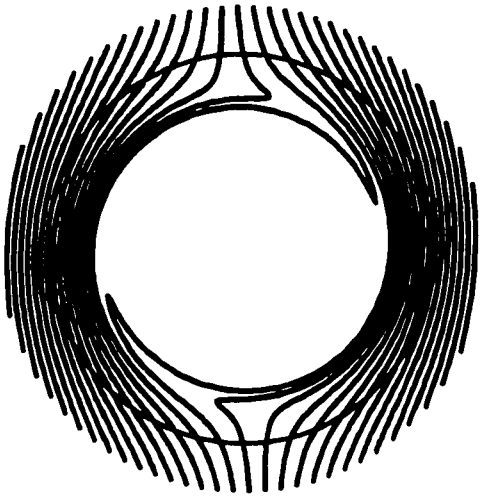

Figure 5.19 Numerically generated cross section of the RMF

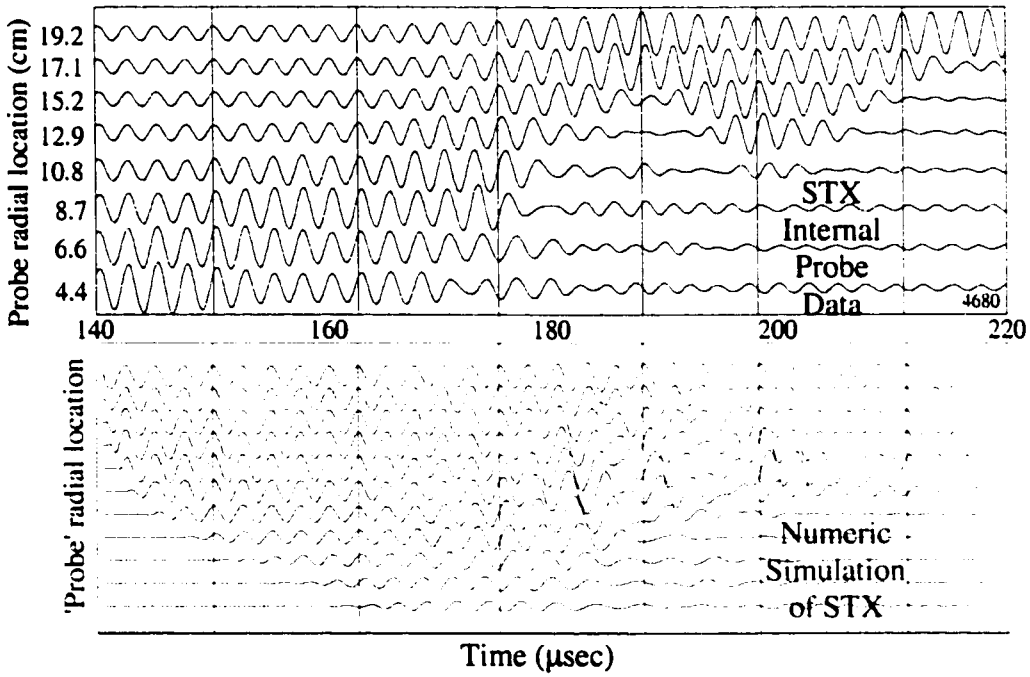


Figure 5.20 Phase slippage of RMF $B_\theta$ in STX and numeric simulation

**Justification of the Internal Probe Data Analysis**

Virtually all of the above signals were derived from one diagnostic, the internal magnetic probe. Given the unique FRC magnetic geometry coupled with the assumption of cosynchronous electron rotation within some narrow region and a spatially uniform electron temperature, from the measurements of $B_z(r)$ and $B_\theta(r)$, a large number of other plasma parameters are calculable. These include such things as density, electron temperature, ion rotation, and azimuthal electric field, to name a few. This is fortunate given STX's otherwise very limited diagnostics. Before proceeding though, it is important to both explain and justify the validity of the techniques used to derive various parameters, as well as discuss the assumptions being made. This is particularly important since the vast majority of data about STX originates from the internal probe, and if it is not on a sound footing, then little else is.

The analysis begins with the assumption of cosynchronous electron rotation within the penetration depth of the RMF. Given the physics of an oscillating field penetrating a conductive medium, without the electrons in near cosynchronous rotation, the RMF could never penetrate more than the classical skin depth, in this case a few millimeters at most. The very fact that the RMF penetrates several centimeters or more can only be explained by near cosynchronous electron rotation. This is a point substantiated by Milroy's resistive MHD numeric simulation. Making this assumption allows one, in the region of RMF penetration, to relate the density to the gradient in the axial magnetic field through the relation $n = n_{cosync} = (1/e\omega r\mu_o)(dB_z/dr)$, where $dB_z/dr$ is directly calculated from the measurement of $B_z(r)$. This calculation is typically made at a radius where the RMF has fallen to approximately half its peak value. Combining this measurement of the local density with the measurement of $B_z$ allows one to calculate the local temperature T through the radial pressure balance equation, $p(r) + B_z(r)^2/2\mu_o = B_e^2/2\mu_o$, with $p = nkT$. At this point, the knowledge that the ions are cold from the Doppler broadening

measurements is important since it immediately lets one equate T with $T_e$, something that will be presumed from here on.

Next, if one assumes that $T_e$ is spatially uniform, one can use the radial pressure balance equation to calculate n at all radii where $B_z$ is measured, from the quartz wall to 5.2 cm past the axis of symmetry. The assumption of uniform $T_e$ is certainly plausible given the FRC's magnetic geometry with interior field lines looping around to the outside, as well as the FRC's high $\langle\beta\rangle$ and thin gradient to the separatrix. Historically this assumption has often been made. Several additional aspects of the data also support this claim, the most convincing of which will be presented last. First, if one makes this assumption and calculates the density profile, $n_{press}(r)$ based on radial pressure balance alone, and then compares this profile to that obtained by calculating the density profile, $n_{cosync}(r)$, in the region of RMF penetration based solely on the assumption of cosynchronous rotation, one obtains a near perfect agreement. This would certainly not be the case if $T_e$ had a strong radial dependence. Figure 5.21 shows these two curves, blue and green, and their good agreement in the region of RMF penetration from 15 to 20 cm. Outside of this region they deviate wildly since the electrons are most definitely not in cosynchronous rotation.

The second supporting piece of evidence comes from considering what the axial field profile would be if all the electrons in the calculated density profile $n_{press}(r)$ were rotating cosynchronously. Figure 5.21 also shows these two curves in cyan, with one starting at the value of $B_z$ at the axis of symmetry and integrated out, and the other starting with the value of $B_e$ at the wall and integrated in. Notice how these curves have excellent agreement with the measured axial field both near the axis of symmetry as well near the wall in the region of RMF penetration. This supports the claim of constant $T_e$ if one considers that the inner and outer regions span the same flux surfaces, and that in Milroy's numeric simulation, if cosynchronous rotation occurred on a flux surface outside the null radius, it also occurred on the same surface inside the null radius. Essentially, the

flux surfaces rotate as a rigid body. If $T_e$ inside the null radius deviated sufficiently from Te outside the null radius, there would not be such good agreement between these cosynchronous curves and the measured profile. Since there is even more convincing evidence presented subsequently that $T_e$ is uniform, this agreement between the curves can rather be viewed as an indication towards the validity of the numeric simulation. Notice the wide gap between these two cosynchronous curves. It indicates that there are far more particles present than needed to produce the measured field reversal. An initial thought as to why the RMF was failing to sustain the FRCs was that there were an insufficient number of charge carriers to allow the field to be reversed. However, even if there are plenty of particles present, they may not be accessible to the RMF, a point which will be taken up subsequently.

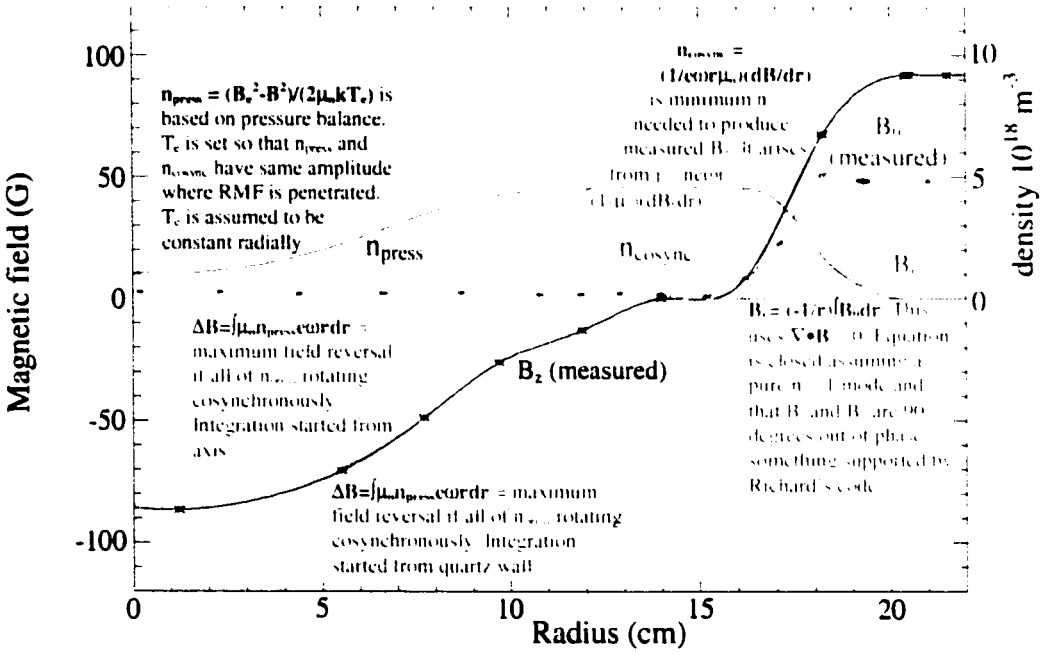


Figure 5.21 Analyzing the internal probe data

On a few shots, there were only just enough electrons to produce the measured field reversal. For these shots, the two cosynchronous curves overlayed, and there was not such a flattening of the axial field profile across the null. Figure 5.22 shows the traces for

such a shot. Interestingly, it was these shots that exhibited a slow flux buildup for the entire duration of the RMF, as shown in figure 5.23. Figure 5.24 shows the time histories of $B_z$ at various radii, figure 5.25 shows $B_z(r)$ profiles at various times, figure 5.26 shows the edge field and coil flux, figure 5.27 shows the plasma radii, figure 5.28 shows the density, inventory, energy, and temperature, figure 5.29 shows the separatrix and axis of symmetry relative pressures, and figure 5.30 shows the plasma $\langle\beta\rangle$. Unless otherwise labeled, traces in red are from the standard shot and are shown as a point of comparison. It is interesting that the RMF started to rapidly drive current at ~ 150 μsec, but that it stopped and was then followed by a very gradual buildup. There was no initial conventionally formed FRC, and the RMF started driving current when it was fully penetrated. These shots were rare and difficult to reproduce, and in all of the data acquired, there are only a few of them, too few to obtain all the data needed for a careful analysis. To the best of our knowledge, the primary difference between these shots and the standard shots was that the pre ionization was deliberately stifled. The RMF appeared so effective at initially driving current and reversing the field, that it often seemed to overshoot what would be its natural equilibrium. The hope was that by restricting the inventory available to the RMF, it would reverse the field more gradually, and enter its equilibrium state in a more sustainable manner. Steady flux growth did occur for the entire time the RMF was on. The lack of reproducibility likely arouse from a strong sensitivity to the initial state of preionization, something we had insufficient control over.

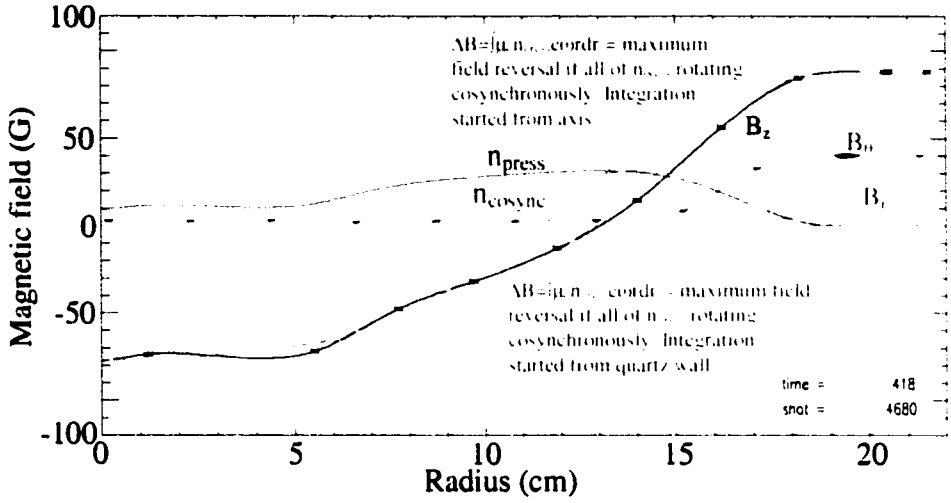


Figure 5.22 Radial profiles, see figure 5.21 for detailed trace labels.

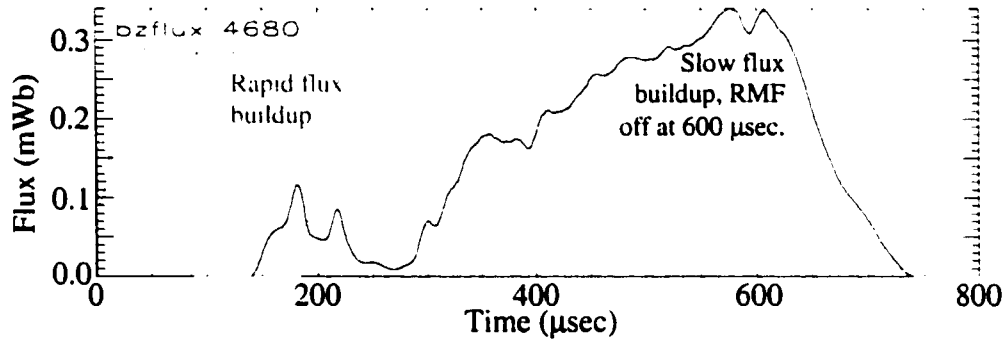


Figure 5.23 Poloidal flux for slow and fast growth shots.

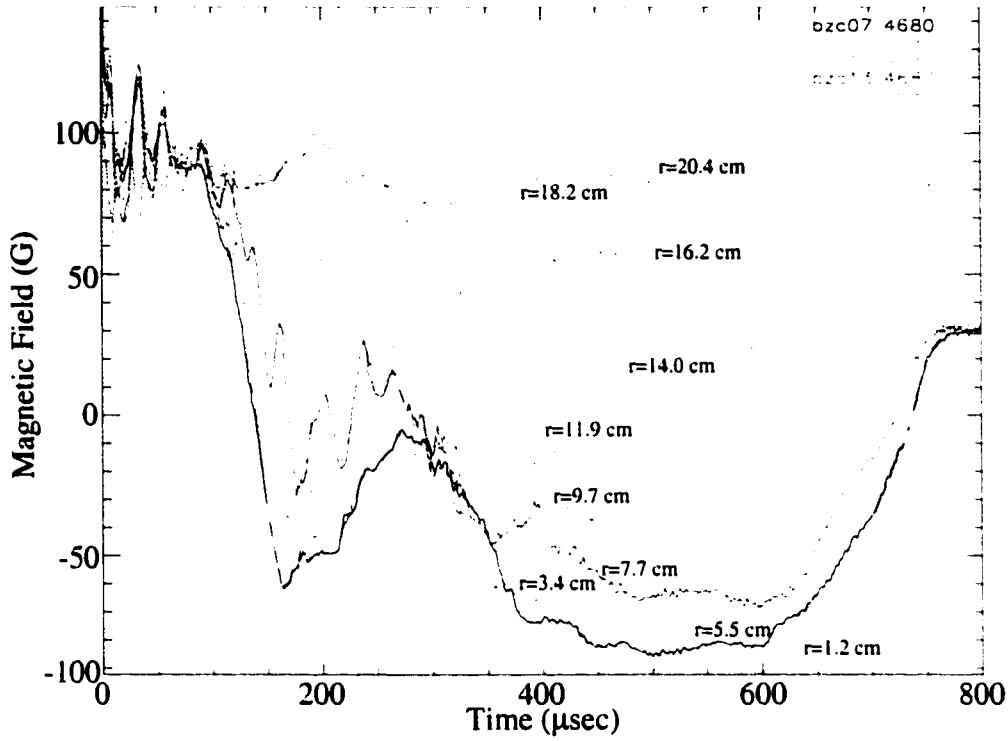


Figure 5.24 Axial field at various radii, RMF off at 600 μsec.

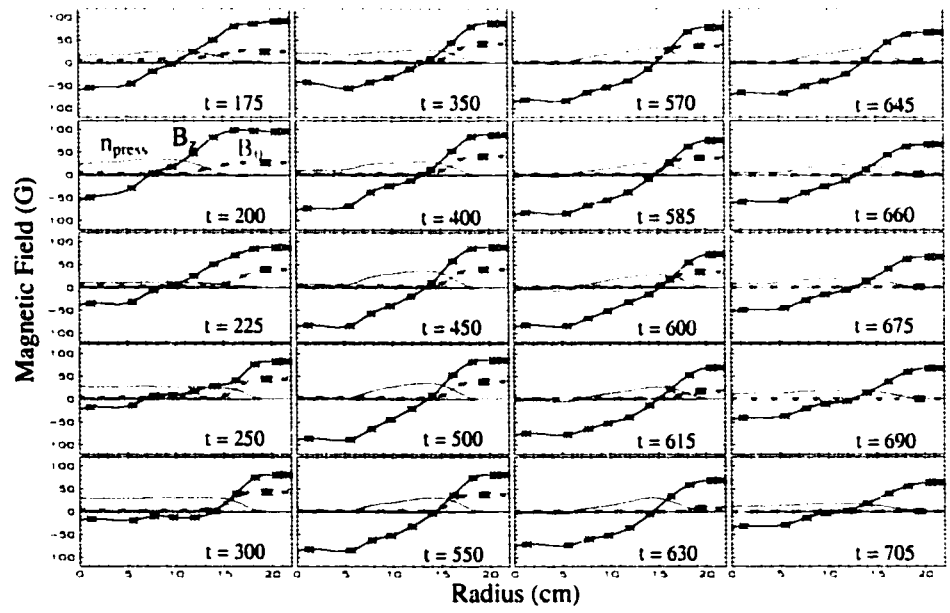


Figure 5.25 Evolution of radial profiles

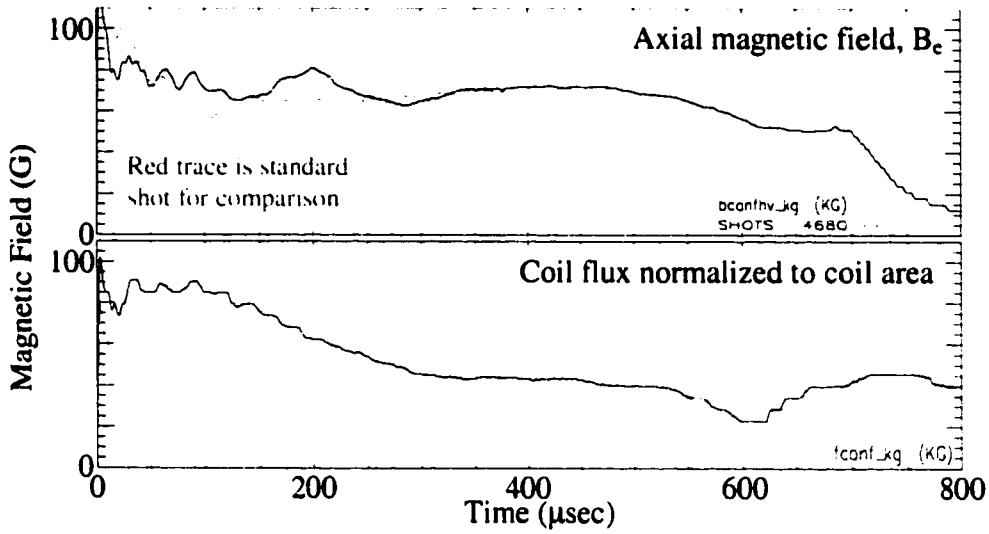


Figure 5.26 Coil flux and field

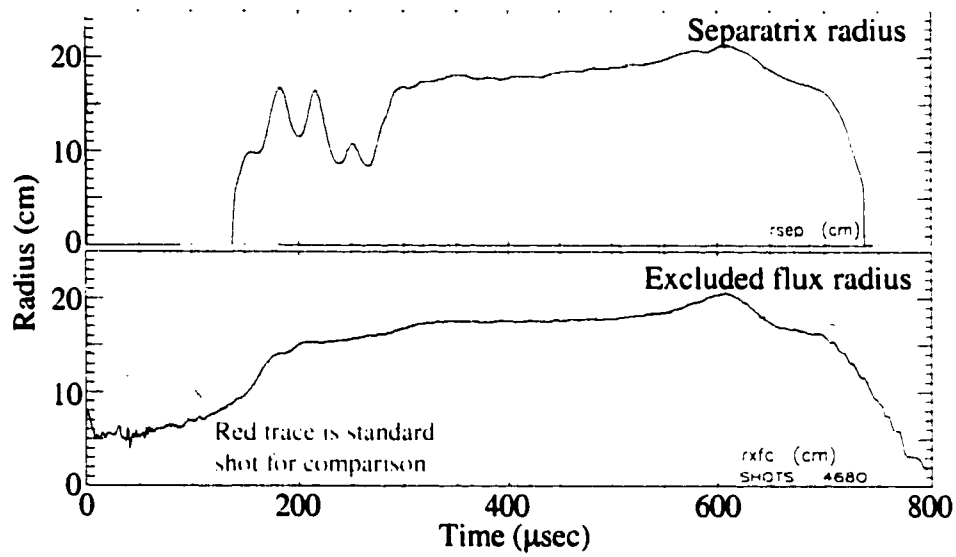


Figure 5.27 Plasma radii

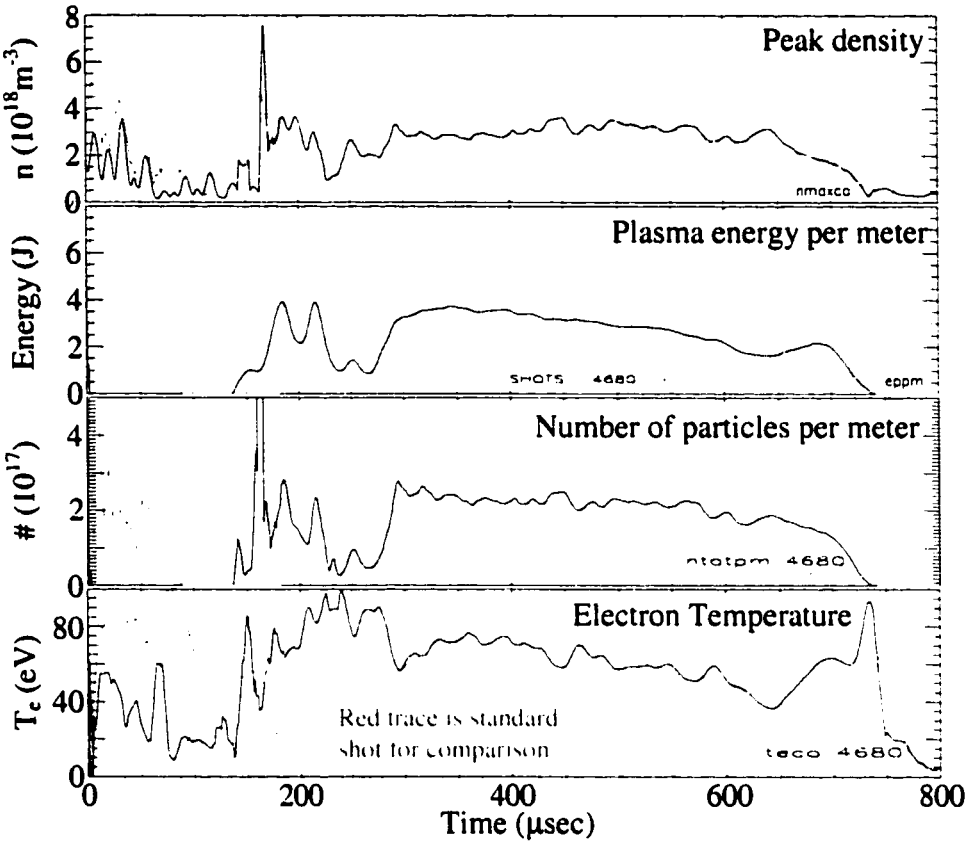


Figure 5.28 Plasma density, inventory, energy and temperature

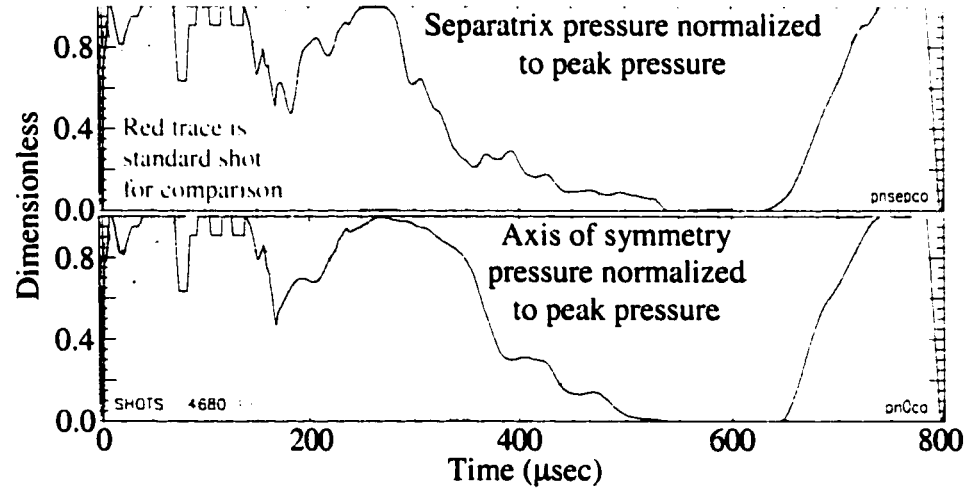


Figure 5.29 Separatrix and axis of symmetry normalized pressures

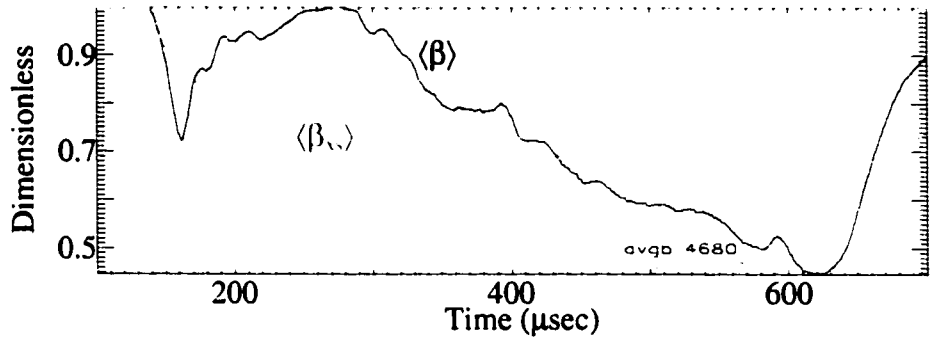


Figure 5.30 $\langle\beta\rangle$ and $\langle\beta_{xs}\rangle$ of slow flux growth shot

Actually, in the above analysis, a third assumption is being made, that the ions are not starting to spin up and rotate cosynchronously with the RMF as well. Such a motion was not seen with the Doppler measurements, though a more thorough investigation would certainly be appropriate. Based on theoretical considerations of the transfer of momentum from the electrons to the ions, one would not expect to see a spinup either, even assuming the fairly high resistivity seen during flux buildup. More convincingly though, if the ions are starting to spin up, at a certain velocity, they would exert a centripetal force that would noticeable perturb the radial pressure balance relation in a characteristic manner. Specifically, a higher $B_e$ would be needed at the edge to confine the plasma, for a given field on axis. Given the accuracy to which the internal probe can measure the radial profiles, ion rotation exceeding 10 % of the RMF rotation frequency would be detectable, and would increase $B_e$ by about 10 % relative to the reversed field on axis. Such a perturbation is not observed, and when the RMF $B_\theta$ radial pressure is accounted for, $B_z(r=0)$ is generally equal to $B_e$, at least while a reasonable degree of field reversal exists. While on the topic of mentioning additional assumptions, cylindrical symmetry is also assumed. The internal probe does cross the axis of symmetry, and it indicates that this is a good assumption to within a centimeter or so most of the time, though larger deviations have certainly been observed. The FRC is also assumed to be sufficiently long that end curvature forces do not play a roll where the internal probe is making measurements, something which is certainly true given the measured axial field profiles. STX makes long skinny FRCs, 2 m long with a 20 cm radius.

The third and most convincing demonstration that the above assumptions are valid comes from a comparison with the end on interferometer measuring the axial integrated line density at a 14 cm radius, figure 5.31. The black trace is the signal recorded from the interferometer, while the red trace is derived from the internal probe. A shot to shot axial scan was done with the internal probe making measurements between z = 0 and z = -130 cm. At each location, the density profile was calculated as described above. The resulting n(z,r) was then integrated axially at r = 14 cm to produce the red trace in figure 5.31. This procedure was done only once with no fudge factors being added, nor additional data manipulation being done, to obtain better agreement. This may not look too good at first glance, but the axial interferometer is measuring additional density outside the region scanned and then integrated for the internal probe. A Langmuir probe was used to look in one of the regions not scanned by the internal probe, and the time dependent density profile it measured is consistent with the discrepancies shown in figure 5.31.

Figure 5.32 also shows a relative density measurement made with the Langmuir probe at z = 145 cm. This placed the Langmuir probe just into the field free region on the vacuum end of STX contained within the 16 inch long by 17 inch diameter stainless steel chamber. The axial field does not enter this region because of the thick aluminum plate that supports the quartz tube, as well as all the axial field magnets. As a very rough calibration, the peak amplitude recorded by the Langmuir probe when placed into the peak density at the midplane was two times greater than the peak amplitude shown in figure 5.32. The Langmuir probe measured the greatest density at times when the deviation between the two traces in figure 5.31 are the greatest, density that would have been measured by the interferometer, but not by the internal probe. When the Langmuir probe is measuring its minimum density around 250 μsec, the two signals are in excellent agreement.

Based on what is happening experimentally, the times at which the Langmuir probe recorded a large signal make sense. The initial high signal is likely due to both the preionization ringing theta pinch as well as the decaying conventionally formed FRC. One of the periods on the initial theta pinch was deliberately extended in order to help squirt plasma out the ends and lower the density under the RMF antenna. The initially high signal only begins to drop when the RMF is turned on and begins to confine particles. During the next few hundred microseconds from the signal minimum, the Langmuir probe shows a gradual, and then rapidly increasing density. This corresponds to the FRC growing in length and pushing itself out past the RMF antennas and up against the end mirror fields. The rapid increase in density at the end occurs in conjunction with the FRC's rapid loss of flux and corresponding opening of field lines. This behavior is mirrored in figure 5.31 where the traces gradually and then rapidly diverge.

Unfortunately, there is insufficient data to make the above explanation of the differences in the interferometer and internal probe traces more rigorous, but even ignoring the above, the traces agree to within at least 25 % for the majority of the duration of the RMF driven FRC. When first plotted, this was certainly a nice confirmation that the assumptions made to analyze the internal probe data are valid. Initially, long before the internal probe data had been analyzed, the very low separatrix density was first observed by doing a radial scan with the end on interferometer. Subsequently, and with somewhat different operating conditions, a radial scan with the Langmuir probe also indicated a very low separatrix density. It is only much more recently that the internal probe has been used to produce the detailed radial density profiles. Once one knows n, $T_e$, and **B**, as functions of position and time, then many additional plasma quantities can also be calculated. Another example mentioned above is $E_\theta$, which is simply $d\phi/dt$, where $\phi$ is the integral of $2\pi B_z r dr$ from the axis of symmetry to wherever one wants to know $E_\theta$. Given STX's very limited diagnostics, it is very fortunate that the internal probe is capable of providing so much information.

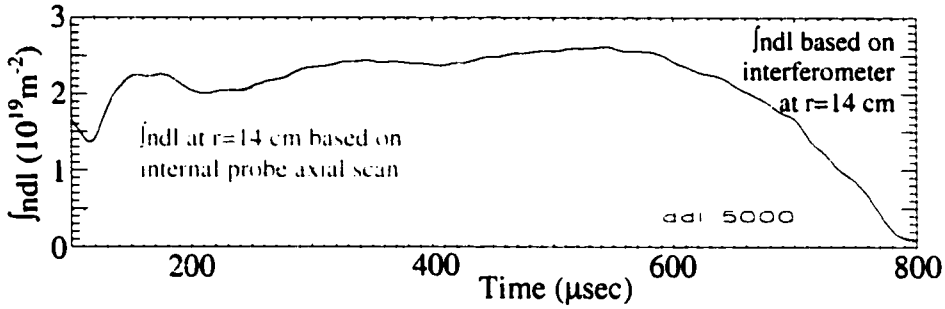


Figure 5.31 Interferometer and internal probe axial density profiles

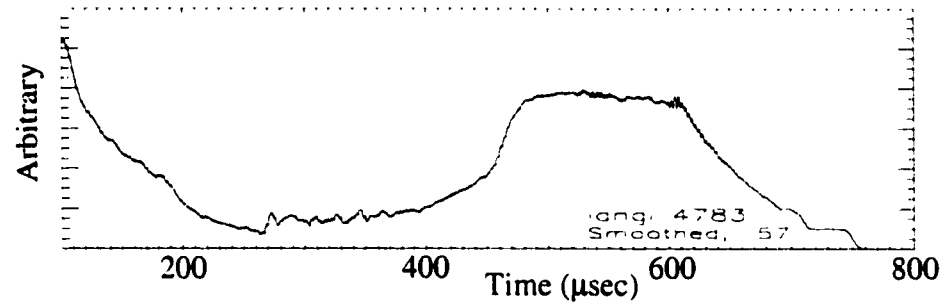


Figure 5.32 Langmuir probe density indicator at end of STX

## Plasma Resistivity

A knowledge of the plasma resistivity is of fundamental importance when considering if the RMF current drive mechanism can feasibly be scaled to reactor levels. With the data available on STX, only global estimates of plasma resistivity can be made for two different time periods, the initial rapid flux growth phase, and the gradual flux decay phase. The estimates are crude, and only place a limit on the maximum resistivity, not the minimum resistivity. The basic procedure involves a comparison of the drop in energy on the RMF energy storage capacitors with and without plasma for different plasma durations. The change in energy is directly calculated from the change in charge voltage on the capacitors. These results are summarized in table 5.1. For otherwise identical shots with and without plasma, the RMF was turned off at 200, 400, and 700 μsec. A

comparison is then made of the energy left on the RMF energy storage caps between the vacuum and plasma shot. The difference in energy used by the circuit can be related to the energy put into the plasma, which given the knowledge of the actual current profile, can be related to an average plasma resistivity.

By turning the RMF off at the three times indicated, the energy that went into initial plasma ionization and heating can be distinguished from that that used in the rapid flux growth phase as well as that used in the gradual flux decay phase. Plasma ionization and heating occurs from -275 to -75 μsec. Rapid flux growth with presumably additional plasma heating and ionization occurs from 100 to 300 μsec. The gradual flux decay phase occurs from 300 to 700 μsec. Using the three energy differences shown in the last column of table 5.1, a system of three equations can be solved to determine the average energy, and hence power, dissipated during each of these three phases. During the initial ionization 800 kW are dissipated, during the rapid flux growth 460 kW are dissipated, and during the gradual flux decay phase 60 kW are dissipated. The corresponding plasma resistivity is 130 μΩm during the rapid flux growth, and 20 μΩm during the gradual flux decay phase.

The fourth column from the end in table 5.1 shows the difference in energy consumed for each of the three sets of shots with and without plasma. The second and third columns from the end show corrections that are made to this difference in energy consumed due to changes in the circuit caused by the presence or absence of plasma. The third column from the end shows the difference in energy left in the tank circuit's capacitors that arises from the different drops in circulating voltage, vcv and vch. The second column from the end shows the difference in energy due to different average currents flowing in the RMF antenna and the corresponding difference in power dissipated due to the antennas real resistance of 23 mΩ.

Since differences between large numbers are being calculated, an assessment of the uncertainty in the difference in energy dissipated is essential. There are several potential sources of error, the effects of which were calculated by changing the appropriate numbers in table 5.1 and noticing how the final energy differences changed. Errors associated with the two corrections just mentioned are sufficiently small, being second order in nature, that they are neglected. Particular attention is paid to placing an upper bound on the energy dissipated by the plasma, and hence an upper bound on the plasma resistivity. This is in part done since it is not possible to establish a lower bound other than zero with the data available.

Table 5.1 RMF energy dissipation in the plasma

| RMF frequency | plasma present | time RMF off (msec) | shots | init. vert. charge (V) | final vert. charge (V) | init. horiz. charge (V) | final horiz. charge (V) | icv at 0.2 msec (kA) | ich at 0.2 msec (kA) | vcv at 0.2 msec (kV) | vch at 0.2 msec (kV) | p-p ipv (kA) sm=2 | p-p iph (kA) sm=2 | E off IGBT caps (J) | E left in ant. caps (J) | Icirc dis. 23 mΩ (J) | tot. diff. in E dis. (J) |
|---|---|---|---|---|---|---|---|---|---|---|---|---|---|---|---|---|---|
| 334 | n | 0.7 | 5069 | 605 | 345 | 605 | 338 | 9.8 | 11.3 | 16 | 17 | 8.2 | 7.2 | 2993 | 54 | 370 | |
| 352 | y | | 4974 | 607 | 335 | 608 | 310 | 8.6 | 10.3 | 13 | 14 | 8.3 | 7.6 | 3179 | 37 | 296 | |
| | | | | | | | | | | | difference | | = | 186 | 17 | 74 | 277 |
| 334 | n | 0.4 | 5066 | 605 | 444 | 605 | 435 | 9.7 | 11.3 | 16 | 17 | 8.2 | 7.0 | 2074 | 77 | 245 | |
| 352 | y | | 4976 | 608 | 435 | 608 | 415 | 8.8 | 10.3 | 13 | 14 | 8.5 | 8.1 | 2267 | 55 | 203 | |
| | | | | | | | | | | | difference | | = | 193 | 22 | 42 | 258 |
| 334 | n | 0.2 | 5065 | 605 | 520 | 605 | 513 | 9.9 | 11.5 | 17 | 17 | 8.5 | 6.9 | 1191 | 102 | 111 | |
| 352 | y | | 4978 | 606 | 515 | 607 | 498 | 8.6 | 10.0 | 13 | 14 | 8.7 | 7.9 | 1331 | 63 | 84 | |
| | | | | | | | | | | | difference | | = | 140 | 38 | 27 | 206 |
| 333 | n | 0.7 | 5075 | 605 | 350 | 605 | 344 | 10.0 | 11.7 | 16 | 17 | 8.0 | 7.3 | 2947 | | | |
| 334 | n | 0.7 | 5070 | 605 | 345 | 605 | 340 | 9.9 | 11.1 | 16 | 17 | 8.4 | 7.3 | 2985 | | | |
| 336 | n | 0.7 | 5074 | 605 | 335 | 605 | 328 | 9.5 | 10.3 | 16 | 16 | 8.3 | 7.9 | 3073 | | | |
| 339 | n | 0.7 | 5073 | 605 | 320 | 605 | 310 | 8.3 | 8.3 | 14 | 13 | 8.9 | 8.7 | 3201 | | | |

The first possible source of error is that all of the voltage measurements were too high or too low by +/- 5V. This error produces no change in the energy differences. The second possible source of error is that only the voltage on either the vacuum or the plasma shots was off by +/-5 V. This would produce an error of +/- 20 J. Based on a

careful analysis of the data, it appears that all of the plasma shots were artificially high by +2.5 V. This would result in -30 J being added to all the energy differences. The third possible source of error is statistical in nature. There is a +/- 2.5 V uncertainty in any measurement due to the error of a single digital count. Since 8 measurements are combined in the above voltages, this corresponds to an effective +/- 1 V error in the voltages displayed. If this statistical uncertainty were applied in a systematic manner to maximize the error to just the initial voltages of either the plasma or vacuum shots, a +/- 15 J uncertainty would arise. Specifically, adding 1 V to the initial plasma voltage only creates a +15 J error, while subtracting 1 V from the final plasma voltage creates a + 10 J error. It is highly improbable that a statistical error would occur in such a systematic manner, but a reasonable upper bound is being looked for. Another indication of the uncertainty arises from the shot to shot reproducibility. Unfortunately, only 2 identical shots were taken, and these differed by 7 J.

The largest potential error arises from circuit detuning and its impact on the energy dissipated. The four final rows in table 5.1 show the behavior as the circuit is detuned from 333 kHz to 339 kHz. A comparison of the tuned and untuned current and voltages, icv, ich, ipv, iph, vcv, vch, including specific details of time dependent behavior, indicates that with plasma present, the circuit was not tuned as well as in vacuum. This would result in the circuit itself dissipating more energy and would reduce the value attributed to the plasma. An estimate is -100 J, though the number could be a lot bigger. This is the reason for the inability to assign a lower bound. It is fortunate that the circuit was more detuned with plasma than in vacuum, even accounting for the change in frequency, since otherwise, a meaningful upper bound would have been difficult to assign. Based on the above uncertainties, error bars of +10 $\mu\Omega$m and -20 $\mu\Omega$m are placed on the resistivity during flux decay of 20 $\mu\Omega$m. A similar upper bound would apply to the 130 $\mu\Omega$m inferred during the flux driveup phase.

A few interesting comparisons can be made with the resistivity calculated from flux decay rates. On shots 4976 and 4977 where the RMF was turned off at 400 μsec, by 445 μsec the RMF amplitude was down by 2 e-foldings. The FRC flux decay rate, $d\phi/dt$, was 3.1 and 2.6 V, which when combined with the null radius of 11 and 10 cm, produced an $E_\theta$ of 4.5 and 4.1 V/m. The current density at the null based on $dB_z/dt$ was 40 and 70 $kA/m^2$. Solving Ohm's law $E = \eta j$ for $\eta$ results in a resistivity of 112 and 59 μΩm with an average resistivity of 85 μΩm. The resistivity of this plasma based on the standard FRC relationship, $\tau_\phi = \phi/(d\phi/dt) = \mu_0 r_s^2/16\eta$, is 63 μΩm. The classical resistivity of this plasma is 1.6 μΩm.

For the driven plasmas during their gradual flux decay phase, the flux decay rate is also characteristic of a 20 μΩm resistivity, a number which is in very nice agreement with the above global resistivity calculated from RMF antenna loading, assuming no RMF drive at the null. Partial RMF drive should make the apparent resistivity based on the flux decay rate less than that based on the global measure. If one assumes no RMF drive for either case, the difference between the driven flux decay resistivity of 20 μΩm and the undriven flux decay resistivity of 85 μΩm is just what would be expected given the difference in the axial field gradient across the null for the two shots. In the plasma where the RMF is turned off, the field gradient is typical of a conventional FRC, and is approximately four times bigger than the gradient in the driven plasma during its gradual flux decay phase. Typically, as can be seen in figure 5.15, the field gradient at the null is much flatter when the plasma is in its gradual decay phase than when the flux is actively being driven up. Interestingly, for the plasma shown in figure 5.25 where the flux gradually increased for the duration of the shot, there is no pronounced flattening of the field gradient across the null.

# CHAPTER 6
# STX DATA AND THE RMF FRC INTERACTION

## The RMF and the FRC Equilibrium

The observation of partial RMF penetration came as quite a surprise given the standard RMF theory prior to the construction of STX. An FRC must satisfy its $\langle\beta\rangle$ condition, and full RMF penetration and the associated cosynchronous electron rotation appear to be inconsistent with such an equilibrium, both experimentally, as well as when modeled numerically[18] and analytically[8]. This is not as general a statement as it might sound, and there are particular profiles, such as the rigid rotor, where full RMF penetration is consistent with the FRC equilibrium. The primary reason for this discrepancy between the RMF and FRC equilibrium lies with the experimental observation that the separatrix density is low. Given how strongly the RMF appears to drive an inward radial flow, this may always be the case, but the analytic model assumes a low separatrix density from the get go and thus only observes partial penetration.

The statement that full RMF penetration is consistent with the rigid rotor profile makes many assumptions, possibly a sufficient number that it may have no bearing on reality. When the true physics of the FRC RMF interaction is understood it may become apparent that full RMF penetration is never a possibility. However, since much of the STX experiment was conducted during a time when full RMF penetration was considered to be an accurate understanding of the RMF FRC interaction, and since it was data from the STX experiment that first threw this understanding into doubt, the following discussion will present the currently understood physics with a slant towards explaining why only partial RMF penetration is observed.

Actually, in addition to past history, there is a real physical reason to discuss the RMF in terms of its penetration depth, especially during the period of initial flux buildup. The

RMF is observed to vary its penetration depth, and hence the current driven, much faster then the FRC responds axially. Thus it makes a certain amount of sense to discuss how the FRC equilibrium responds to such changes in the RMF penetration depth since the change in RMF penetration precedes the relaxation into an equilibrium. Also, viewing the RMF as something that must penetrate a certain distance may also aid in understanding its interaction with axial flows.

Having said this, the current understanding of the RMF FRC interaction does not directly address or invoke the issue of penetration depth, though it can be explained correctly, as will be done, by discussing what happens as the penetration depth is varied. Rather the equilibrium is set by the RMF drive torque balancing the resistive drag. If the RMF drives a little too much current, the FRC expands, $B_z$ and n increase, the resistive drag increases, a little less current is driven, and a stable equilibrium results. The understanding is based on a 2-D problem, and other then the $\langle\beta\rangle$ condition, physics involved with the third dimension, the z axis, has barely been addressed.

For cases with strong RMF drive, the numeric model produces the same low separatrix density that was assumed in the analytic model. In the numeric model, given an existing FRC, an equilibrium is attained as follows. The RMF penetrates a certain distance based on its drive force balancing the resistive drag of the plasma. If the RMF penetrates a little farther, it drives a little more current, the internal field increases, and the FRC expands radially. This expansion compresses the coil flux and increases the external field. The density increases, in a manner dependent on how the temperature is modeled, sufficiently to maintain radial pressure balance with the increasing external field. The process continues until the RMF drive and resistive drag forces balance. The model has no length dependence, but in actuality, as the FRC expands radially the end magnetic curvature forces would increase and the FRC would shrink axially. This is the source of the increase in density that appears numerically.

As mentioned, the model does not have any explicit z dependence, but it does account for the FRC's axial equilibrium constraint by adjusting n appropriately, in this case increasing it as the FRC shrinks. The model adjusts its density profile through stipulation of flow from inner to outer flux surfaces and also through a stipulation of a minimum density outside of the separatrix. The particles are moved based on maintaining p as a function of $\psi$, but the time taken for them to move in response to differences in flux surface pressure is kept unrealistically short. As the RMF drives particles radially inwards, others reappear on the outside with a very short time delay, and the reverse happens near the axis of symmetry. In STX, in order for particles to move from the inner to outer flux surfaces, axial flows must arise that carry the particles around the FRC's ends. These axial flows take time, and the RMF is very clearly seen to drive p away from a function of $\psi$, various aspects of which can be seen in figure 5.7, figure 5.11 and figure 5.12. The physics of such axial flows, as well as their interaction with the RMF and FRC, are fundamentally not contained within the simulation because of the simulations two dimensional nature. This may be a very important difference between the simulation and the experiment, especially with regards to the axially flow's potential ability to partially screen the RMF.

Keeping in mind some of the limitations of the model just discussed, a problem arises when the numeric model is used to simulate the STX experiment. In order to achieve the correct machine parameters during STX's flux buildup, the model uses a resistivity of 112 $\mu\Omega$m, a value in close agreement with the resistivity of 130 $\mu\Omega$m measured during this time. However, if the experimentally measured value of 20 $\mu\Omega$m during the flux decay is used, the model predicts a much higher density and field equilibrium then is observed. In the model, it is the high resistivity that keeps the fields and densities low by restricting the amount of current the RMF can drive. If axial flows partially screened the RMF, they might also provide such a restriction, and naturally allow for the use of a lower resistivity more in agreement with the 20 $\mu\Omega$m measured. It would certainly be

interesting to see the effects of axial flows accounted for in the model. It is worth noting that for no value of $\eta$ does the model lead to a gradually decaying FRC as seen in STX.

**RMF Induced Oscillations**

An interaction between the RMF and FRC equilibrium was clearly seen with regards to the equilibrium length of the FRC. To date, all the modeling of RMF driven FRCs has assumed infinitely long plasmas, something not changed by the imposition of the $\langle\beta\rangle$ axial pressure balance condition. A spatially uniform RMF by its very nature is going to try and drive an axially uniform current profile, whatever its equilibrium penetration depth is. Unfortunately, real FRCs do not have an axially uniform current profile. Rather, as shown in figure 6.1, substantially less current flows at the ends where the field curvature is high. Contours of constant current density are shown. In STX, when the plasma was shorter than the RMF antenna, a strong dynamic oscillatory behavior was observed, most prominently at the ends. It is believed to have arisen from the RMF trying to drive more current at the ends than the FRC equilibrium desired. Figures 6.2 a, b, c, d, e and f show plots of the internal field profiles at various axial positions. Refer to figure 5.3 or figure 5.24 for the specific radii of particular traces. Notice the strong oscillation between 250 and 450 μsec, an oscillation which becomes much more pronounced as one moves toward the ends. As the plasma grows sufficiently past the antenna, the oscillations disappear. Though the length of the FRC with respect to the RMF antenna is likely what is determining the presence or absence of these oscillations, the length of the FRC itself should be governed by basic FRC equilibrium constraints. If the energy content is held constant, FRCs shrink axially as their flux increases, and grow axially as their flux is lost. The STX FRCs are initially formed the length of the RMF antenna. The rapid initial flux driveup causes a rapid axial contraction, and then as the flux gradually decays, the FRCs gradually lengthen.

The oscillation is believed to occur in the following manner. Initially, the RMF drives more current at the end than the FRC desires. The length of the FRC increases as the extra current extends the flux surfaces axially. The FRC density and pressure drop as the particle inventory spreads over the greater volume. But now, the FRC is out of equilibrium with its $\langle\beta\rangle$ condition, and it contracts axially to bring the pressure back up to that needed. An oscillation could certainly result. More direct evidence that this is the case is shown in figure 6.3 which makes a comparison between the oscillations in the poloidal flux, and the oscillations in the separatrix pressure at z = -90 cm. When the RMF is rapidly driving up current, it is observed to sweep particles radially inwards, a point to be discussed subsequently. Thus, as the flux builds, one would expect the separatrix pressure to drop. This is exactly what is shown in figure 6.3 where the oscillations in poloidal flux and separatrix pressure are 180 degrees out of phase. This activity may not be too healthy for the FRC, but it is also believed not to be the primary cause of the loss of drive. The oscillations only started after drive was lost, and the lack of drive continued long after the oscillations had stopped. The STX RMF antennas were deliberately made long to create the theoretically ideal RMF, i.e. one that was spatially uniform. However, given the discrepancy in current drive that will likely always occur at the end of the FRC between what the FRC needs and what the RMF wants, the best approach could well be to make the RMF antenna substantially shorter than the FRC.

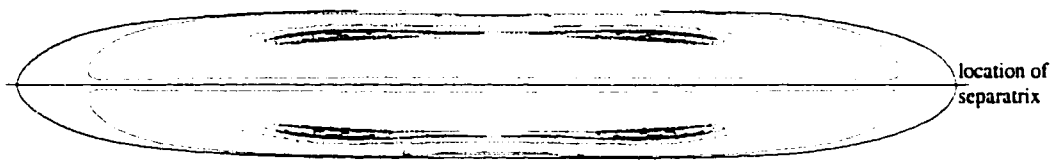


Figure 6.1 MOQUI generated FRC, contours of constant current density

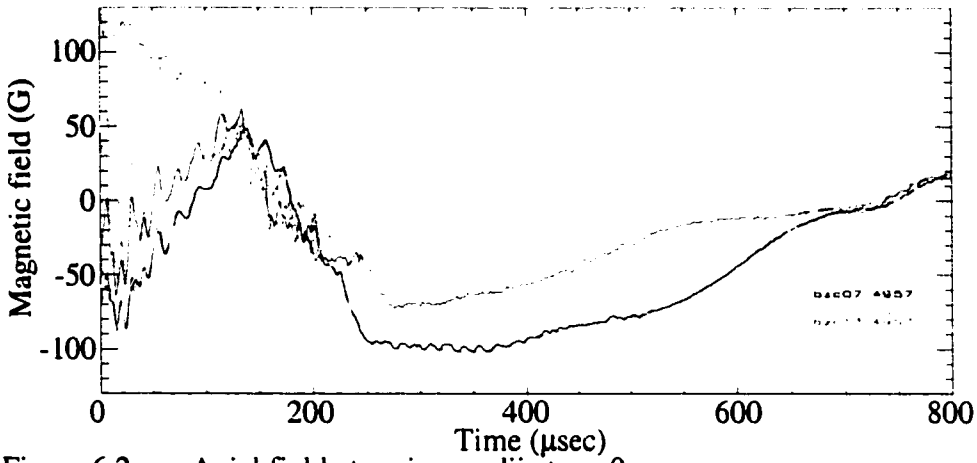


Figure 6.2a Axial field at various radii at z = 0 cm

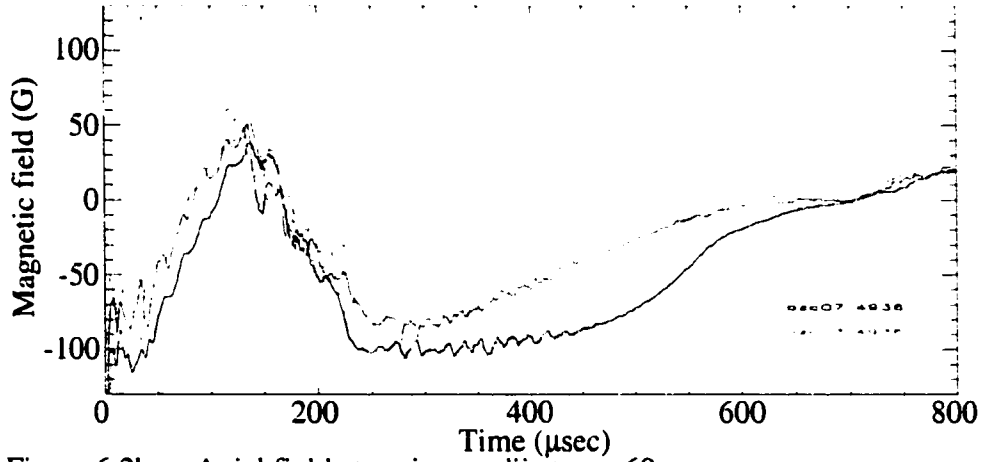


Figure 6.2b Axial field at various radii at z = -60 cm

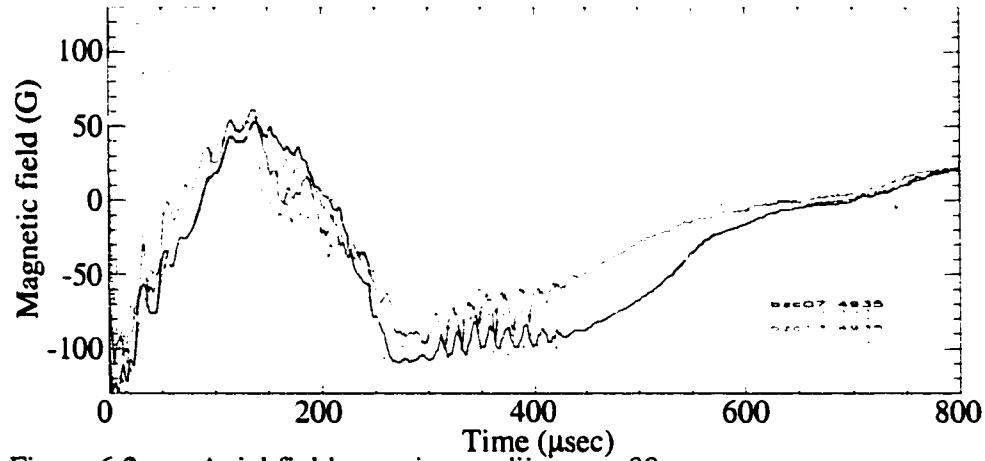


Figure 6.2c Axial field at various radii at z = -80 cm

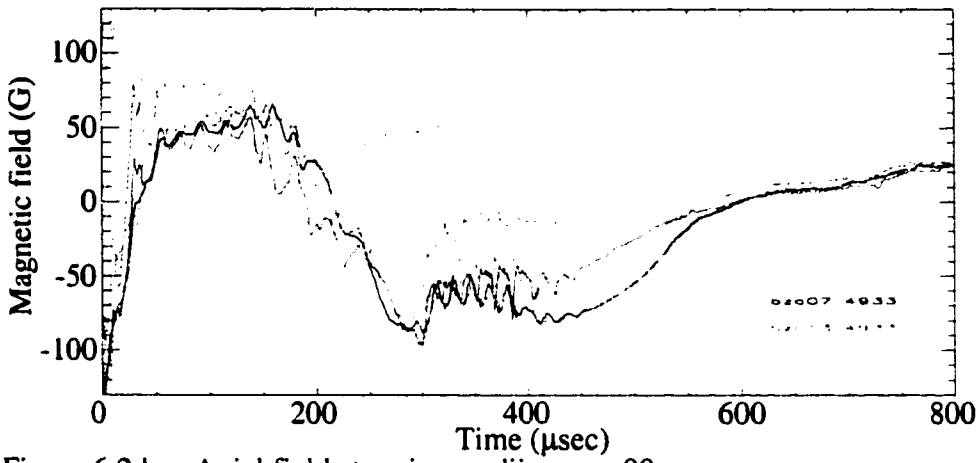


Figure 6.2d Axial field at various radii at z = -90 cm

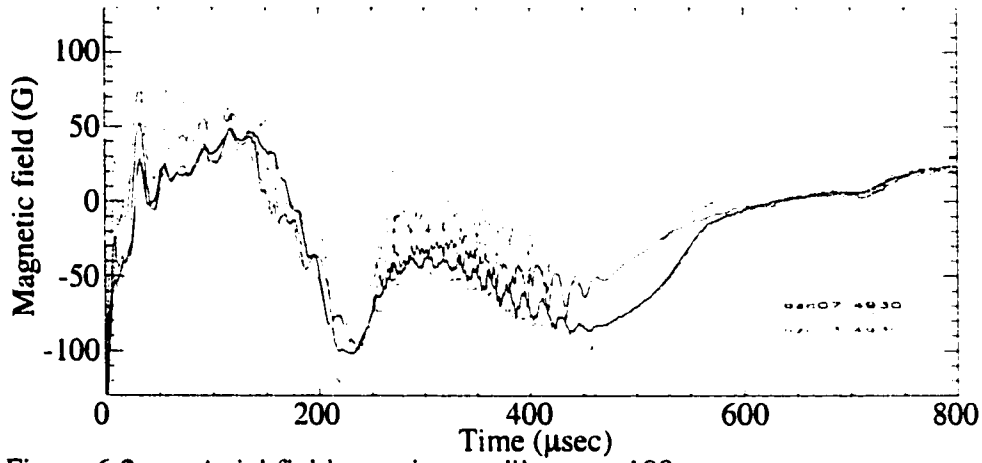


Figure 6.2e Axial field at various radii at z = -100 cm

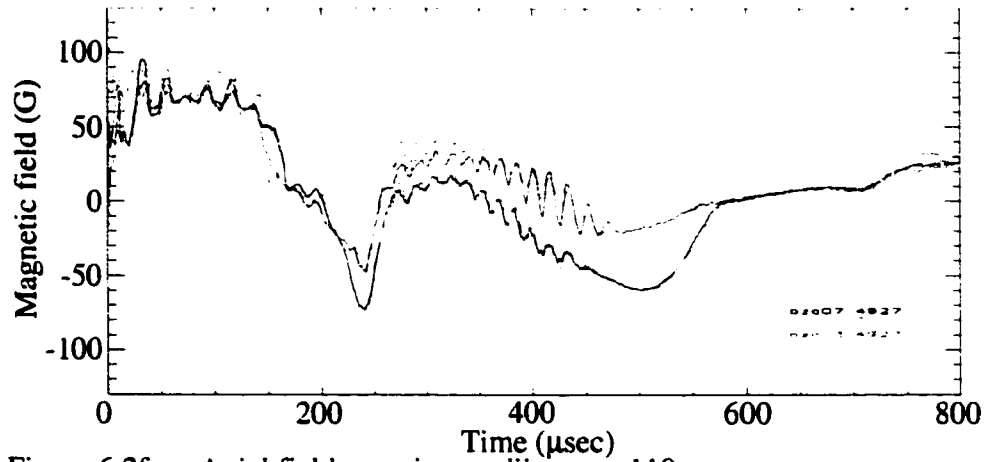


Figure 6.2f Axial field at various radii at z = -110 cm

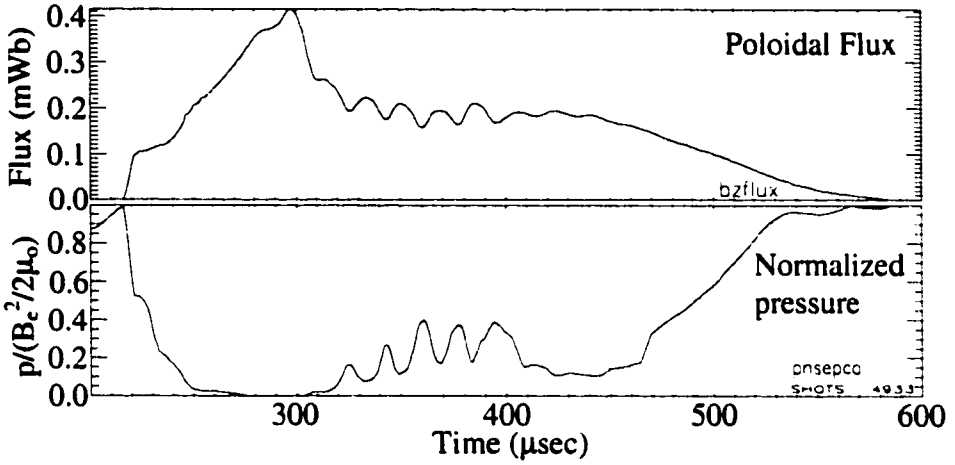


Figure 6.3 Oscillations in poloidal flux and separatrix pressure

## Radial Flow

Since the RMF does not fully penetrate the plasma, something which the theory indicates will always be the case for elongated FRCs in a flux conserver, inward radial flow becomes essential for sustaining the current on the inner field lines. The flow can close on itself by flowing axially along the axis of symmetry to the ends of the FRC, out and around on the poloidal field lines, and then axially back in towards the center on field lines near the separatrix. Where the RMF does not penetrate, the flow that needs to occur must be strong enough that $v_r B_z$ balances $\eta j_\theta$ in Ohm's Law. Since in a non-driven decaying FRC $v_r B_z$ is always somewhat less then $\eta j_\theta$, resulting in a negative $E_\theta$, there must be some feature, such as an effective particle sink, that allows $v_r$ to be larger in the RMF driven FRCs. This is the present understanding of how flows are important and occur based on the underlying physics. It would certainly be nice if STX had the diagnostics to explicitly confirm this, as well as point out how and why the drive failed. Unfortunately, such clear data does not exist, but STX data does provide clear circumstantial evidence as to what is occurring.

To begin, it is worth considering the relative magnitude of the terms in Ohm's law, equation 2.3, as they are experimentally measured in a region midway between the null and the separatrix. During the growth phase, $E_\theta$ is at most a few V/m, while during the decay phase, it is typically less than a V/m. Based on a flux growth resistivity of 130 $\mu\Omega$m, $\eta j_\theta$ has a peak around 25 V/m, while during the decay phase with a resistivity of 20 $\mu\Omega$m, $\eta j_\theta$ has a peak around 4 V/m. During both growth and decay, the RMF drive term has a value around 20 V/m. It is calculated as $0.5 j_z B_r$, where the 0.5 arises from taking the average of two in phase sinusoidal components. $j_z$ is calculated from the gradient in $B_\theta$. $B_r$ is directly calculated from $B_\theta$ by integrating $B_\theta$ from the axis of symmetry on out and by assuming $B_\theta$ has a pure n = 1 mode and is 90 degrees out of phase with $B_r$, something the numeric simulation indicates should be a fairly good assumption. A factor of 2 would be a reasonable uncertainty to assign these numbers

Based on Ohm's Law, these measurements clearly indicate the presence of a large radial inwards flow half way between the null and the separatrix during the decay phase of the FRC. In this region, $E_\theta$ is small compared to the other terms and will be ignored, though certainly it is what directly governs flux growth and decay. During the growth phase the RMF drive term is measured to approximately equal the resistive drag term, but during the decay phase the RMF drive term dominates the other two terms. This means that during the decay phase, in this region, the radial inwards flow must be quite large since $B_z$ has remained about the same and the $v_r B_z$ term is the only free term left in Ohm's law to balance the observed large RMF drive term. The flow speeds necessary to balance the RMF drive term are on the order of a few thousand m/sec. At this velocity, the entire FRC inventory would circulate in under 100 $\mu$sec, based on the density being about half its peak value where the flow is at its maximum and these measurements are made.

The above is based on the empirical observation that $E_\theta$ is small while the RMF drive term remains persistently large. Ohm's Law has two free parameters, $E_\theta$ and $v_r$. If $E_\theta$ is

small, then $v_r$ must be large to balance the RMF drive term. This does not explain why $E_\theta$ is small, other then to say that the plasma can apparently thwart efforts to create $E_\theta$ by driving flows instead. This is true everywhere except at the null where the $v_r B_z$ is zero. If one can get a particular amplitude of RMF penetration at the null, and one knows $\eta j_\theta$ there, then one could precisely determine $E_\theta$ and hence the rate of flux growth or decay. The best chances of RMF penetration to the null likely occur in low $\langle\beta\rangle$ plasmas where the $B_z(r)$ profile more closely matches the profile based on cosynchronous electron rotation needed by the RMF for penetration. High $\langle\beta\rangle$ profiles have a magnetic profile resulting from an edge current spike which is not consistent with the profiles created by the cosynchronous electron rotation needed for RMF penetration to the null. From a very different perspective, low $\langle\beta\rangle$ profiles have relatively fewer particles which should make deeper RMF penetration easier. In any case, for the reason of RMF penetration to the null, it could be very important to maintain low $\langle\beta\rangle$ plasmas.

There are three other pieces of experimental data that clearly point towards the existence of radial flow. The first is quite obvious. STX maintains a 50 eV plasma less than a centimeter from the vacuum wall, even when some of the field lines tie directly into the wall due to the separatrix being outside the vacuum wall, not to mention the large transverse RMF there, and even though there is a very steep density gradient pointing straight at the wall barely a centimeter away. Something must be actively countering diffusion and sweeping the particles in. This is certainly an explanation as to why the separatrix density, figure 5.11, can remain so much lower than the density on the axis of symmetry.

The second piece of evidence is shown in figure 6.4a, a plot of the time evolution of the pressure profile near the separatrix during the initial flux buildup phase. As time proceeds, inventory is clearly swept in away from the separatrix. The profiles have been shifted so that the position of the separatrix radius remains fixed at the value it had on the first trace, since it is the motion with respect to the separatrix that is important. The RMF

stops driving flux up at about the same time it stops sweeping these particles in. Given that the flux is actively being built up at this time, and that as a result field lines created at the null are moving radially outwards through the magnetized plasma and transporting addition inventory above that expected from diffusion alone towards the separatrix, the RMF is extremely effective at not only countering $\eta j_\theta$, but also at reversing normal outwards radial diffusion.

Figure 6.4b shows a similar plot for a different shot later in time. Different shots have been used to most clearly show the profile evolution, though profile evolution similar to that shown in these two figures has been seen in all shots when looked for. At first glance, and as based on the conventional wisdom of the FRC RMF interaction, Figure 6.4b would seem to quite clearly illustrate the ineffectiveness of the RMF later in time at countering radial diffusion, since the inventory is clearly moving radially outwards with respect to the separatrix. However, as will be discussed in much greater detail subsequently, this profile motion with respect to the separatrix is believed to have virtually nothing to do with the effectiveness of the RMF at driving current or countering outwards radial diffusion. Rather, it will be shown that for most of the duration of the RMF, the RMF maintains a fairly constant penetration depth with respect to the vacuum wall, and that within this penetration depth, the density and field profiles also remain fairly constant in time. The radius of the plasma pressure maximum, figure 6.13, is observed to be independent of $r_s$, the null, or virtually any other plasma parameter. Consequently, the motion shown in figure 6.4b appears to be simply due to the separatrix pulling away from the region of RMF penetration and current drive, and not due to any growing ineffectiveness of the RMF itself.

The third piece of evidence is shown in figure 6.5, a plot of the radial $B_z$ profile in what has been termed the ring state. This state is stable, and it very rapidly evolves from the high $\beta$ plasma column as soon as the last bit of reversed field has disappeared. In shots where the RMF does not initially attain field reversal, the plasma directly evolves

into this ring state. It has similar densities and temperatures as the field reversed plasmas even though it is an open field configuration. However, there are still strong mirrors at the ends that likely help confinement. The ring state is quite peculiar, consisting of two counter rotating current rings. The outer one is the standard one driven by the RMF in its region of penetration. The inner one flows in the opposite direction and can only be sustained by radial flow since the RMF does not penetrate to it. Instead, it is sustained in the same manner as a simple theta pinch plasma. As long as there is no field null, radial flow can counteract $\eta j_\theta$ throughout the entire plasma and maintain a zero $E_\theta$. If one moves the origin of the r axis to the field minimum, this profile would look exactly like that of a standard theta pinch plasma. In this case, the RMF drives plasma inwards over its region of penetration, and maintains a density maximum at r = 15 cm rather then at r = 0 cm. The positive density gradient inside r = 15 cm then maintains the oppositely directed inner current ring. The evolution of the high beta plasma column into the ring state is a clear indication of flow. This state is particularly well illustrated in the plots in figure 6.6 from 450 to 550 μsec. The existence and persistence of the ring state remained a puzzle for many years until the importance of flow was realized. It was observed very early on, but could not be explained without flow. Figure 6.22, 6.23 and 6.24 also nicely illustrate the ring state, and how it correlates with various parameter scans.

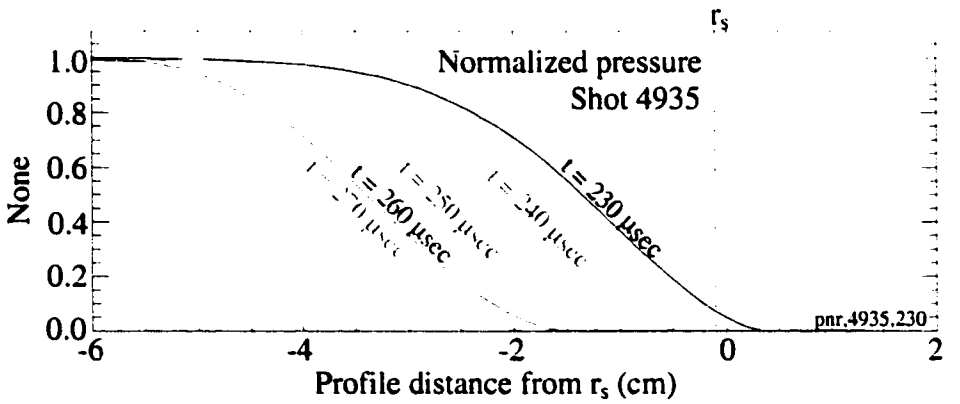


Figure 6.4a Time evolution of pressure profile during rapid flux growth near $r_s$

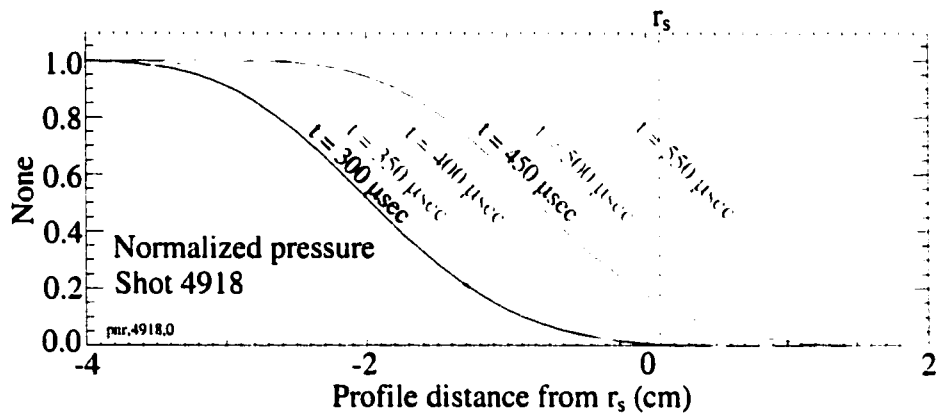


Figure 6.4b Time evolution of pressure profile during slow flux decay near $r_s$

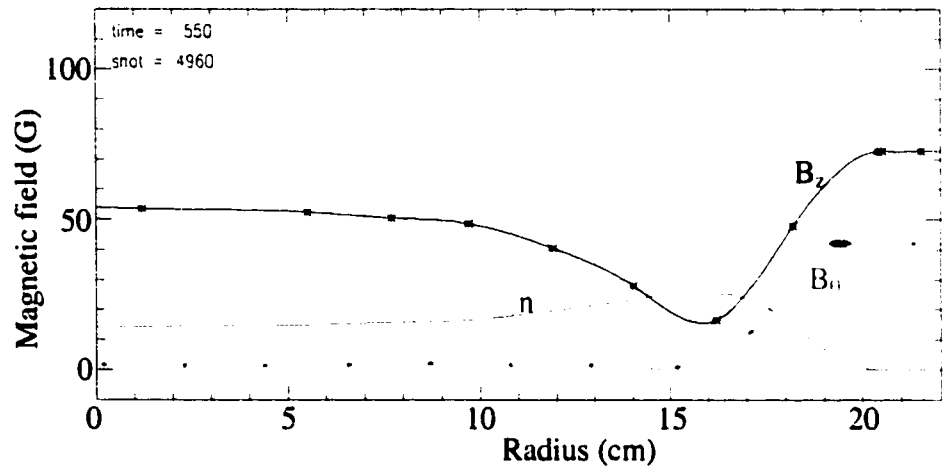


Figure 6.5 Ring state radial field profile

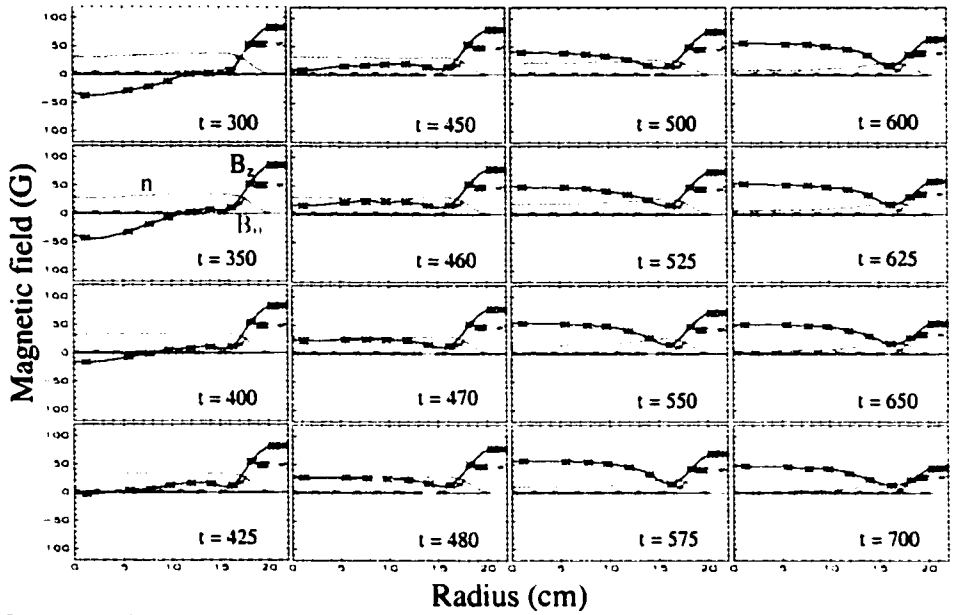


Figure 6.6 Time evolution of ring state radial field profile

## Axial Flow

Information about axial flows is more limited. In order for the RMF to drive radial flow, it must have a 'source' of particles outside the null and a particle 'sink' inside the null. Such a sink can only be maintained through axial flow, and is essential in maintaining the density gradients needed for proper radial flow and effective current drive. Figures 5.12, 5.11, 5.15 and 5.4 all provide indications that axial flow is indeed being restricted. Specifically, if axial flow was restricted for some reason, one would expect the pressure inside the null and on the axis of symmetry to build, shown in figure 5.12 and figure 5.11, the field gradients to be reduced, shown in figure 5.15, and flux to be lost, shown in figures 5.4.

Figure 5.12 also indicates how the plasma may respond to a flow restriction. At any location where a flow restriction increased preferentially as one moved radially inwards from the null, the density gradient would be reduced. A reduction in the density gradient would reduce the inward radial flow due to diffusion. This in turn would reduce the

current driven which would result in flux loss at that location. If there were not some sort of monotonically increasing restriction to axial flow as one moved radially inwards, then density piling up at one radial location would actually tend to increase the density gradient at slightly smaller radii, and thus help to sustain the drive further in. The net effect might be that the entire density profile simply shifts radially inwards as loss of drive near the null propagates additional drive further in. Such behavior is shown in figure 5.12 where the peak density gradient remains approximately constant in time, but the entire profile moves radially inwards. This process must stop, as it does in figure 5.12, when the density gradient encounters the axis of symmetry, and the small remaining core of field fills in.

Interestingly, the buildup of inventory would not necessarily upset radial pressure balance requirements since as flux is lost, space is naturally made for an increased plasma pressure. Such a transition would not be consistent with a traditional FRC's $\langle\beta\rangle$ condition, but if the $\langle\beta\rangle$ condition itself were changing to allow higher $\langle\beta\rangle$, an issue to be discussed subsequently, or for some other reason the $\langle\beta\rangle$ condition did not apply, another issue to be discussed subsequently, then one would expect the plasma to naturally evolve into the high $\beta$ plasma column that is observed and which is consistent with a stifled axial flow. The loss of current drive and flux naturally accommodates the building pressure.

Actually, the high $\beta$ plasma column is experimentally observed to not be a steady state configuration. As soon as it forms, it rapidly evolves into the ring state described above. This is as expected, since once all field reversal is lost, the inward flow driven in the region of RMF penetration naturally sweeps forward open field in with it, field which accumulates near the axis of symmetry, Figure 6.6. Interestingly, the work, though not torque, required of the RMF is minimized in the high $\beta$ plasma column state which only has a field gradient of $\Delta B$. Both the FRC and ring state have a field gradient of roughly $2\Delta B$ and take about twice the work to sustain. On the other hand, the FRC feels the maximum torque since its currents all flow in the same direction, while the ring state

feels virtually no torque since its currents flow in opposite directions. The fact that the RMF can sustain a field gradient of $2\Delta B$ in the ring state but not the FRC state even though the work required is similar, is consistent with the hypothesis that axial flow is being stifled in the FRC and forcing the FRC to evolve into the ring state, a state where such flows are much less likely to be restricted due to its open field configuration with inner field lines terminating in a wall far from the RMF antenna. In the FRC, the flow must loop around on the closed field lines under the ends of the RMF antenna, a path possibly fraught with restrictions.

Another piece of evidence suggestive of axial flows is shown in figure 6.7, a plot of the poloidal flux as a function of time and axial position. The fact that the poloidal flux is greater at the ends of the machine came as quite a surprise, and indicates a stronger RMF current drive there. This observation can be explained by the knowledge that the ends of the FRC are closest to the source of particles returning from 'the end run'. To work, the RMF seems to require large flows, and being near the source of particles could certainly help. But if being near the source helps, this can also help to explain the failure of drive near the middle of the machine. The particles are driven radially in before they have time to flow to the midplane, leaving the RMF there starved of particles and forced to work harder on those farther in. This stripping of particles from the field lines as they flow axially towards the midplane could be the mechanism that keeps p from being a function of $\psi$. An axial scan of the separatrix pressure supports this belief, figure 6.8, and shows that during the time of gradual flux loss as one moves axially away from the ends of the RMF antenna and towards the middle of the machine, the separatrix pressure falls.

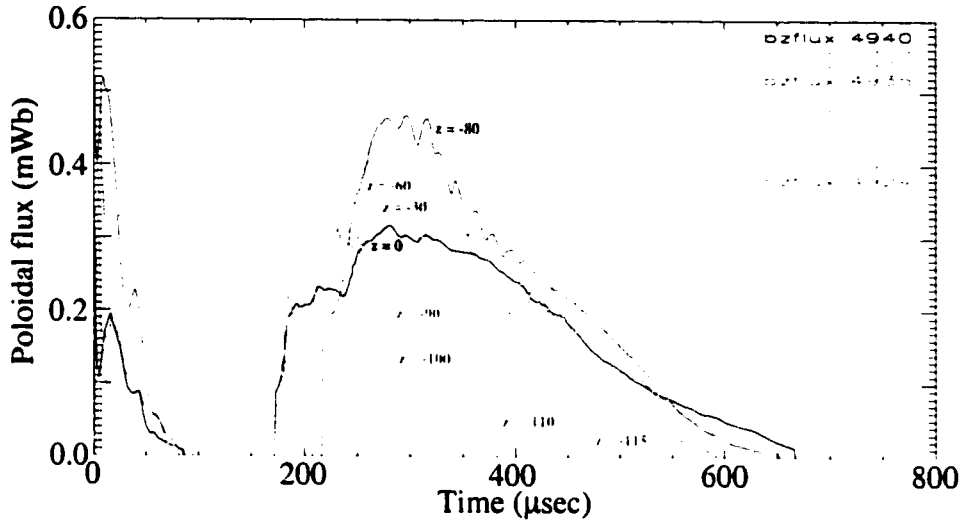


Figure 6.7 Poloidal flux as a function of time and axial position

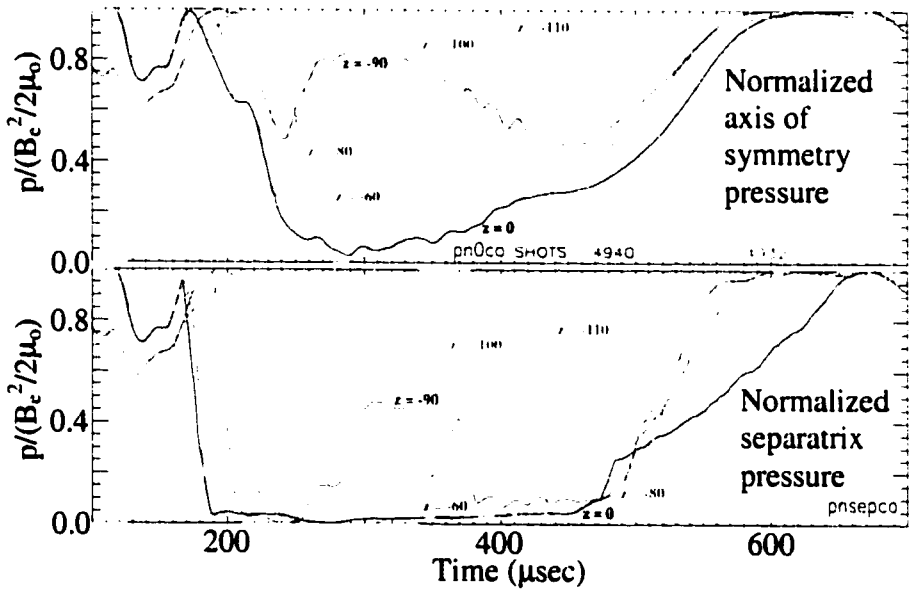


Figure 6.8 Separatrix pressure as a function of time and axial position

Figure 6.8 also shows the pressure evolution at the axis of symmetry at various axial locations. Interestingly, the pressure rises instead of falls as one moves towards the end of the FRC, something possibly inconsistent with the idea that plasma is flowing axially out of the FRC due to an axial density gradient, though the axis of symmetry is a rather

special field line and may not indicate what is happening somewhat closer to the FRC null. Rather the increase in pressure near the ends could be due to the known presence of open field plasma at the ends of STX. Still the fact that the pressure does stay so low on the axis of symmetry near the midplane of the FRC does indicate the action of some axial force driving particles off of it as they diffuse radially inwards. Under many different conditions, the RMF rapidly drove up the FRC, only to immediately loose drive, something that is consistent with the belief that the RMF works well as long as it has a source of particles. The fact that the RMF could steadily drive up the flux on shots where the preionization was stifled is also consistent with this explanation. The week preionization left many neutrals behind which were gradually ionized and driven in by the RMF for the duration of the shot.

At the ends of the FRC, the RMF is far from the ideal assumed in the theory. Actual fields may have adversely effected the necessary axial and radial flows. Currents flowing in the ends of the RMF antenna generate additional oscillatory $B_z$ and $B_r$ components. The $B_z$ component generates a time averaged mirror, one that can get quite strong given the amplification due to screening currents flowing in the plasma. In addition to the possibility of the mirror restricting flow, it is quite possible that other $\mathbf{j}\times\mathbf{B}$ forces exists that also restricts flow from coming around the end. One possibility comes from looking at the radial component of $\mathbf{j}\times\mathbf{B}$. Both the $j_{\theta AC}B_{zAC}$ and the $j_{zAC}B_{\theta AC}$ potentially create a steady inward force at both ends of the plasma that could restrict flow. All four components are AC in nature as indicated by the subscript. $j_{\theta AC}$ is the screening current that flows to keep $B_{zAC}$ out of the plasma while $j_{zAC}$ is the overall axial screening current that flows to keep $B_{\theta AC}$ out of the plasma. All of the products of a DC term with an AC term likely average to zero. Of the two remaining terms, the $j_{\theta DC}B_{zDC}$ is the standard term balancing plasma pressure, and the $j_{zDC}B_{\theta DC}$ is zero since there is likely no $j_{zDC}$.

The interest in looking for such a restriction arises in looking for an explanation as to why p is not a function of $\psi$. One has been proposed above, that the RMF is actively

driving particles in on the outer flux surfaces, but there may be other possibilities. A restriction of flow around the ends could not only explain the deviation of p from a function of $\psi$, but also explain the increase in the plasma $\langle\beta\rangle$ as discussed above. Figure 6.8 does provide some indications as to where the restriction may be occurring. Pairs of traces from this figure are compared in figure 6.9 where one can explicitly see the deviation between the separatrix and axis of symmetry pressure at each axial location measured. The separation between the curves is a minimum at the very end of FRC far from the RMF antenna, and a maximum just inside the RMF antenna at z = -90 cm. It then falls as one moves towards the midplane. The above discussion is primarily focused on the FRC's gradual decay from 300 to 500 μsec while a reasonable amount of field reversal exists. From 500 to 700 μsec, the pressure on both the axis of symmetry and the separatrix increases substantially, though a gradient between the inner and outer field lines is still maintained. Certainly a more thorough investigation of the complicated fields and plasma structures at the end of the RMF antenna is needed, especially with regards as to how they effect the equilibrium. This is however another reason why it may be important to keep the length of the RMF antenna sufficiently shorter than the length of the FRC.

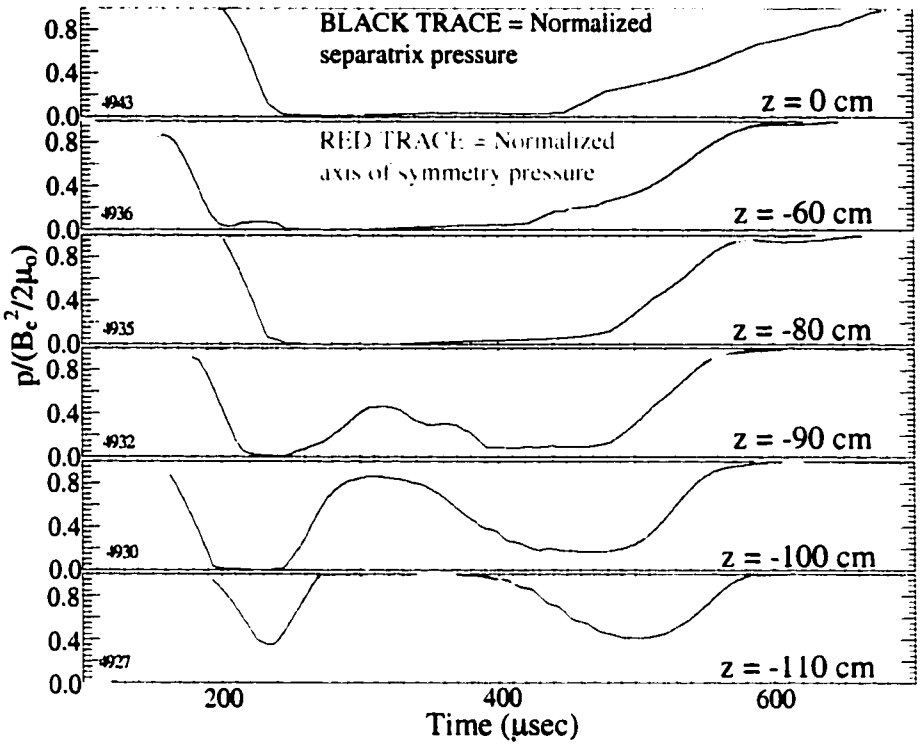


Figure 6.9 Comparison of separatrix and axis of symmetry pressure

## The Average Beta Condition

It is worth discussing the issue of the ⟨β⟩ condition a little bit more, especially regarding how one might change it as well as the possible effects changing it might have on the plasma. In general, the FRC ⟨β⟩ condition can be controlled by varying the coil flux as a function of axial location. Specifically, one might want to create the configuration shown in figure 6.10 where there is less coil flux at the ends of the FRC than under the central flux conserver. Field lines are shown with color related to field magnitude. The RMF can certainly drive current in a manner inconsistent with the FRC's ⟨β⟩ condition. Instead of trying to force its penetration depth to be consistent, it might be easier to create an experiment where one can change the FRC's ⟨β⟩ condition itself. When an FRC rests against a mirror, it can have a much higher ⟨β⟩ beta because the mirror helps to provide the axial pressure needed to confine a relatively higher pressure. Similarly, the bubble mode configuration shown in figure 6.10 allows for lower ⟨β⟩ by reducing the

axial tension available to confine the plasma. Figure 6.11 shows the radial pressure profile for three numerically simulated FRCs using the MOQUI code. The middle trace is simply the pressure profile for an FRC in an infinitely long flux conserver. The upper trace is from a mirror confined FRC with twice the end coil flux of the middle trace, while the lower trace is from a bubble mode FRC with half the end coil flux of the middle trace. The $\langle\beta\rangle$ is proportional to the area under the curve, and the bubble mode FRC has by far the lowest $\langle\beta\rangle$. The specific interest in the configuration shown in figure 6.10 has to do with the fact that the RMF must penetrate to the null. $B_z(r)$ profiles with a low $\langle\beta\rangle$ are more consistent with the profile required for the RMF to penetrate to the null, and thus they may be easier to sustain. High $\langle\beta\rangle$ profiles have a spiked current profile at their edge which is inconsistent with the current profile that would be driven by an RMF penetrating to the null.

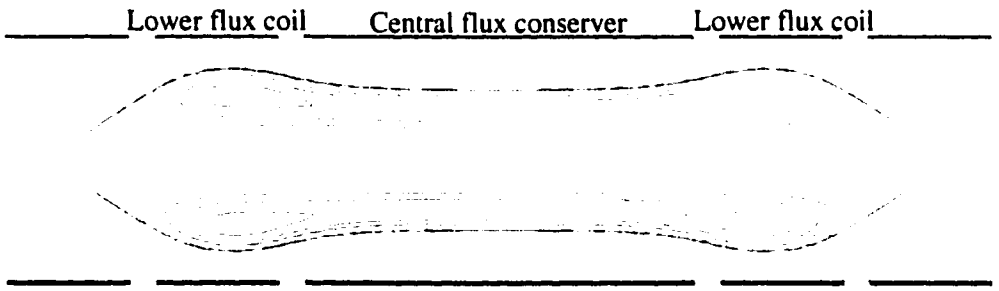


Figure 6.10 Bubble mode FRC, less coil flux at ends than in middle

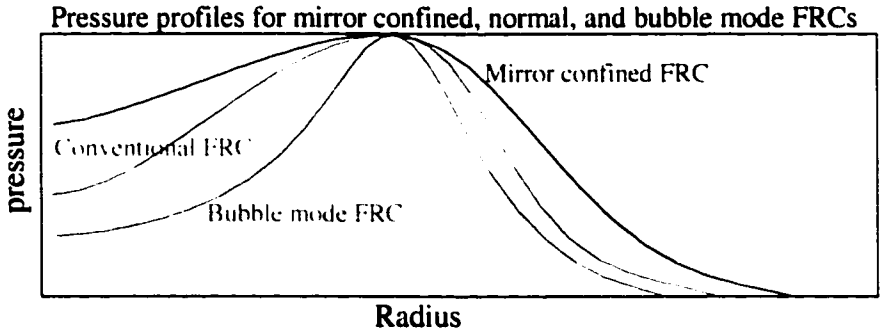


Figure 6.11 Variation of radial pressure profile with axial coil flux

As the STX plasmas evolved in time and grew axially during the gradual flux loss phase, they encountered the mirror imposed by the axial field coils shown in figure 5.16. An FRC losing flux will naturally lengthen as the end field curvature forces are reduced, so it is not surprising that as the STX FRCs lost flux, they grew axially and pushed up against the mirror. This encounter would likely have shifted the underlying ⟨β⟩ condition to call for an overall higher plasma ⟨β⟩, and could account for some of the observed increase in the plasma ⟨β⟩. Figure 6.8 also supports this explanation. The rapid increase in separatrix pressure along the entire length of the plasma correlates with it resting against the mirror between 450 and 600 μsec. Figure 6.7 is used to estimate the length of the STX plasmas, while figure 6.12 shows how the plasma separatrix and excluded flux radii at various axial locations evolve in time. Notice from 575 to 675 μsec how the separatrix radius, i.e. field reversal, disappears first at the ends of STX and then rapidly sweeps towards the center. Also notice how the excluded flux radius is a very poor indicator of what the actual separatrix radius is doing, something due to the RMF's ability to maintain a high beta open field configuration. Early in time, one can see the axial profile of the decay of the conventionally formed FRC.

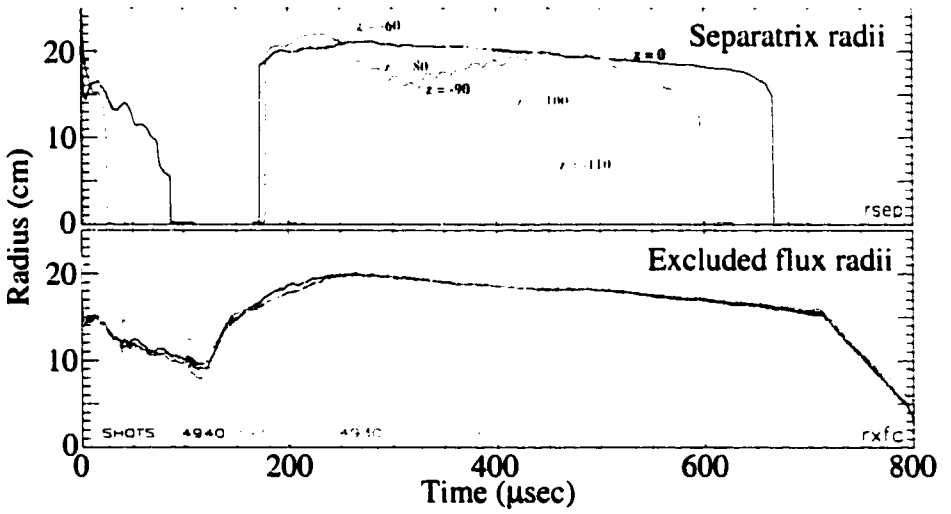


figure 6.12 Separatrix and excluded flux radii at various axial locations

## The Inability of STX To Sustain the Poloidal Flux

Several possibilities have been presented above as to why the RMF may have been unable to sustain the FRC in STX. These have primarily been based on how STX violated some of the basic equilibrium and flow requirements. There are two other observations that may also help explain STX's performance, observations that do not relate to the basic physics of RMF current drive as considered thus far. The first and most striking occurrence, one that came as a total surprise, is shown in figure 6.13, a plot of the radius of the pressure maximum, $r_{pmax}$, for a wide variety of shots. The upper plot in this figure shows 5 traces from an axial field scan, the fields and coil fluxes of which are shown in figure 6.16. In order to tell what trace corresponds to which field profile, the colors of each trace have been matched to the corresponding traces in figure 6.16, but basically, the edge field was slowly raised from that of the standard shot. It was not lowered below that of the standard shot since then the plasma has a tendency to strike the wall. The middle plot of figure 6.13 shows the results of a fill pressure scan. Unfortunately the exact pressures are not known, but it is known that shot 4899, green trace, had a higher fill pressure than shot 4910, red trace, which had a higher fill pressure than shot 4891, black trace. The pressure was not reduced below that of the standard shot, 4891, since the standard shot is already done at the lowest possible fill pressure that supports a consistent breakdown. The third plot in figure 6.13 shows traces from an RMF amplitude scan, the corresponding vacuum amplitude envelopes of which are shown in figure 6.25. Once again, the colors of the traces in figure 6.13 have been matched to the corresponding traces in figure 6.25 in order to identify which trace corresponds to which RMF amplitude. The RMF amplitude was decreased from that of the standard shot since the standard shot was done a little above the highest power level that the IGBT RMF power supplies could safely be operated at. One can see the difference in amplitude of the screened theta component of the RMF in figure 6.24.

The striking feature of figure 6.13 is that $r_{pmax}$, to a very good approximation, does not change regardless of the machine operating parameters or the plasma conditions, during the period the RMF is on. The jumping around of the traces does not reflect any true plasma dynamic, but rather is due to a difficulty in locating the pressure maximum given the flatness of the profile. In a true FRC, $r_{pmax}$ would certainly not have remained fixed since it is simply the null radius, and is quite free to change as machine and plasma parameters are varied. Such behavior can be seen during the decay of the initial conventionally formed FRC from 0 to 100 μsec, where $r_{pmax}$ falls to approximately zero as expected. The envelope formed by the bottom edges of all the traces is actually what approximately traces out the location of $r_{pmax}$ during this time, rather than any individual trace, a peculiarity which solely arises due specifics of the reduction program used.

A brief note is in order regarding the colors of the traces. In all of the radial profiles, figures 6.22, 6.23 and 6.24, the black trace is for the standard shot, the red trace is the first step away from the standard shot, the blue trace is the next step, and for the axial field scan, the green and magenta traces are the final two steps in parameter space. For all of the other figures where the three plots are stacked together, figures 6.13 through 6.21, black is always the standard shot, red is the first step away, green the next, followed by blue and cyan for the axial field scan. For both of these two color sequencings, the steady evolution from one trace to the next makes the sequencing obvious and negates much of the need to remember which color corresponds to which value of the particular parameter. They are only mentioned here in case any questions arise.

In terms of how widely these shots were varied, figures 6.14 to 6.24 show some of the other basic plasma parameters of these shots. Possibly the best ones to begin with are figures 6.22, 6.23 and 6.24 which show the time evolution of the radial $B_z$ and $B_\theta$ profiles for the axial field, fill pressure, and RMF amplitude scans. Clearly, $r_{pmax}$ has nothing to do with the particular field profile, or even the presence or absence of field reversal. The penetration depth and profile of the RMF shows a similarly independent behavior, as can

be seen by the similarity of the $B_\theta$ traces. Such similarities are most striking in figure 6.23, the fill pressure scan, where for the entire plasma duration, not only the $B_\theta$ profile, but also the $B_z$ profile between the wall and $r_{pmax}$, remain fairly constant in time independent of what is happening inside $r_{pmax}$. In figure 6.13, even though the edge field is only increased slightly, as shown in figure 6.16, the coil flux increases substantially. This likely pushes the plasma farther from the wall and explains the slight inwards shift of the $B_\theta$ profile as the field and flux are raised. Interestingly, during the initial poloidal flux drive up, the initial $\Delta B$ driven between the wall and $r_{pmax}$ is fairly constant. It is only during the gradual flux decay phase that substantial differences in this $\Delta B$ are observed. Figure 6.24, the RMF amplitude scan, also shows such a behavior. Even though the RMF had a substantially lower amplitude, it did not appear to adversely effect the ability of the RMF to create and sustain a given $\Delta B$ between the wall and $r_{pmax}$ during the initial flux driveup. A substantial difference did arise during the gradual flux decay phase where the weaker RMF drove proportionately less current.

Figure 6.14 shows the poloidal flux, figure 6.15 shows the separatrix radii and figure 6.16 shows the edge field and the normalized coil flux, $\phi/\pi r_c^2$. Notice how the standard shot always has the lowest coil flux, and how the edge field and the coil flux vary with the changing parameters. The consistent increase in coil flux explains the consistent decrease in separatrix radii shown in figure 6.15. In the pressure scan, $B_e$ remains constant while the coil flux rises. In the RMF amplitude scan, $B_e$ falls which makes sense since a weaker RMF would be expected to drive less current, but the coil flux still rises. The behavior of the coil flux and $B_e$ are unfortunately not related by the simple $B_e = B_o/(1-x_s^2)$ relationship that applies to conventional FRCs in flux conservers since the external circuit does not keep $B_o$ constant. $B_o$ is the axial field that would be present in vacuum. It is intimately tied in with the plasma behavior, and experimentally, there is very little independent control over it. Figure 6.17 shows the plasma's $\langle\beta\rangle$, of which the standard shot has the lowest $\langle\beta\rangle$ for each of the scans. This is consistent with the radial

profiles which predominantly show a loss of inner reversed field as the scan moves away from the standard shot.

Figure 6.18 and 6.19 show the peak plasma density, $n_{max}$, and the electron temperature for each of the scans. Surprisingly, $T_e$ is independent of the parameters scanned and remains constant. Possibly even more surprisingly, $n_{max}$ did not change on the fill pressure scan, the scan that was intentionally done to change it. As expected, with the exception of the trace done at highest $B_e$ where many other plasma parameters where substantially different, increasing $B_e$ lead to an increase in $n_{max}$. Also as expected, decreasing the RMF amplitude which decreased $B_e$ also resulted in a decreased $n_{max}$. These trends developed during the initial flux driveup and then persisted during the gradual flux decay. Figures 6.20 and 6.21 show the FRC energy and particle inventory per meter as opposed to the plasma energy and inventory. Hence, these traces disappear with the disappearance of field reversal even though the other plasma parameters may not be changing. Since the FRCs are approximately two meters long, these numbers can simply be doubled to estimate the total FRC energy and inventory.

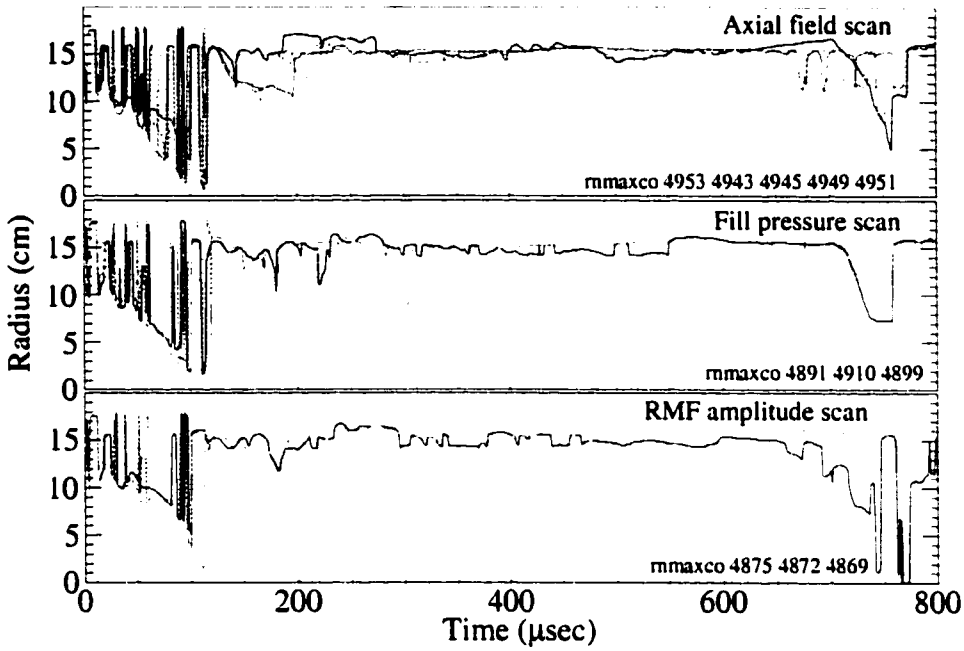


Figure 6.13 Radius of the pressure maximum, $r_{pmax}$, for scans

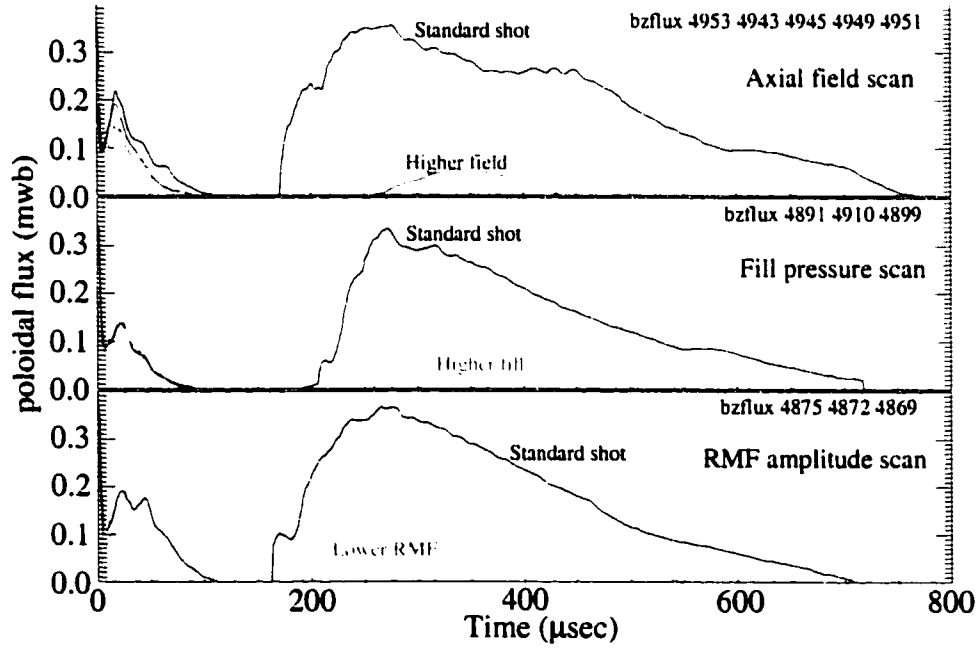


Figure 6.14 Poloidal flux for scans

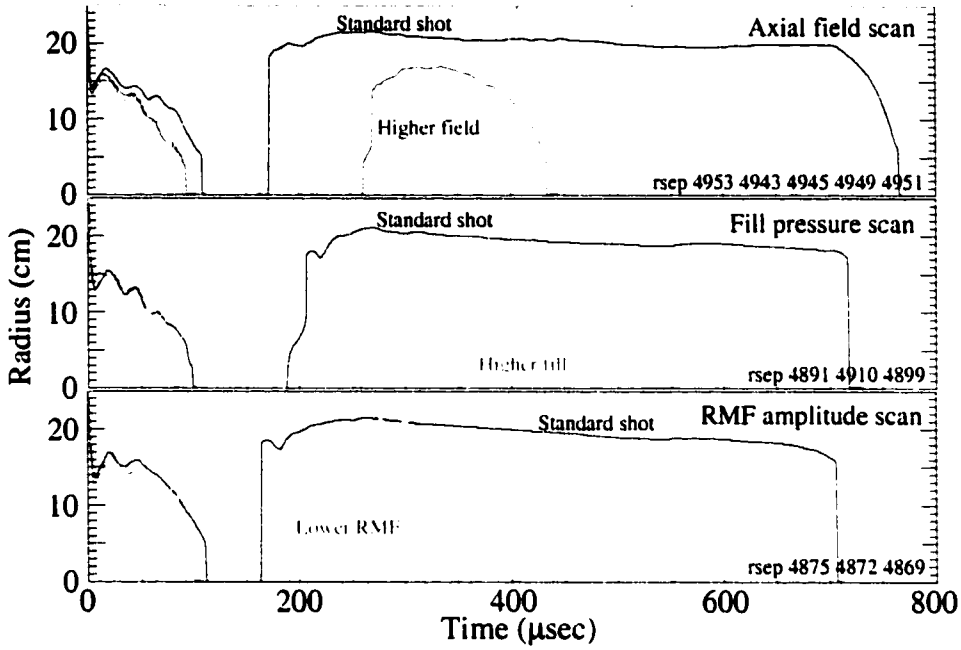


Figure 6.15 Separatrix radii for scans

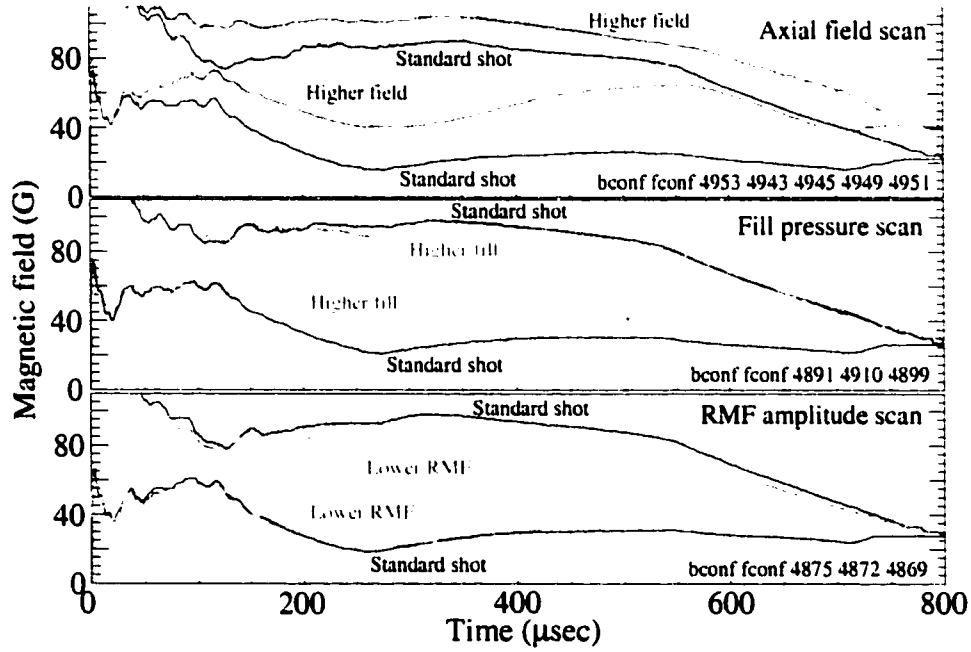


Figure 6.16 $B_e$ and normalized coil flux, $\phi/\pi r_c^2$, for scans
In each plot, upper traces are $B_e$ and lower traces are $\phi/\pi r_c^2$

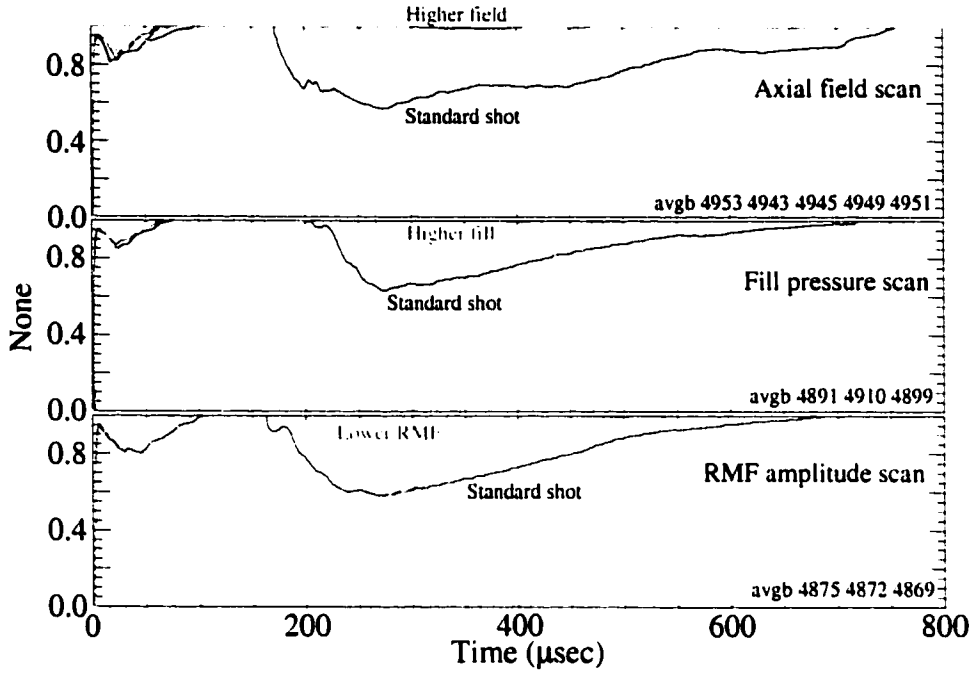


Figure 6.17 Average beta for scans

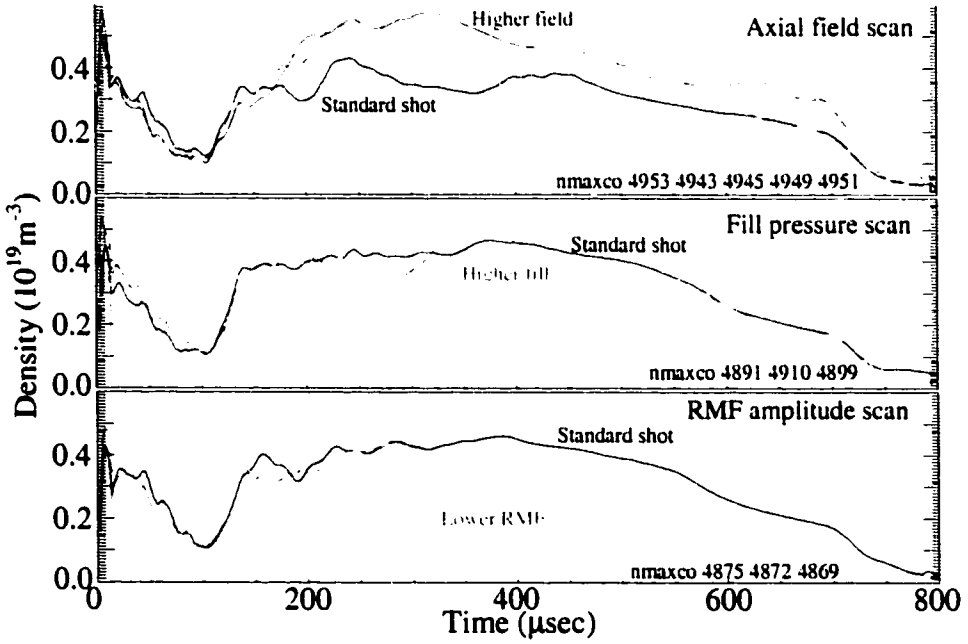


Figure 6.18 Density maximum for scans

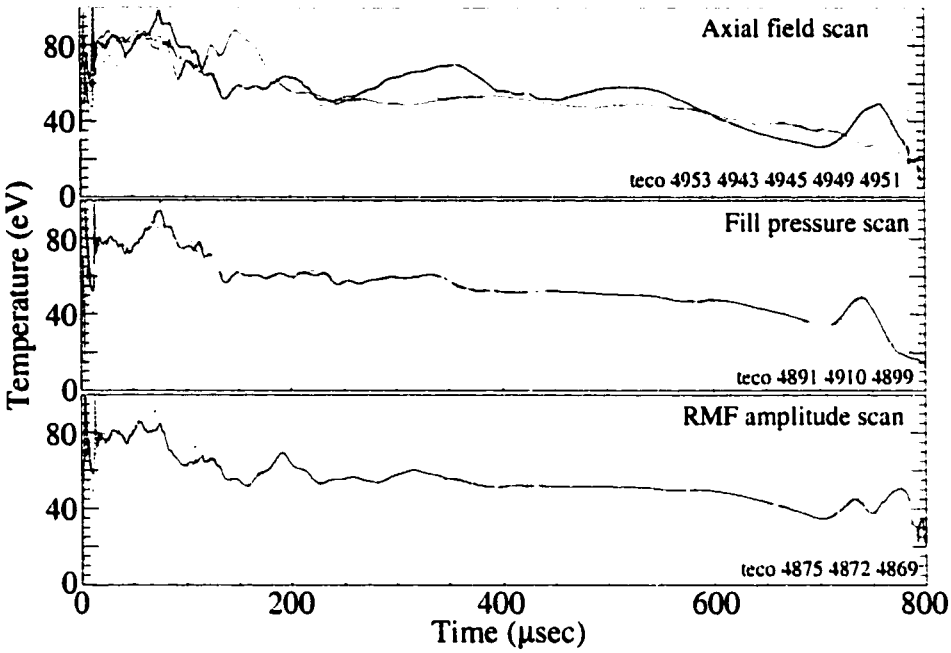


Figure 6.19 Electron temperature for scans

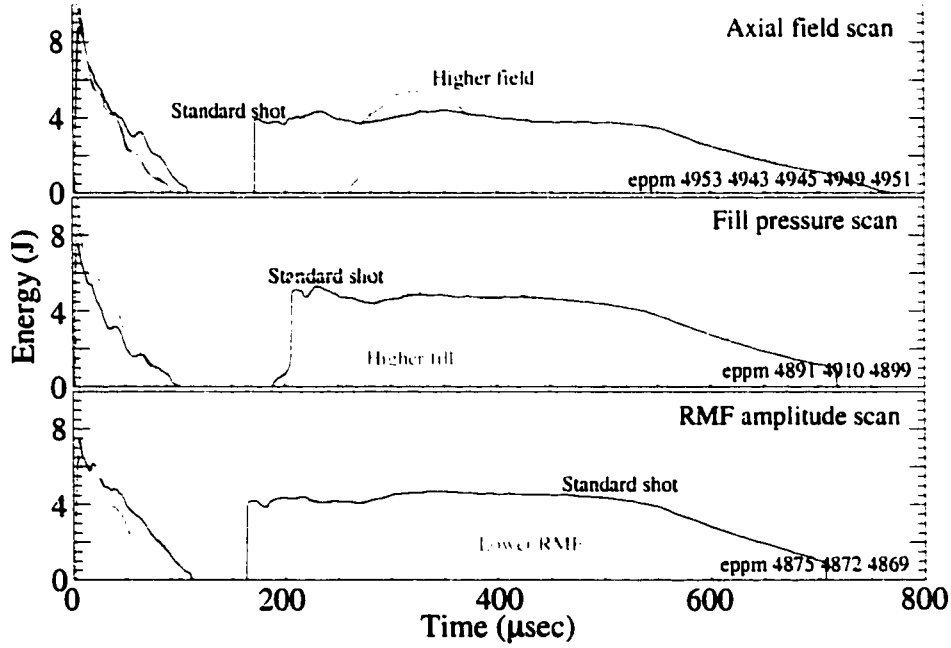


Figure 6.20 Plasma energy per meter for scans

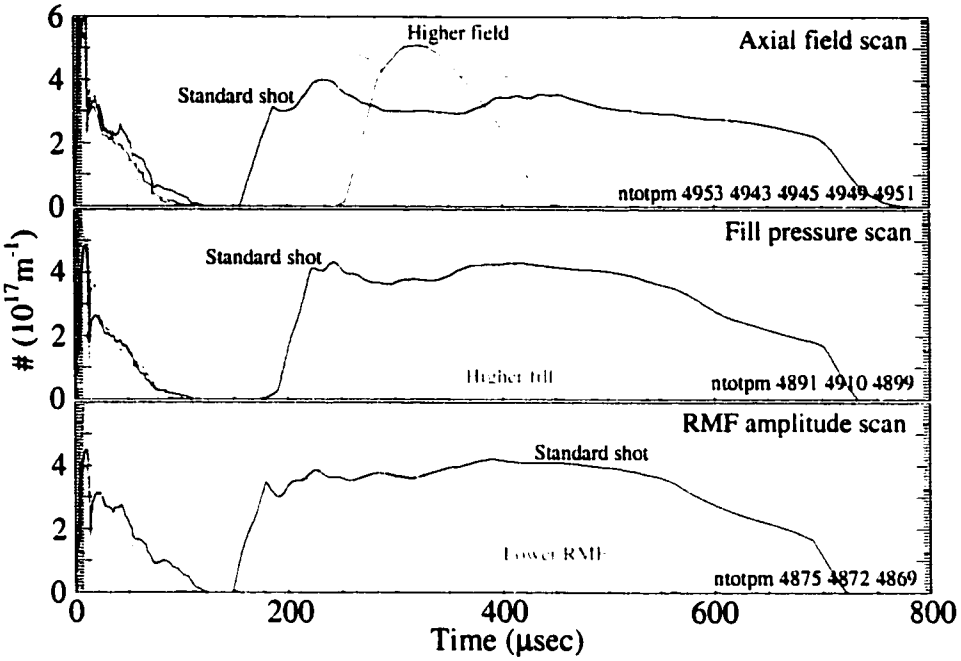


Figure 6.21 Particle inventory per meter for scans

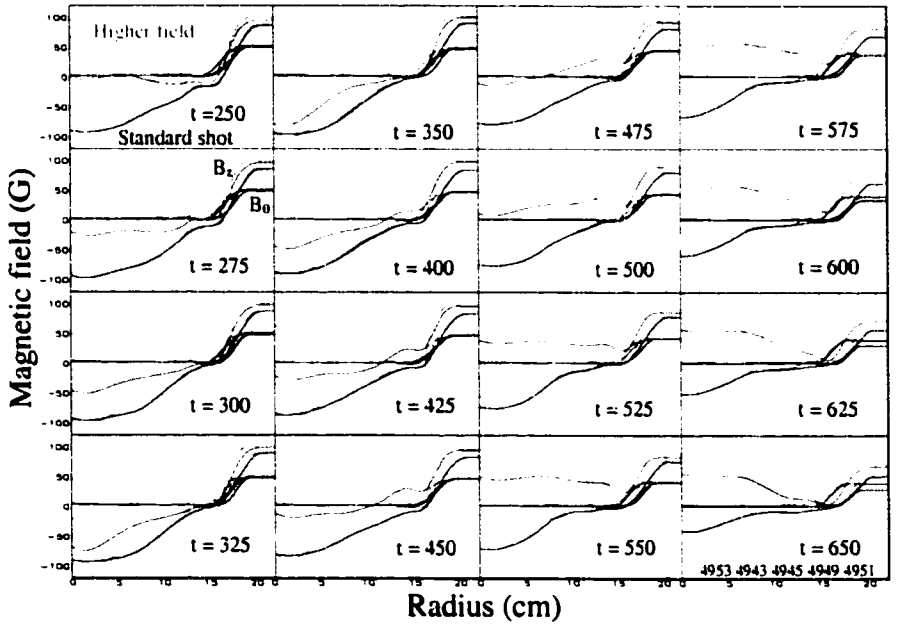


Figure 6.22 Radial profile evolution for axial field scan

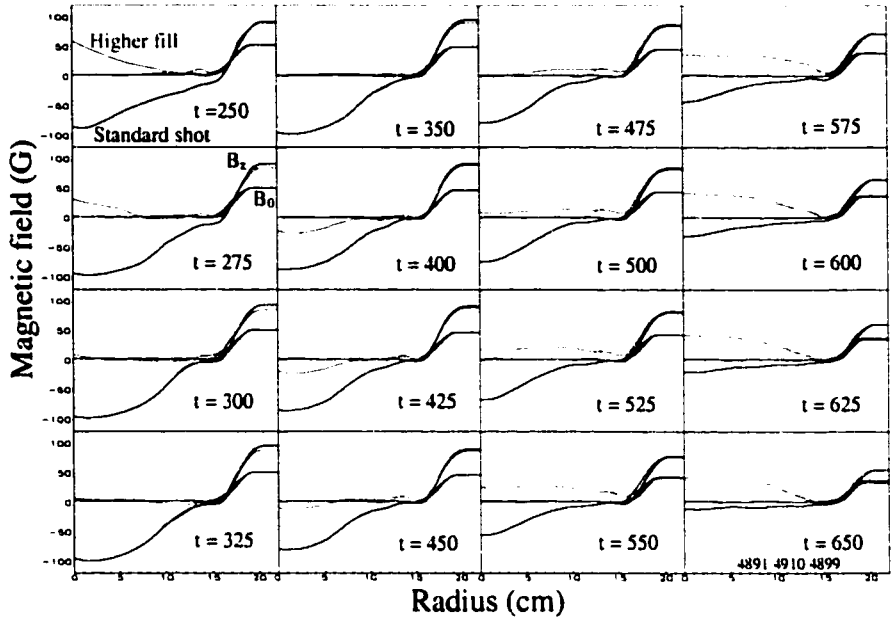


Figure 6.23 Radial profile evolution for fill pressure scan

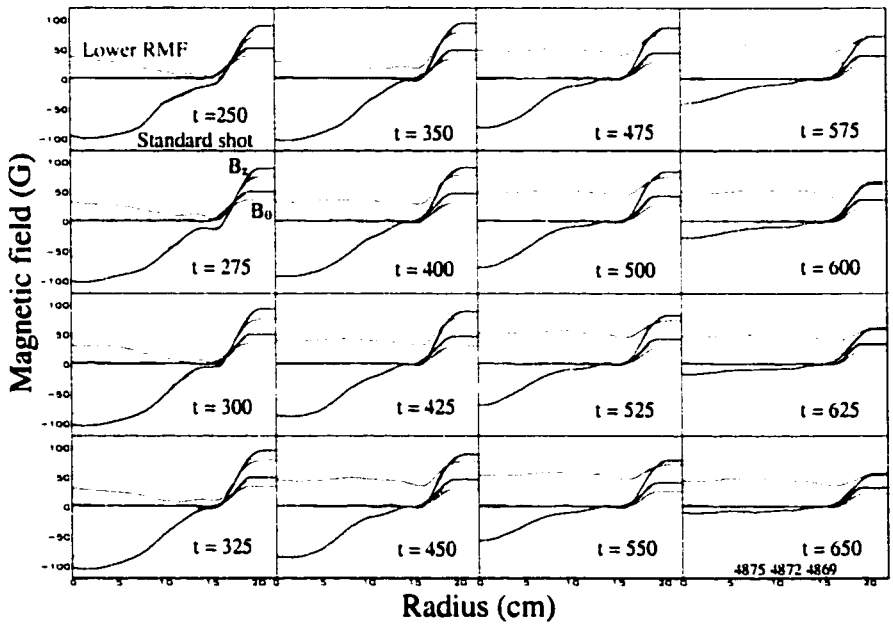


Figure 6.24 Radial profile evolution for RMF amplitude scan

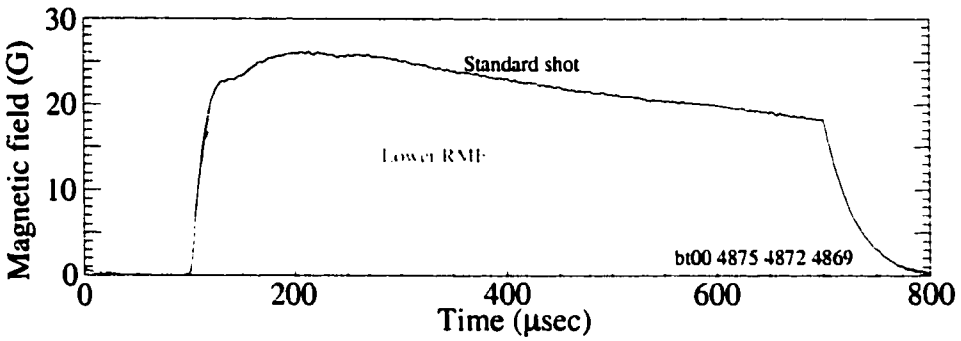


Figure 6.25 Vacuum RMF envelope for RMF amplitude scan

Though it is certainly not fully understood, the invariance of the radius of the pressure maximum, $r_{pmax}$, is a clear indication of two things. The first is that the RMF is driving current in a manner independent of the presence or absence of an FRC, and hence is free from any $\langle\beta\rangle$ condition. This was often suspected since over a wide variety of conditions, the RMF was observed to drive a similar amount of current and consequently maintain a constant $\Delta B$. The second is that the plasma some how knows about the vacuum wall, even though the plasma density is observed to vanish near the wall. The plasma preionization scheme may have something to do with this, as may axial flow. Regarding the preionization, as has been discussed in the apparatus section, the actual breakdown pressure of STX is likely not known. Rather it is set by a balance between gas evolution off the wall and flow to the pump. Once a plasma has been formed, there is no reason to expect this gas evolution to stop. Possibly the RMF penetration depth and current driven is simply set by the torque required to ionize and penetrate this continually evolving layer, a torque which could remain fairly constant if the gas evolution rate remained fairly constant. This does not explain the drop in plasma resistivity once drive is lost, nor does it explain the observed axial pressure profile, though it is not inconsistent with them either.

Regarding the issue of axial flow, STX is known to have a fair amount of open field plasma at either end, plasma that would be in intimate contact with the vacuum wall. The observed radius could be set by the balance between how fast this gas could flow axially

under the RMF antenna, how well the RMF could penetrate it, and how fast it was driven radially inwards. As has been discussed earlier, some of the end plasma certainly resulted from the initial preionization, but it could also be maintained by diffusion out of the ends of the FRC as well as RMF antenna end effects locally continuing to ionize and heat the plasma. As the plasma flows axially under the RMF antenna towards the midplane, the RMF must penetrate it in order to drive current. Since this plasma is known to be hot, around 50 eV, even assuming a high anomalous resistivity, the RMF is effectively screened. Penetration times are certainly much longer than the estimated 100 μsec plasma turn over time.

In any case, a balance between axial flow originating near the wall, the rate at which the RMF could penetrate it, and the rate at which the plasma flowed radially in off the RMF would result in the RMF driving a relatively fixed number of particles in a fixed penetration depth. This in turn would explain the independence of the driven current, $\Delta B$, and the radius of the pressure maximum on any of the other plasma or machine parameters. An effective screening of the RMF would also explain the observed low plasma resistivity during the gradual decay phase, since in being screened, the RMF would be prevented from driving the current and dissipating the power that it would otherwise be capable of. In this state, the RMF still drives enough current and radial flow to flatten the FRC field profile near the null, but it does not penetrate to the null sufficiently to sustain the FRC. Interestingly, assuming no RMF drive at the null, solving Ohm's law for $\eta$ gives a plasma resistivity of 20 μΩm. This is the same value as that based on the global power loading from the RMF antenna during this time, and the same value as that based on the empirical FRC scaling of $\tau_\phi = \phi/(d\phi/dt) = \mu_o r_s^2/16\eta$. Such an agreement is suggestive that the RMF is screened after the initial rapid drive up, and that what remains is a conventional FRC that decays as expected. The particle decay rate is much less than would be empirically expected, but the RMF thwarts radial diffusion by actively driving the particles in.

The reason for the initial rapid flux drive up likely has to do with there being a large source of cold plasma near the wall that the RMF can easily penetrate and drive, or just ionize and drive. One of the initial goals of STX was to form plasma on the RMF so one would not have to worry about the issue of RMF penetration, an issue that will be addressed by the TCS experiment. It is quite a surprise how rapidly the RMF drives plasma in, and how large an axial flow is required to sustain the observed radial flow. It is only when the RMF has driven this plasma in and is forced to rely on fueling from the ends that the RMF becomes partially screened and the plasma transitions to the low resistivity flux decay phase. Once the plasma is screened, the depth of its penetration is comparable to the resolution of the current probe, making it difficult to know exactly what is happening. An internal magnetic probe with better resolution would certainly aid in studying this transition. The numeric simulation does not account for any potential screening from axial flow since particles are simply magically transported radially to keep p a function of $\psi$. It would be very interesting to see how the code would behave if screening effects from axial flow were included. Such an effect could naturally limit the RMF penetration depth and current driven, and eliminate the need to use a resistivity much greater than that observed experimentally. The initially high plasma resistivity of 130 $\mu\Omega$m is likely due to the RMF both ionizing and heating the initially cold partially ionized plasma.

The second observation that helps to explain STX's failure to sustain the FRC lies in the behavior of the axial field banks. Specifically, after the initial poloidal flux buildup and rapid drop in coil flux, the external circuit in the standard shot always forced more flux back into the axial field magnets. This increase in flux can clearly be seen in figure 5.2 starting at ~ 280 $\mu$sec. It arises from peculiarities of the complicated circuit used coupled with the plasma changing the coil inductance and adding an IdL/dt term to the circuit equation. Such an increase in coil flux, under a wide variety of different shots, was always observed to send the FRC into its decay mode. Figure 6.26 shows this correlation between coil flux and FRC poloidal flux for a variety of different shots, as does figure

6.27. However, figure 6.27 also shows that the inverse is true. Dropping the coil flux late in time can reverse the characteristic flux decay rate and result in an increase in the poloidal flux. It was a steady drop in the coil flux that was key to the few shots that exhibited the steady poloidal flux growth in time, as shown in Figure 5.26 and figure 5.23. Even in these shots, as soon as the RMF was turned off, the banks drove additional flux back into the axial field magnets. Unfortunately, given the system used with the plasmas generated, it was virtually impossible to maintain such a decrease with any regularity.

If one believes the RMF behavior described above, then this reaction of the FRC's poloidal flux to the coil flux makes sense. Keep in mind that it is $r_{pmax}$ that is experimentally observed to be invariant, and not the null radius, something that is in direct conflict with prior notions of conventional FRCs where $r_{pmax}$ and the null radius are identical. When the coil flux is sufficiently low, the null radius is within the region penetrated by the RMF, and the RMF increases the poloidal flux. When the coil flux increases, especially just after the RMF has entered its partially screened state, the null radius is pushed in out of the region penetrated by the RMF, and whatever poloidal flux is present begins to decay away based on the characteristic plasma resistivity set by the field gradient across the null. On the few shots where the coil flux was later dropped, the null radius was once again brought into the region of RMF penetration where the RMF could drive poloidal flux again. This all hinges on the observation that the RMF drives current independent of the presence or absence of field reversal, or more importantly, independent of any $\langle\beta\rangle$ condition.

The above also explains the observed exquisite sensitivity of the plasma on the coil flux. This sensitivity is one of the most prominent features of STX, and it was something never seen in the analytic or numeric simulations, something which now makes sense since it arises from a decoupling of the $\langle\beta\rangle$ condition and the current driven by the RMF. Coil flux above a particular value always prevented FRC formation, or caused existing

FRC decay, because it pushed the null radius out of the region where the RMF could make $E_\theta$ positive and increase poloidal flux. In the three parameter scans presented above, notice the strong inverse correlation between coil flux and FRC poloidal flux shown in figures 6.14 and 6.16. The greater the coil flux, the less the poloidal flux. It is not a coincidence that in all of the scans, the standard shot had the lowest coil flux. As a point of comparison, in a "conventional" RMF driven FRC, increasing the coil flux makes it more difficult to form FRCs since the RMF is required to drive more current, as testified by the higher edge fields that are produced as the extra flux is compressed up against the wall. However, this is not an explanation of STX's inability to maintain a constant poloidal flux, and as shown in figure 6.16, increasing the coil flux actually causes a drop in the edge field, contrary to conventional wisdom. But then again, no one would have guessed that STX would hold $r_{pmax}$ as well as the current driven by the RMF constant.

Unfortunately, given the plasma's coupling into the circuit behavior and coil flux driven, the coil flux could not be varied independently of the poloidal flux. This coupling possibly explains why any small adverse perturbation to the plasma, such as adding 1% $CO_2$, either destroyed, or prevented formation of an FRC. The adverse perturbation resulted in slightly less current being driven, which resulted in less flux being initially pushed from the coil, and a greater overall coil flux. The greater coil flux pushed the null farther in and made it harder for the RMF to reverse the sign of $E_\theta$ there, which in turn resulted in even less current being driven. Such an occurrence is shown in figure 6.28 where the only difference between the two traces in each graph is that one of them was generated using pure $D_2$ and the other one was generated using 1% doped $CO_2$. The three plots show the poloidal flux, the coil flux, and the null radius. An additional negative feedback may further complicate the situation. If less flux is initial pushed out of the axial field magnets due to some adverse perturbation, then a fewer number of particles will be convected towards the wall and into the region of RMF drive. This could be particularly damaging given how important the initial source of particles was to the rapid flux

buildup. On a related note, to finish a detail mentioned earlier, hopefully the above explanation makes it apparent why STX could never create and sustain an FRC with a small separatrix radius. The small separatrix radius simply held the null radius out of the reach of the RMF.

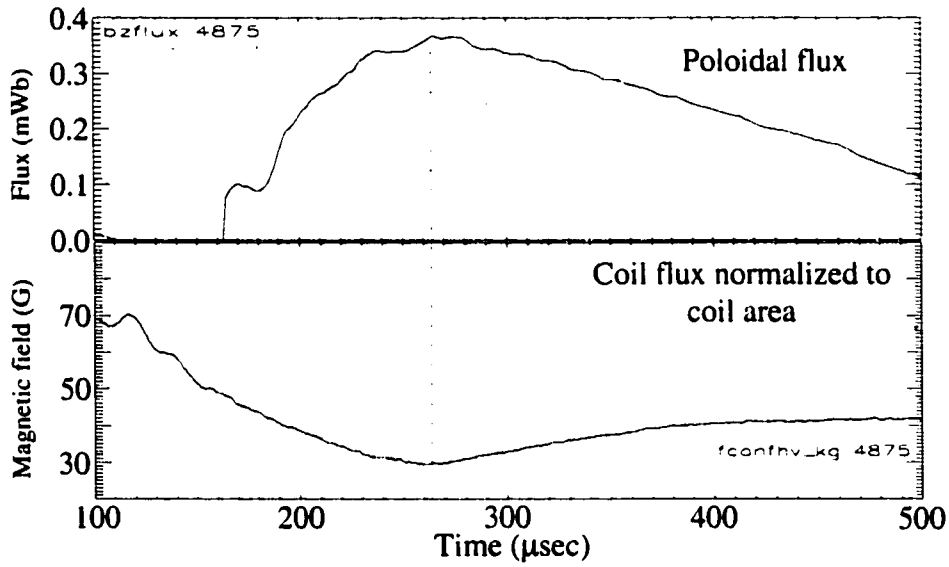


Figure 6.26 Coil flux causing poloidal flux decay

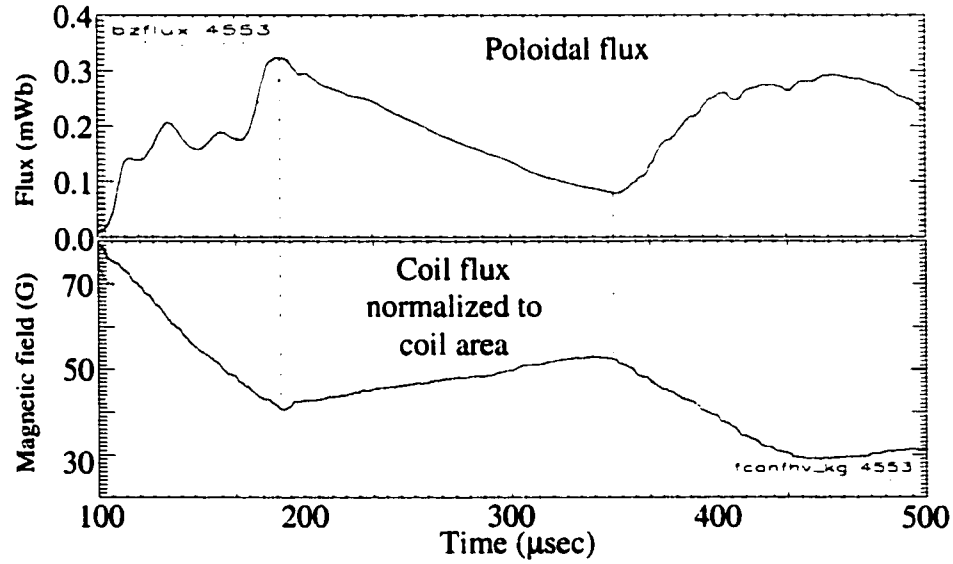


Figure 6.27 Coil flux causing poloidal flux decay and growth

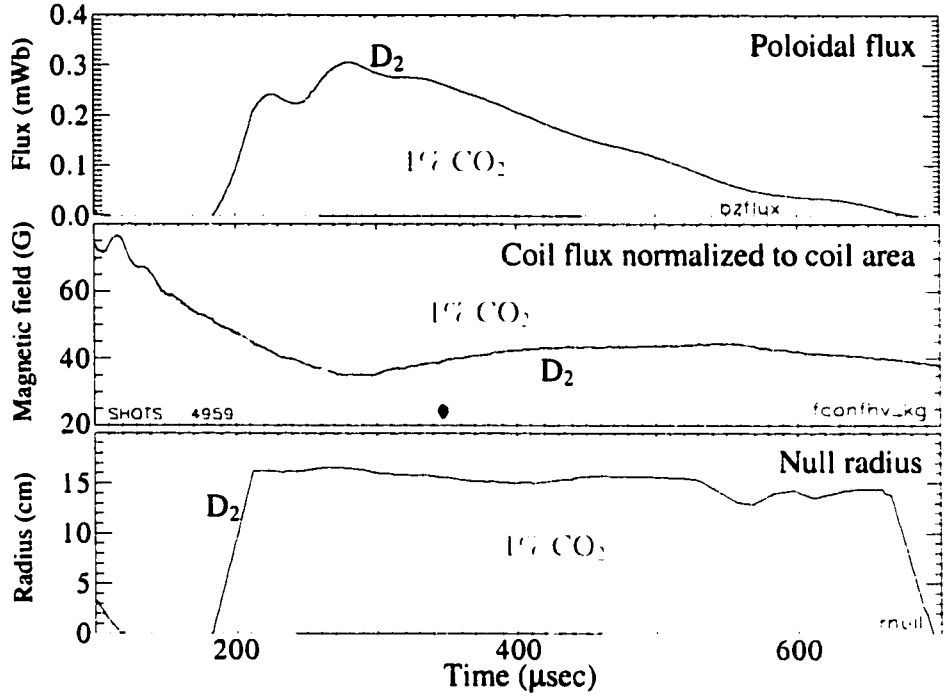


Figure 6.28 The impact of impurities on coil and poloidal flux

## A Brief Summary

To conclude this discussion of STX and its inability to sustain a steady poloidal flux, the following few paragraphs summarize the hypotheses presented above. When the RMF exhausts the supply of readily available particles during the initial flux buildup by driving them radially inwards, axial flows become the dominant source of particles. The axial flow partially screens the RMF and prevents it from driving the current that would otherwise be expected based on the observed plasma resistivity. The flow originates at either end of STX and imparts a knowledge of the wall to the RMF, fixing the RMF penetration depth with respect to the wall. The current driven and penetration depth are simply set by the rate at which the RMF can penetrate the axial flow. It can never slowly work its way in since new particles are always being introduced at the ends near the wall that cause a continual screening. The result of this behavior is that the RMF is decoupled

from the FRC equilibrium. It would certainly be interesting to see this effect modeled in the numeric simulation.

The RMF initially works well for several reasons. The plasma is cold, near the wall, and easy for the RMF to penetrate. The RMF is always observed to rapidly penetrate such initial target plasmas and drive current. There is a large source of particles for the RMF to drive inwards, a source likely augmented by initially continuing ionization. It is only when these particles have been driven radially in that axial flows arise to replenish them, flows which partially screen the RMF. Such screening flows in and of themselves would not decouple the RMF from the FRC equilibrium. The decoupling arises from the observed invariance of the RMF penetration depth and $r_{pmax}$, an empirical observation which is not fully understood. The transition from the initially unscreened state where ionization may be continuing to occur, to the partially screened state, is believed to explain the observed dramatic drop in plasma resistivity. Unfortunately, it is not known whether the initial resistivity is high due to continuing ionization, fundamental dynamics of the flux buildup, or some other process, and equivalently, it is not known if the resistivity drops later in time because the RMF is screened from the plasma, the plasma has entered a more quiescent state, or some other as of yet unidentified mechanism is at work.

The decoupling of the RMF from the FRC, in turn, would not explain STX's inability to drive a steady FRC with constant poloidal flux. However, STX's inability is explained when one considers the axial bank's tendency to drive flux into the coils after the initial flux buildup, and the feedback that occurs between the effectiveness of current drive and the coil flux. Too great a coil flux pushes the null radius out of the region of RMF penetration. The resistive decay term in Ohm's law is no longer countered by the RMF drive term, and the FRC decays. This decay was successfully reversed on a few shots where the coil flux was once again dropped, bringing the FRC null radius into the region of RMF current drive. If the coil flux is too high, the RMF will still readily drive current,

but instead of an FRC, the ring state will result. The ring state takes a similar amount of work to drive based on ohmic dissipation with the observed current distribution, but does not lead to field reversal. The net torque produced in the plasma in the ring state is much less then when the plasma is in the FRC state since the driven poloidal currents inside $r_{pmax}$ flow in the opposite direction of those outside $r_{pmax}$.

## A Comparison to TCS

Fortunately, the TCS[7] experiment appears to have demonstrated the ability of the RMF to maintain an FRC's poloidal flux with RMF current drive. The actual flux has not been measured yet, but the reversed field on axis is measured to be held constant, which given the steady behavior of some of the other plasma parameters, is a fairly good indication that the poloidal flux is remaining constant as well. TCS's success at sustaining the FRC is very encouraging and supports the contention that STX is unable to sustain the FRC due to some of the device specific issues discussed rather then a fundamental problem with the RMF current drive process itself. TCS is presently operating in a very similar regime as STX, with typical plasma parameters of $n \sim 10^{19}$ $m^{-3}$, $T_e \sim 30$ eV, $T_i \sim$ cold, $B_e \sim 100$ G, and $B_{RMF} \sim 35$ G. The confinement vacuum chamber is 2.5 m long with a 40 cm radius, and typical plasma radii are ~ 35 cm. Figure 6.29 shows excluded flux, coil flux, edge field, and internal field traces.

The ability of TCS to maintain the FRC flux where STX generally failed to do so is consistent with some of the differences between the two machines. One of the most important differences likely has to do with the TCS axial field banks not driving addition flux into the axial field magnets the way those on STX did. The beginning and end values of the flux trace shown in figure 6.29 actually indicate a slight drop in coil flux, an occurrence which likely facilitates the current drive process. The presence of plasma changes the coil flux trace, though not the actual coil flux, because the flux loop is positioned at a radius smaller then the coil radius, allowing the plasma to compress flux

into the space between the flux loop and the coil. On STX, the flux loops sit at the coil radius and eliminate this sort of behavior. What is important though is that for the duration of the plasma, the coil flux remains constant or decreases slightly, but certainly does not increase.

A second important difference may have to do with the size of the RMF antenna relative to that of the sustained FRC. On TCS, the RMF antenna is ~ 1.6 meters long and does not span the length of the FRC, unlike the 2 m long antenna on STX. Hence the TCS antenna is less likely to be interfering with the different azimuthal currents that must flow at the ends of the FRC in order to maintain the equilibrium, interference which has been observed on STX. A shorter antenna also means that relative to the radial flows driven, smaller axial flows are needed. Smaller axial flows in turn may result in less screening of the RMF and allow for overall better current drive. Additionally, by not spanning the length of the FRC, the RMF antennas gives space for radially outwards particle diffusion to occur, diffusion which can help sustain the swirling flow pattern driven by the RMF. A final area in which TCS may benefit has to do with the difference in plasma radii of the two machines. A figure of merit for how easily the particles inside the FRC can flow or diffuse axially out the ends may be given by the ratio of the axial distance needed to travel to the cylindrical area available to travel in. This ratio is 8 on TCS and 32 on STX, giving the STX particles a much more difficult trip. Such axial flow is believed to have been restricted in STX, though it must occur in steady state to offset the radial inwards flow driven by the RMF.

FRC end effects are believed to have played a role in the STX plasma, and data from TCS also indicates their importance. Two axial field scans were done. In one, the end mirror field was slowly raised, while in the other, the axial field near either end of the FRC was reduced, creating more of a bubble mode configuration. The result of these scans are shown in figures 5.30 and figure 6.31. Notice how the increase in the mirror field leads to a gradual decay of the reversed field on axis, and presumed gradual loss of

poloidal flux, while the shift towards the bubble mode enhanced the reversed field on axis. These results are consistent with the predictions made based on the STX data that a mirror field is likely detrimental while the bubble mode configuration is beneficial.

Another big difference between STX and TCS has to do with the observed plasma resistivity. On both machines this resistivity is initially greater then 100 μΩm, but on STX it falls to 20 μΩm while on TCS it does not. Given the importance of this resistivity to the overall usefulness of the current drive scheme, understanding this difference is very important. At present there are several possibilities, though no clear explanation. The possibilities generally have to do with why the resistivity might remain so high in TCS, and include such things as an unusually high impurity level, a high charge exchange rate with neutrals, or some sort of global instability. The geometry of the TCS FRC's may make them more prone to the tilt instability, and the shorter RMF antenna may have less of a stabilizing influence then the long STX antenna has on the STX FRCs. The lower STX resistivity certainly holds out hope for improved performance on the TCS experiment.

The Flinder's rotamak experiments, unlike STX, also maintained a steady field reversal with the RMF current drive. Given the lack of a true FRC equilibrium, coupled with a spherical, partially ionized, and wall supported plasma, these experiments served more to demonstrated the ability of the RMF to drive current in the rotamak configuration, rather then the ability of the RMF to sustain the FRC equilibrium. Consequently, these experiments do not appear to provide much insight into the behavior of the STX plasmas, especially with respect to the three dimensional equilibrium effects. Given the differences though, the similarities in the radial field profiles and RMF penetration depth, figure 5.13 and figure 5.17, are quite remarkable, and indicate an underlying similarity in the current drive physics between the experiments.

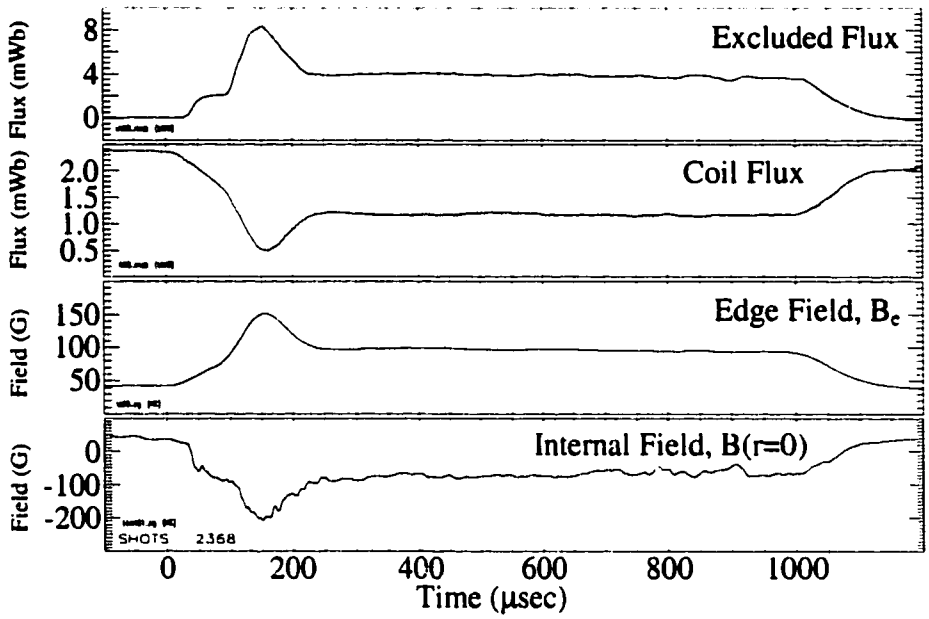


Figure 6.29 Typical TCS flux and field traces
(RMF on from 0 to 1000 msec)

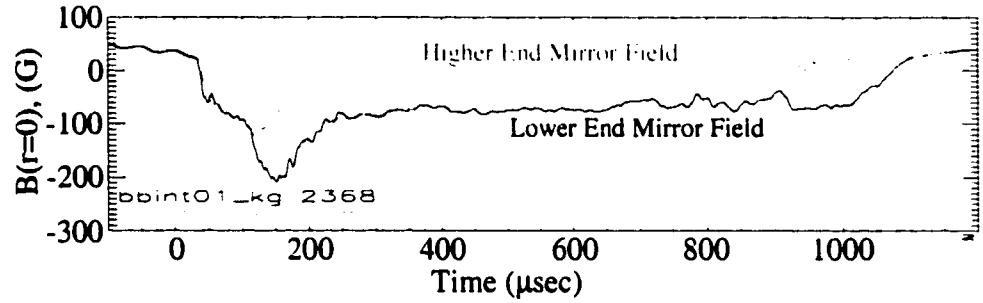


Figure 6.30 Impact of increasing end mirror on B(r=0)

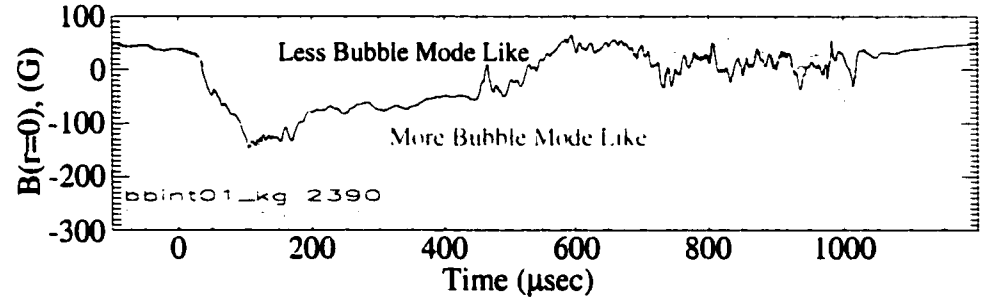


Figure 6.31 Impact of reducing axial field at either end on B(r=0)

# CHAPTER 7
# CONCLUSIONS

During the coarse of the STX experiment, the understanding of RMF current drive in FRCs has improved substantially. Key experimental observations, the most important of which was likely the observation of very low separatrix density, guided the development of analytic and numerical modeling of RMF current drive in FRCs. These models made important predictions about the interplay between the RMF and the FRC, particularly regarding the importance of current being driven in a manner consistent with the FRC equilibrium, and the importance of radial and axial flows. Though definitive measurements of flow patterns and RMF driven FRC equilibria have not been made, STX data is not only consistent with the models, but also directly support some of the predictions made. More importantly, STX data provide important insight into three axial effects not considered in the modeling or theory, insight that can be directly used to guide future experimentation.

The first involves the observation that a spatially uniform RMF may be consistent with an infinitely long FRC obeying its $\langle\beta\rangle$ condition, but it will likely never be consistent with the actual axial current profile that must flow at the ends of the FRC. By its very nature, the RMF wants to drive an axially uniform current, a current inconsistent with an FRC's true axial current profile. This suggests that the RMF should only be applied to the central region of the FRC where the current profiles are in agreement. RMF antenna end effects may still be important, but placing them sufficiently far from the end of the FRC likely reduces their ability to upset the equilibrium.

The second involves the observation that the true closing of the FRC flow pattern is important. The radial flow must balance the axial flow in all regions. This not only sets a limit on the total length of the RMF antenna, but also a limit on the fractional length of the FRC that can be covered with the RMF antenna. The limit to the absolute length of

the RMF antenna arises in two manners. First, all axial flow towards the midplane that resupplies particles near the separatrix must originate outside the region covered by the RMF antenna, since once under the antenna, flow is driven only inwards. Since the RMF wants to drive an axially uniform radial inward flow, the longer the antenna, the greater the necessary axial flow. At some point, the RMF antenna will become long enough that the flows needed to supply it will become implausible. The shorter the antenna, the smaller the axial flow needed. The same argument applies to the axially outward bound flows occurring near the axis of symmetry. Second, the RMF will need to continuously penetrate regions where axial flow is occurring since the axially incoming flow likely does not already have the RMF embedded in it. The greater the flow, the greater the potential impediment to RMF penetration, and without sufficient penetration, current drive will fail. The limit on the fractional length of the FRC covered by the RMF antenna arises from balancing the axial flow with the outward radial flow that must occur outside the region covered by the RMF antenna. If the plasma can simply flow out and around on the FRC's closed poloidal field lines, then this issue may not be so important, assuming that the RMF does not directly inhibit such flow parallel to the magnetic field. However, if the plasma must diffuse radially out across the axial field, then the issue of the FRC to RMF antenna length could be very important. The length of FRC outside of the RMF antenna would need to be sufficiently long so that the radial diffusive flow could balance the required axial flow.

The third involves the possibility of varying the FRC's $\langle\beta\rangle$ condition from that of an FRC in an infinitely long flux conserver, i.e. $\langle\beta\rangle = 1 - 0.5x_s^2$. As $\langle\beta\rangle$ becomes lower, the RMF may have an easier time penetrating to the null since the magnetic profile becomes more consistent with cosynchronous electron rotation and since the RMF will have relatively fewer particles to penetrate through. A lower $\langle\beta\rangle$ configuration also leaves more space on the inner field for radial diffusion and axial flow to occur. Interestingly, as shown in figure 5.23 and 5.30, the few shots that exhibited a steadily increasing flux, also had a steadily decreasing $\langle\beta\rangle$, an $\langle\beta\rangle$ that fell below the value based on $\langle\beta\rangle = 1 - 0.5x_s^2$.

Changing the FRC's $\langle\beta\rangle$ condition would change the FRC's axial current profile, making it potentially important to keep the RMF antenna over just the central region of constant coil flux where the FRC's axial current profile is uniform.

All of the above suggest the need for an experiment where the length of the RMF antenna can be readily adjusted and made short compared to the length of the FRC, and where the axial coil flux profile can be readily adjusted as well. Such a machine would address basic physics issues involving the combination of the FRC's true three dimensional equilibrium and RMF current drive, issues presently unaddressed in any theory or simulation. Two suitable machines exist at RPPL for performing such experiments, STX and TCS, each with its own particular advantages and disadvantages.

The STX experiment is both easy to modify, and has a sufficiently large length to diameter ratio that a wide variety of antenna and axial field configurations could be tried. Importantly, it allows for experiments were the length of the antenna could be kept sufficiently short compared to the length of the FRC so that the RMF antenna's end effects could be completely decoupled from the FRC's equilibrium end profile, as well as largely decoupled from the region of axially varying coil flux needed to produce the bubble mode configuration. It would be very interesting to see how such changes would effect the basic plasma resistivity. Presumably, the antenna length best matched to the flow patterns would produce the least turbulence, and hence the lowest plasma resistivity. In order to perform these investigations though, STX would need a few modifications, the most important of which would be a readily controllable axial field, a better plasma preionization scheme, and a more powerful IGBT based RMF power supply. An additional draw back to the STX devise is the poorly understood coupling of $r_{pmax}$ to the wall, though it is suspected that a better plasma preionization scheme would eliminate such coupling.

The TCS experiment on the other hand does presently produce steady RMF driven FRC equilibria, and consequently, effects of varying RMF antenna length as well as axial flux profiles could be more immediately observed. By the time of such experiments, TCS will also likely have a much better set of diagnostics then STX. Ignoring the unexplained difference in plasma resistivity between the two devices, the primary difficulty arises from the length to diameter ratio of the TCS vacuum chamber and RMF antenna. Specifically, TCS does not have the length to diameter ratio necessary to fully decouple FRC end effects from RMF antenna end effects, let alone bubble mode axial flux changes from the RMF antenna end effects. Decoupling these could be of critical importance, and fortunately, sufficient quartz tube vacuum pieces do exist to lengthen the TCS chamber. Lengthening the TCS chamber may have the additional benefit of reducing a source of plasma contamination by moving the end cones sufficiently far from the ends of the plasma, at least for the quiescently formed plasmas where the end cones are not needed to stop axial plasma translation. It will certainly be interesting to study true three dimensional equilibrium interactions between the RMF and FRC that occur both at the ends of the RMF antenna and at the ends of the FRC. Key issues to be addressed are the appropriate FRC to RMF antenna length ratio and the appropriate axial coil flux profile.

# Bibliography


1. H. A. Blevin, P. C. Thonemunn, "*Plasma confinement using an alternating magnetic field*", Nuclear Fusion: 1962 Supplemental Part 1, **55** (1962)
2. G. Durance, I. R. Jones, "*Investigations of the magnetic field structure of high-power, short-duration rotamak discharges*", Phys. Fluids **29**, 1196 (1986)
3. Peter Euripides, "*Experimental Investigations of Power Transfer in the 50 Liter Rotamak*", Ph.D. Thesis, The Flinders University of South Australia, February 23, 1998.
4. J. A. Grossnickle, "*Field-Reversed Configuration Acceleration for deep Fueling of Large Tokamaks*", Ch. 5, Masters Thesis, University of Washington, 1996
5. A. L. Hoffman, J. T. Slough, "*Flux, Energy, and Particle Lifetime Measurements for Well-Formed FRCs*", Nuclear Fusion **26**, 1693 (1986)
6. A. L. Hoffman, J. T. Slough, "*FRC Lifetime Scaling Based on Measurements from the Large s Experiment (LSX)*", Nuclear Fusion **33**, 23 (1993)
7. A. L. Hoffman, "*Flux build-up in field reversed configurations using rotating magnetic fields*", Phys. Plasmas **5**, 979 (1998)
8. A. L. Hoffman, "*Rotating magnetic field current drive of FRCs subject to equilibrium constraints*", Nuclear Fusion **40**, 1523 (2000)
9. Hoffman et al., "*The Large-s Field-Reversed Configuration Experiment*", Fusion Technology **23**, 185 (1993)
10. W. N. Hugrass, "*Cylindrical Plasma Equilibria Maintained by Means of a Rotating Magnetic Field*", J. Plasma Physics **28**, 369 (1982)
11. W. N. Hugrass, "*The Existence of Non-unique Steady State Solutions to the RMF Current Drive Equations*", Aust. J. Phys. **38**, 157 (1985)
12. W. N. Hugrass, R. C. Grimm, "*A numerical study of the generation of an azimuthal current in a plasma cylinder using a transverse rotating magnetic field*", J. Plasma Physics **26**, 455 (1981)

13. W. N. Hugrass, I. R. Jones, K. F. McKenna, M. G. R. Phillips, R.G. Storer, H. Tuczek, "*Compact torus configuration generated by a rotating magnetic field: the rotamak*", Phys. Rev. Lett. **44**, 1676 (1980)

14. I. R. Jones and W. N. Hugrass, "*Steady-state solutions for the penetration of a rotating magnetic field into a plasma column*", J. Plasma Phys. **26**, 441 (1981)

15. A. J. Knight, I. R. Jones, "*A Quantitative Investigation of Rotating Magnetic Field Current Drive in a Field-Reversed Configuration*", Plasma Phys. Contr. Fusion **32**, 575 (1990)

16. R. H. Lovberg, "Magnetic Probes", Chapter 3 in Plasma Diagnostic Techniques, ed. by R. H. Huddlestone and S. L. Leonard, Academic Press, New York (1965) pp. 69-112.

17. R. D. Milroy, "*A numerical study of rotating magnetic fields as a current drive for field reversed configurations*", Phys. Plasmas **6**, 2771 (1999)

18. R. D. Milroy, "*A magnetohydrodynamic model of rotating magnetic field current drive in a field-reversed configuration*", Phys. Plasmas **7**, 4135 (2000)

19. H. Momota, A. Ishida, Y Kohzaki, G. H. Miley, S. Ohi, M. Ohnishi, K. Yoshikawa, K. Sato, L. C. Steinhauer, Y. Tomita, M. Tuszewski, "*Conceptual Design of a D-$^3$He FRC Reactor ARTEMIS*", Fusion Technology **21**, 2307 (1992)

20. M. Ohnishi, Y. Yamamoto, K. Yoshikawa, J. Kitagahi, A. Ishida, "*A steady state field-reversed configuration with rotating magnetic field*", Proceedings 16$^{th}$ IEEE/NPSS Symposium on Fusion Engineering, (IEEE, Picataway, NJ, 1995) Vol. 2, 1413 (1995)

21. Siemon et al., "*Review of the Los Alamos FRX-C Experiment*", Fusion Technology **9**, 13 (1986)

22. J. T. Slough, A. L. Hoffman, "*Penetration of a transverse magnetic field by an accelerated field-reversed configuration*", Phys. Plasmas **6**, 253 (1999)

23. J. T. Slough, K. E. Miller, D. E. Lotz, M. R. Kostora, "*Multimegawatt solid state rf driver for generating rotating magnetic fields*", Rev. Sci. Instr. **71**, 3210 2000

24. M. Tuszewski, "*Field Reversed Configurations*", Nuclear Fusion **28** (1988) 2033

25. E. T. Um, "*Diamagnetic Loop Diagnostic System for the Trap Experiment*", Masters Thesis, University of Washington, 1994

# Vita

Kenneth Elric Miller:

Doctor of Philosophy, Plasma Physics, University of Washington, 2001.

Master of Science, Aeronautics and Astronautics, University of Washington, 1996.

Bachelor of Arts, Magna Cum Laude, Physics, Amherst College, 1992.